



**HAL**  
open science

# Study of reduction process on perovskite nickelates and its derivatives : a bulk and thin film approach

Mufeed Keenari

► **To cite this version:**

Mufeed Keenari. Study of reduction process on perovskite nickelates and its derivatives: a bulk and thin film approach. Physics [physics]. Normandie Université, 2023. English. NNT : 2023NORMC281 . tel-04509574

**HAL Id: tel-04509574**

**<https://theses.hal.science/tel-04509574>**

Submitted on 18 Mar 2024

**HAL** is a multi-disciplinary open access archive for the deposit and dissemination of scientific research documents, whether they are published or not. The documents may come from teaching and research institutions in France or abroad, or from public or private research centers.

L'archive ouverte pluridisciplinaire **HAL**, est destinée au dépôt et à la diffusion de documents scientifiques de niveau recherche, publiés ou non, émanant des établissements d'enseignement et de recherche français ou étrangers, des laboratoires publics ou privés.

# THÈSE

Pour obtenir le diplôme de doctorat

Spécialité **PHYSIQUE**

Préparée au sein de l'**Université de Caen Normandie**

**Study of Reduction Process on Perovskite Nickelates and its Derivatives: A Bulk and Thin Film Approach**

Présentée et soutenue par

**MUFEEED KEENARI**

**Thèse soutenue le 09/11/2023**

devant le jury composé de :

M. RACHEL DESFEUX	Professeur des universités - UNIVERSITE ARTOIS	Rapporteur du jury
M. MATHIEU PASTUREL	Directeur de recherche - UNIVERSITE RENNES 1	Rapporteur du jury
MME ALEXANDRA PENA REVELLEZ	Chargé de recherche - UNIVERSITE GRENOBLE ALPES	Membre du jury
M. WILFRID PRELLIER	Directeur de recherche au CNRS - ENSICAEN	Président du jury
M. ADRIAN DAVID	Maître de conférences - Université de Caen Normandie	Directeur de thèse
M. YOHANN BREARD	Maître de conférences - Université de Caen Normandie	Co-directeur de thèse

Thèse dirigée par **ADRIAN DAVID** (Laboratoire de cristallographie et sciences des matériaux (Caen)) et **YOHANN BREARD** (Laboratoire de cristallographie et sciences des matériaux (Caen))





---

# ACKNOWLEDGMENT

I would like to express my profound gratitude to my advisors, Dr. Adrian David and Dr. Yohann Breard, for their unwavering support and invaluable guidance throughout my PhD journey. I am deeply indebted to Dr. Wilfrid Prellier, the Director of CRISMAT Lab, for granting me the opportunity to become a part of the CRISMAT research community. My sincere appreciation to Dr. Philippe Boullay, Dr. Denis Pelloquin, and Ms. Sara Passuti for their significant contributions to Electron Microscopy studies, and to Dr. Julien Varignon and Mr. Alvaro Adrian Carrasco Alvarez for their valuable insights from DFT calculations. I extend my gratitude to Dr. Alain Pautrat, Dr. Ulrike Lüders and Dr. Arnaud Fouchet for engaging in fruitful scientific discussions and Dr. Maryline Nasr for her invaluable contributions to our project.

I am profoundly thankful to my lab mates and friends for their camaraderie and unwavering support. I would also like to acknowledge the indispensable assistance provided by the technical staff. I am forever grateful to the dedicated teachers from my school and college days who instilled in me a passion for science and nurtured my scientific curiosity.

My deepest appreciation goes to the most important individuals in my life, my father, Mr. Muneer Keenari, and my mother, Ms. Rashida Muneer, for their support, love, and encouragement. I am also deeply indebted to and appreciative of my grandmothers for their boundless love and support. I extend my heartfelt gratitude to my uncles, who stood by me during challenging times, and to my entire family for their enduring love and affection. I offer my sincere thanks to my loving wife, Ms. Masmoora Edachery Kandy, who provided me with immense confidence and support during my PhD journey. Her untiring moral and emotional support helped me complete my research in a timely manner. A special mention goes to my brother, Rashad Keenari, and my sister, Ms. Hiba Fathima Keenari, for being a part of my life. I am also thankful to my in-laws, Mr. Mahroof Edachery Kandy and Ms. Thahira Mahroof, and my brother in-law Mr. Manas for their love and support.

I extend my heartfelt appreciation to my dearest friends and mentors, Dr. Suraj Rajan and Dr. Muhammed Juvaïd, for their invaluable support. A special acknowledgment goes to Dr. Marthando and Dr. Mudit for their assistance during my research. I am sincerely grateful to my dearest friends Mr. Sarath, Dr. Gayathri, Ms. Sreya, Mr. Praveen, Mr. Pranav, Dr. Rahul, Mr. Krishnendu, Mr. Jeffry, Dr. Paribesh, Dr. Hari, Mr. Abhishekh, Mr. Oualyd, Ms. Erica, Mr. Abdel, Mr. Moussa, Ms. Anjali, Ms. Parameshwari, Ms. Indu, and Mr. Sayan for the wonderful times we have shared. Your presence has meant a lot to me.

In conclusion, I want to convey my heartfelt appreciation to each and every person who has been a part of my life. Your support and guidance have been indispensable, and I am immensely thankful for your constant presence throughout my endeavours.

-Mufeed KEENARI

---

# TABLE OF CONTENTS

<b>Introduction: Nickelates and Superconductivity</b> .....	10
<b>Chapter 1- State of the Art: From Bulk to Thin Film Nickelates</b> .....	13
1.1 Perovskite structure .....	14
1.2 Thin film vs bulk .....	15
1.3 Metal-insulator transition (MIT) in $RNiO_3$ .....	16
1.4 Low-valence square planar nickelates .....	18
1.5 Superconductivity in infinite layer nickelates .....	20
1.5.1 <i>Synthesis aspects</i> .....	22
1.5.2 <i>Crystal structure</i> .....	23
1.5.3 <i>Electronic structure</i> .....	24
1.5.4 <i>Role of hydrogen</i> .....	27
1.5.5 <i>Nickelate superconductivity: current challenges</i> .....	29
1.6 $K_2NiF_4$ -type rare earth nickelates .....	31
<b>Chapter 2- Investigation on the physical, chemical, and structural properties of polycrystalline <math>Nd_{0.8}Sr_{1.2}NiO_4</math> and topotactically reduced <math>Nd_{0.8}Sr_{1.2}NiO_3</math></b> .....	35
2.1 Introduction.....	36
2.2 Synthesis of polycrystalline $Nd_{0.8}Sr_{1.2}NiO_4$ and $Nd_{0.8}Sr_{1.2}NiO_3$ .....	37
2.3 Structural characterizations .....	39
2.3.1 $Nd_{0.8}Sr_{1.2}NiO_4$ .....	39
2.3.2 $Nd_{0.8}Sr_{1.2}NiO_3$ .....	41

---

2.4	Physical characterizations of $\text{Nd}_{0.8}\text{Sr}_{1.2}\text{NiO}_4$ .....	45
2.4.1	Resistivity measurement .....	45
2.4.2	Magnetoresistance (MR).....	50
2.4.3	Magnetization measurements.....	56
2.4.4	Discussion on the physical properties of $\text{Nd}_{0.8}\text{Sr}_{1.2}\text{NiO}_4$ .....	60
2.5	Physical characterizations of $\text{Nd}_{0.8}\text{Sr}_{1.2}\text{NiO}_3$ .....	61
2.5.1	Resistivity measurement .....	61
2.5.2	Magnetization measurements.....	62
2.6	SUMMARY AND DISCUSSION .....	64

**Chapter 3- Thin film nickelates:**

<b>Epitaxial growth and topotactic reduction</b> .....	67
3.1 Introduction.....	68
3.2 Preliminary works on infinite layer nickelates in CRISMAT .....	71
3.3 PLD synthesis of perovskite $\text{Pr}_{0.8}\text{Sr}_{0.2}\text{NiO}_3$ on $\text{SrTiO}_3$ (STO) substrate.....	74
3.4 Reduction of $\text{Pr}_{0.8}\text{Sr}_{0.2}\text{NiO}_3$ on $\text{SrTiO}_3$ (STO) substrate .....	81
3.5 PLD synthesis and reduction of $\text{Pr}_{0.8}\text{Sr}_{0.2}\text{NiO}_3$ on LSAT substrate .....	89
3.6 TEM on nickelate thin films .....	93
3.7 PLD synthesis and reduction of STO-capped $\text{Pr}_{0.85}\text{Sr}_{0.15}\text{NiO}_3$ films on STO substrate ..	98
3.8 SUMMARY AND DISCUSSION .....	102

**SUMMARY AND CONCLUSIONS**..... 105

**Appendix**..... 110

**References**..... 122

## LIST OF FIGURES

Figure	Description	Page
1.1	<i>Schematic crystal structures of <math>Nd_{0.8}Sr_{0.2}NiO_3</math> (left) and <math>Nd_{0.8}Sr_{0.2}NiO_2</math> (right) thin films on the <math>TiO_2</math>-terminated single-crystal <math>SrTiO_3</math> (001) substrate. Upon low-temperature reduction, the films undergo a topotactic transition from the perovskite phase to the infinite-layer phase. from ref. 11</i>	21
1.2	<i>a) Resistivity versus temperature plots of the as-grown <math>NdNiO_3</math> and <math>Nd_{0.8}Sr_{0.2}NiO_3</math> films. b) Resistivity versus temperature plots <math>NdNiO_2</math> and <math>Nd_{0.8}Sr_{0.2}NiO_2</math> films. from ref. 11</i>	22
1.3	<i>Schematic phase diagram for the electronic phases of the cuprates (top) and nickelates (bottom) from ref. 99</i>	27
1.4	<i>a) The graph shows the temperature-dependent resistivity measured for <math>Nd_{0.8}Sr_{0.2}NiO_2H_x</math> samples with different H concentrations (<math>x</math> from 0.19 to 0.44). For the <math>x</math> range of <math>0.24 &lt; x &lt; 0.26</math>, the zero-resistance superconducting state is obtained. b) Phase diagram of <math>Nd_{0.8}Sr_{0.2}NiO_2H_x</math>. Circles (squares) represent 90% (10%) of the resistivity (<math>R</math>) value at 30 K. Open triangles represent the MIT temperature</i>	29
2.1	<i>Schematic diagram shows a) Solid state synthesis steps for <math>Nd_{0.8}Sr_{1.2}NiO_4</math> b) Topotactic reduction using <math>CaH_2</math> of <math>Nd_{0.8}Sr_{1.2}NiO_4</math></i>	38
2.2	<i>XRD pattern and Rietveld refinement of the monochromated XRPD data recorded at RT for <math>Nd_{0.8}Sr_{1.2}NiO_4</math>. Corresponding crystal structure is shown (generated using Vesta)</i>	39
2.3	<i>XRD pattern and Rietveld refinement of the monochromated XRPD data recorded at RT for <math>Nd_{0.8}Sr_{1.2}NiO_3</math>. Corresponding crystal structure is shown (generated using Vesta)</i>	43

2.4	<i>TEM image of Nd<sub>0.8</sub>Sr<sub>1.2</sub>NiO<sub>3</sub>. Inset shows FFT of crystallite along (100) direction</i>	44
2.5	<i>Resistivity vs Temperature plot of Nd<sub>0.8</sub>Sr<sub>1.2</sub>NiO<sub>4</sub> fitted with eq 2.1</i>	45
2.6	<i>Projected density of states (a) La<sub>0.8</sub>Sr<sub>1.2</sub>NiO<sub>4</sub>. (b) La<sub>2</sub>NiO<sub>4</sub>. Red lines on the DOS are Ni d states and in blue O p states. Positive and negative DOS corresponds to spin-up and spin-down channels.</i>	47
2.7	<i>Projected density of states for Nd<sub>0.8</sub>Sr<sub>1.2</sub>NiO<sub>4</sub>. The negative and positive density of states corresponds to the spin-up and spin-down channels, respectively. Nd 4f states are represented in orange, O 2p states in blue, and Ni 3d states in red.</i>	47
2.8	<i>Resistivity vs Temperature plot fitted with additional term accounting Kondo effect (eq 2.2)</i>	49
2.9	<i>semi-log resistivity plot at different applied magnetic fields</i>	50
2.10	<i>a) Magnetoresistance vs applied magnetic field for Nd<sub>0.8</sub>Sr<sub>1.2</sub>NiO<sub>4</sub> at 3K, 5K ,10K and 20K b) Parabolic fit using eq 2.4 for low field (-2.5 to 2.5T)</i>	51
2.11	<i>Magnetoresistance vs applied magnetic field for Nd<sub>0.8</sub>Sr<sub>1.2</sub>NiO<sub>4</sub> at 3K, 5K ,10K and 20K</i>	53
2.12	<i>ZFC, FC Susceptibility data Nd<sub>0.8</sub>Sr<sub>1.2</sub>NiO<sub>4</sub>, Inset shows low temperature susceptibility in semi-log plot</i>	56
2.13	<i>ZFC- Susceptibility fitted with modified Curie-Weiss law.</i>	57
2.14	<i>Projected density of states on Ni 3d in red and O 2p in blue for La<sub>0.8</sub>Sr<sub>1.2</sub>NiO<sub>3</sub></i>	61

2.15	<i>Susceptibility vs temperature measured in ZFC and FC method for Nd<sub>0.8</sub>Sr<sub>1.2</sub>NiO<sub>3</sub>. Inset shows Inverse susceptibility curve, shows non-Curie-Weiss behavior till 300 K</i>	62
2.16	<i>AC-susceptibility measured in ZFC method for Nd<sub>0.8</sub>Sr<sub>1.2</sub>NiO<sub>3</sub> at different ac frequency a) Real part (<math>M'</math>) b) Imaginary part (<math>M''</math>)</i>	63
3.1	<i>a) X-ray diffraction <math>\theta</math>-<math>2\theta</math> symmetric scans Nd<sub>0.8</sub>Sr<sub>0.2</sub> and Nd<sub>0.8</sub>Sr<sub>0.2</sub>NiO<sub>2</sub> of films capped with 20-nm-thick SrTiO<sub>3</sub> layers grown on SrTiO<sub>3</sub> (001) substrates b) Resistivity versus temperature <math>\rho(T)</math> plots of the as-grown NdNiO<sub>3</sub> and Nd<sub>0.8</sub>Sr<sub>0.2</sub>NiO<sub>3</sub> films c) Resistivity as a function of temperature for the reduced films (NdNiO<sub>2</sub> and Nd<sub>0.8</sub>Sr<sub>0.2</sub>NiO<sub>2</sub>)</i>	69
3.2	<i>a) The XRD <math>\theta</math>-<math>2\theta</math> scan patterns of the Nd<sub>1-x</sub>Sr<sub>x</sub>NiO<sub>2</sub> thin films on a STO substrate b) The resistivity versus temperature (<math>\rho</math>-<math>T</math>) curves of the Nd<sub>1-x</sub>Sr<sub>x</sub>NiO<sub>2</sub> thin films with Sr doping level <math>x</math> from 0.08 to 0.3 c) Superconducting dome of Nd<sub>1-x</sub>Sr<sub>x</sub>NiO<sub>2</sub> d) The temperature dependence of the <math>R_H</math> for the Nd<sub>1-x</sub>Sr<sub>x</sub>NiO<sub>2</sub></i>	70
3.3	<i>Thin film XRD patterns of Nd<sub>0.85</sub>Sr<sub>0.15</sub>NiO<sub>3</sub> and Nd<sub>0.85</sub>Sr<sub>0.15</sub>NiO<sub>2</sub> thin films on STO substrate</i>	73
3.4	<i>Four probe resistivity measurements on Nd<sub>0.85</sub>Sr<sub>0.15</sub>NiO<sub>3</sub> and Nd<sub>0.85</sub>Sr<sub>0.15</sub>NiO<sub>2</sub> films</i>	74
3.5	<i>Schematic of Pulsed laser deposition process</i>	76
3.6	<i>Thin film XRD pattern for Pr<sub>0.8</sub>Sr<sub>0.2</sub>NiO<sub>3</sub> films a) Deposited at different oxygen pressure at temperature 700°C. b) Deposited at different temperature with oxygen pressure 0.1 mbar</i>	77
3.7	<i>a) Thin film XRD pattern for Pr<sub>0.8</sub>Sr<sub>0.2</sub>NiO<sub>3</sub> films went through different annealing conditions. b) Enlarged view of (002) peak. Dashed line indicates <math>2\theta = 48^\circ</math></i>	79

3.8	<i>Four probe electrical resistivity measurement on films corresponding to films with diffraction pattern shown in figure 3.7</i>	80
3.9	<i>a) Glove box setup in CRISMAT laboratory. b) Vacuum sealed quartz tube containing thin film sample as well as CaH<sub>2</sub> powder</i>	81
3.10	<i>Thin film XRD patterns before and after reduction on Pr<sub>0.8</sub>Sr<sub>0.2</sub>NiO<sub>3</sub> films. Dashed line indicates 2θ=48°</i>	83
3.11	<i>Figure shows thin film XRD patterns before and after consecutive reductions on Pr<sub>0.8</sub>Sr<sub>0.2</sub>NiO<sub>3</sub> films. Dashed line indicates 2θ=48°</i>	84
3.12	<i>Electrical resistivity measurement corresponding XRD pattern in blue color. Inset shows four probe contacts on the sample. Matched with color code of the resistivity plot.</i>	85
3.13	<i>a) Evolution of thin film XRD pattern upon series of reduction performed. b) Enlarged view focused on Second order diffraction peaks. Inset shows corresponding change in the out of plane lattice parameter vs peak intensity upon each reduction.</i>	87
3.14	<i>Thin film XRD pattern for Pr<sub>0.8</sub>Sr<sub>0.2</sub>NiO<sub>3</sub> on LSAT substrate deposited with different laser output energy. Patterns are vertically displaced for clarity</i>	90
3.15	<i>Thin film XRD patterns for as deposited and reduced Pr<sub>0.8</sub>Sr<sub>0.2</sub>NiO<sub>3</sub> films on LSAT substrate deposited with different laser output energy and reduced at 260°C for 3hrs. Patterns are vertically displaced for clarity</i>	91
3.16	<i>Electrical resistivity vs temperature of reduced Pr<sub>0.8</sub>Sr<sub>0.2</sub>NiO<sub>3</sub>/LSAT films at 260°C for 3hrs. Inset shows four probe contacts on the sample. Matched with color code of the resistivity plot.</i>	92
3.17	<i>a) Figure EDS mapping of Pr<sub>0.8</sub>Sr<sub>0.2</sub>NiO film on LSAT. b) Elemental concentration profile across selected area of cross section</i>	94

3.18	a) TEM cross section images of $Pr_{0.8}Sr_{0.2}NiO_3/LSAT$ b) FFTs of substrate and film	95
3.19	Mapping of 3D-ED data points collected for substrate in the reciprocal space into perovskite $a_p*a_p*a_p$ unit cell	96
3.20	Mapping of 3D-ED data points collected at 4 different regions of the film in the reciprocal space into perovskite $a_p*a_p*a_p$ unit cell.	97
3.21	a) Thin film XRD pattern for $Pr_{0.85}Sr_{0.15}NiO_3$ on STO substrate deposited with different STO capping thickness. Patterns are vertically displaced for clarity. b) Enlarged view focused on Second order diffraction peaks	99
3.22	Thin film XRD patterns for as deposited $Pr_{0.85}Sr_{0.15}NiO_3$ films on STO substrate following by capping the film with 25 unit-cell thickness of STO and corresponding reduced film XRD pattern.	100
3.23	Thin film XRD patterns for as deposited $Pr_{0.85}Sr_{0.15}NiO_3$ films on STO substrate following by capping the film with STO and corresponding reduced film XRD pattern. a) Capped with 8 u.c of STO b) Capped with 1 u.c of STO	101

---

## Introduction: Nickelates and Superconductivity

Transition metal oxides (TMOs) are known for their strongly correlated nature and versatile properties such as superconductivity [1], metal-to-insulator transition (MIT) [2], colossal magnetoresistance [3], charge and spin ordering [4], etc. Emergences of these properties in TMOs are on account of charge, spin, lattice, and orbital degrees of freedom, and the complexities arise from the strong Coulomb interactions and the consequences of partial filling of the d-shells [5]–[7].

Nickelates hold a significant position as a member of the TMO family, with their study dating back to the mid-20th century. The discovery of nickelates was spurred by their structural resemblance to other perovskite-structured oxides, such as high-temperature superconductors, thus initiating early research aimed at understanding their fundamental physical properties and their connection with other oxides. In the 1980s and 1990s, researchers began to delve deeper into the electronic and magnetic properties of nickelates. It was during this time that the unique and interesting behavior of these materials began to emerge, including metallic behavior and metal-insulator transition (MIT) [8]–[10], which set them apart from other oxide materials. This sparked a renewed interest in nickelates and led to a surge in research aimed at understanding the underlying mechanisms behind these properties. Researchers focused on optimizing the electronic and magnetic properties of nickelates through the manipulation of their crystal structure, doping, and other factors. In recent years, the discovery of quasi-two-dimensional nickelates with superconducting properties has sparked further interest in this particular system [11].

*‘Superconductivity; a giant jigsaw puzzle’*

Superconductors, as the name indicates, are a class of materials that exhibit zero electrical resistance and expel magnetic flux below a specific temperature referred to as critical temperature ( $T_c$ ). The history of superconductors begins with the liquefaction of helium (4.15K) by Heike Kamerlingh Onnes in 1912, that allowed the extremely low temperature regime to become accessible. A year after this achievement, Kamerlingh observed the element Mercury behaves as a perfect conductor with no electrical resistance below 4.2K and named this phenomenon

superconductivity, for which he was awarded the Nobel Prize in Physics for the year 1913. Theoreticians and experimentalists extensively and rigorously studied this phenomenon with the goal of unraveling the physics behind this phenomenon by designing materials that can superconduct at higher temperatures.

In the mid-twentieth century, scientists came up with two important theories that could explain the 'conventional' superconductivity. The macroscopic properties of superconductors are explained by the phenomenological Ginzburg-Landau (G-L) theory, which is a theoretical framework that incorporates principles from Landau's theory of second-order phase transitions and the quantum mechanical concept of wave functions. This theory effectively explains the behavior of superconductors on a macroscopic level, providing insight into their unique characteristics and properties [12]. In 1957, the pioneering microscopic theory of superconductivity was postulated by Bardeen, Cooper, and Schrieffer, referred to as the BCS theory. This theory advanced the notion that superconductivity is facilitated by the formation of Cooper pairs of electrons, which engage in interactions through the exchange of phonons, thus accounting for the phenomenon of superconducting current as a superfluid of Cooper pairs [13]. This theory played a pivotal role in developing a microscopic understanding of the underlying mechanism of superconductivity. It has been recognized as a seminal contribution to the field of superconductivity and has laid the foundation for the advancement of superconductor technology. However, the BCS theory had a limitation of restricting the maximum transition temperature ( $T_c$ ) for superconductivity to around 30 K. This theory was widely accepted as true until the discovery of superconductivity in lanthanum barium copper oxide (LBCO) in 1986, which had a  $T_c$  of 35K [14], thereby challenging the validity of the BCS theory. This opened a new realm of superconductors, known as high- $T_c$  superconductors, which do not follow the conventional BCS theory and are categorized as "unconventional" superconductors. Later,  $T_c$  increased above 90K by replacing lanthanum with yttrium, forming yttrium barium copper oxide (YBCO) [15]. Iron-based layered compounds, a new family of high  $T_c$  superconductors, were discovered in the year 2008 with a  $T_c$  above 40 K, later increased to 55 K by replacing some elements in the system [16], [17]. Advancement in high  $T_c$  superconductivity relies on the understanding of current copper and iron-based high  $T_c$  superconductors. Which in turn relies on finding similar superconducting systems and studying them.

As we lack a comprehensive model to explain the phenomenon of high- $T_c$  superconductivity in cuprates, researchers have focused on identifying key features that contribute to this behavior. Despite the ongoing enigma surrounding the mechanism of HTS in cuprates, there is a widespread agreement that the key structural unit, the  $\text{CuO}_2$  plane, which demonstrates distinctive quasi-two-dimensional (2D) physics of the  $dx^2-y^2$  orbital, holds a fundamental position in the HTS process [18]. In pursuit of cuprate-analog superconductors, researchers have turned their attention to nickelates, specifically systems with nickel valency of  $\text{Ni}^{1+}$ , which possess a  $d^9$  electronic configuration similar to  $\text{Cu}^{2+}$  in cuprates. Efforts to find cuprate analog superconductivity in nickelates [19]–[28] reached a milestone with the discovery of superconductivity in  $\text{Nd}_{0.8}\text{Sr}_{0.2}\text{NiO}_2$  with a  $T_c \sim 15\text{K}$  [29]. This led to a global race to investigate and explore the family of nickelates further, which might fill a few pieces of this giant jigsaw puzzle.

# State of the Art: From Bulk to Thin Film Nickelates

Transition metal oxides (TMOs) exhibit a rich physics due to the d electron valence states of the transition metal (TM) cations located at the Fermi level. Understanding the low-energy physics of rare-earth nickelates is essential to comprehend their properties. The d states hybridize with the oxygen p states, and the hybridization strength depends on the orbital overlap of the p and d states and their energy difference. This hybridization can be adjusted by external parameters that rely on the distance between the TM site and oxygen. The intrinsic properties of these materials depend significantly on the rotation angles of the oxygen octahedra, as both p and d orbitals are highly directional [29].

## 1.1 Perovskite structure

A perovskite structure is a type of crystal structure that has the general formula  $ABX_3$ , where A and B are cations of different sizes, and X is an anion that bonds to both A and B. In the perovskite structure, the A cation is larger than the B cation and occupies the corners of a cubic unit cell. The B cation is smaller and occupies the center of the unit cell. The X anion is located at the midpoints of the edges of the unit cell, forming an octahedron around the B cation. Distortion and geometric stability of a perovskite structure is characterized by a dimensionless factor called Goldschmidt tolerance factor ( $t$ ) [30] and can be described as

$$t = \frac{r_A + r_O}{\sqrt{2} (r_B + r_O)}$$

$r_A$ ,  $r_B$  and  $r_O$  are the ionic radii of the A-site cation, B-site cation, and oxygen anion, respectively.

The value of the Goldschmidt tolerance factor determines whether a perovskite material has a cubic, tetragonal, or orthorhombic crystal structure. For  $t = 1$ , the perovskite has a cubic structure, while for  $t < 1$ , it has a tetragonal structure. When  $t$  is significantly less than 1, the perovskite material is said to be under "octahedral tilting" which is the result of distortions of the oxygen octahedra in the crystal structure. When  $t$  is significantly greater than 1, the perovskite material is said to be overbonded, which describes the situation when the A cation is too large to fit into the cavities of the  $BX_3$  framework, resulting in a high degree of bond strain and structural instability [30].

In perovskite thin films, the substrate on which the film is grown can affect the lattice constant and, thus, the Goldschmidt tolerance factor. For example, the lattice constant can be compressed or stretched due to the lattice mismatch between the film and substrate, which can modify the value of  $t$  and affect the crystal structure of the perovskite.

## 1.2 Thin film vs bulk

Rare-earth nickelates have been widely studied in both thin-film and bulk form, and there are some notable differences in their physical properties. While both thin-film and bulk nickelates are important for understanding the properties of this class of materials, it is important to be aware of certain effects on thin-film and to consider the differences between thin-film and bulk properties when interpreting experimental data. Several factors can significantly affect the structural, electronic, magnetic, and transport properties of thin films, which makes it different from their bulk counterparts [31]. Understanding these differences is important for developing and optimizing thin film growth techniques and for tailoring the properties of nickelate thin films for specific applications.

**Strain:** One of the major differences between thin film and bulk nickelates is the presence of strain in thin films. Thin films can experience strain due to lattice mismatch between the film and substrate, which can affect their structural and electronic properties. For example, strain can induce structural phase transitions and change the electronic correlations and magnetic ordering of nickelates [32]. Bulk nickelates, on the other hand, do not normally experience this type of strain.

**Surface effects:** Thin films also have a higher surface-to-volume ratio compared to bulk materials, which can lead to significant changes in their physical properties. Bulk nickelates, which have a much smaller surface area, do not typically exhibit these surface effects to the same extent.

**Dimensionality:** Thin films are inherently two-dimensional (2D) or quasi-2D, while bulk materials are three-dimensional (3D). This can lead to significant differences in the electronic and magnetic properties of the materials. One important consequence of the reduced dimensionality of thin films is the phenomenon of quantum confinement. When the thickness of a thin film is reduced to a few nanometers or less, the electronic and optical properties of the material can be significantly altered

due to the confinement of the electronic wavefunctions in the out-of-plane direction. This can lead to a variety of interesting phenomena, such as the quantization of energy levels and the enhancement of quantum mechanical effects.

### 1.3 Metal-insulator transition (MIT) in $\text{RNiO}_3$

Metal-insulator transition (MIT) is a phenomenon in which some materials change their electrical conductivity from metallic to insulating as a function of temperature, pressure, magnetic field, or chemical doping [33]–[35]. The MIT in rare earth nickelates is accompanied by structural, electronic, and magnetic changes and is influenced by electron-lattice coupling, orbital ordering, spin state, and interface effects. The MIT in rare earth nickelates can be modulated by growing thin films and heterostructures of different nickelate compositions and orientations. These artificial structures can reveal new physical phenomena and enable novel applications in oxide electronics, such as field-effect transistors, memristors, and neuromorphic devices [36]–[38].

Rare earth nickelates have a cubic perovskite structure at high temperatures but undergo a series of distortions as they are cooled down. The most important distortion is the breathing mode of the oxygen octahedra surrounding the Ni atoms, which causes a change in the Ni-O bond lengths and induces a charge disproportionation on the Ni sites. This leads to a lowering of the crystal symmetry from a high-temperature orthorhombic metallic phase ( $Pnma$  symmetry) to a low-temperature monoclinic insulating phase ( $P2_1/n$  symmetry). The MIT occurs at a critical temperature ( $T_{\text{MI}}$ ) that depends on the rare earth cation size and the oxygen octahedra rotation amplitude. The smaller the cation size and the larger the rotation amplitude, the higher the  $T_{\text{MI}}$  [37]. The MIT in rare earth nickelates is also accompanied by a magnetic phase transition from a paramagnetic state to an unusual antiferromagnetic order, in which the Ni spins form zigzag chains along the diagonal direction of the  $\text{NiO}_2$  planes. The magnetic order is driven by the super exchange interaction between the Ni-3d orbitals mediated by the O-2p orbitals. The magnetic transition temperature ( $T_{\text{N}}$ ) is slightly lower than  $T_{\text{MI}}$ , indicating a weak coupling between the electronic and magnetic degrees of freedom [38].

The origin of the MIT in rare earth nickelates has been debated for a long time, and different models have been proposed to explain it. One of the key issues is whether these materials obey a conventional positive charge-transfer picture, in which the charge gap is determined by the energy difference between the O-2p and Ni-3d orbitals, or a negative charge-transfer picture, in which the charge gap is determined by the energy difference between the lower and upper Hubbard bands of Ni-3d orbitals. Recent experimental and theoretical studies have provided strong evidence for the negative charge-transfer scenario, in which the ground state of these materials has abundant oxygen holes and a Ni-3d<sup>8</sup> configuration [38]. This implies that the MIT is driven by a correlation-induced localization of Ni-3d electrons rather than by a structural distortion.

One of the aspects that makes the MIT in rare earth nickelates interesting is how it can be affected by the dimensionality and the interface effects of thin film structures. Compared to bulk samples, thin films of nickelates can exhibit different values of  $T_{MI}$  and  $T_N$  depending on the strain induced by the substrate, the film thickness, and the presence of capping layers or superlattice configurations. For example, epitaxial strain can enhance or suppress the oxygen octahedra rotations and modulate the Ni-O bond lengths, thus influencing the charge disproportionation and the electronic localization. Moreover, thin films can show a reduced dimensionality that can alter the orbital occupancy and the magnetic coupling of Ni-3d electrons. Furthermore, heterostructures of nickelates with other perovskites can create novel interface phenomena such as charge transfer, orbital reconstruction, magnetic proximity, or superconductivity [32], [39]. The substrate on which rare earth nickelate thin films are grown can influence their electronic and structural properties. This can lead to changes in the MIT characteristics of the films. For example, when grown on a substrate with a large lattice mismatch, nickelate films can experience strain, which affects their crystal structure and can lead to changes in MIT behavior. On the other hand, when grown on a substrate with a lattice parameter that closely matches that of the nickelate, the films can exhibit improved crystallinity and more consistent MIT characteristics [40]–[42].

Some of the latest findings on metal-insulator transition in rare earth nickelates include elucidating the structurally triggered mechanism of this transition from first-principles calculations that showed that the transition arises from the softening of an oxygen-breathing distortion, which is induced by oxygen-octahedra rotation motions [37]. The calculations also developed a Landau

model that accounted for the evolution of the transition temperature as a function of the rare-earth cation size and suggested ways to tune the transition by acting on oxygen rotation motion [37].

The antiferromagnetic metal phase in an electron-doped nickelate was discovered by using molecular beam epitaxy to grow thin films of  $\text{NdNiO}_3$  with a small amount of La doping. The films were characterized by various techniques such as X-ray diffraction, transport measurements, angle-resolved photoemission spectroscopy, and scanning transmission electron microscopy. The results showed that the electron doping preserved the magnetic order on the Ni sites but induced a metallic phase with a gapped Fermi surface due to an electronic reconstruction driven by bond disproportionation. The films also exhibited a large zero-field planar Hall effect, attributed to spin-orbit coupling effect arising from the non-collinear antiferromagnetic order [43].

The evidence for ground-state oxygen holes and a negative charge-transfer scenario in rare earth nickelates was obtained using resonant inelastic X-ray scattering experiments on thin films of  $\text{NdNiO}_3$  and  $\text{LaNiO}_3$  grown on different substrates. The experiments revealed that the charge gap in these materials was determined by the energy difference between the lower and upper Hubbard bands of Ni-3d orbitals rather than by the energy difference between the O-2p and Ni-3d orbitals. The experiments also showed that the ground state of these materials had abundant oxygen holes and a Ni-3d<sup>8</sup> configuration, implying that the metal-insulator transition was driven by a correlation-induced localization of Ni-3d electrons [36].

## 1.4 Low-valence square planar nickelates

Low-valence square planar nickelates (LVSP) are of the form  $\text{R}_{n+1}\text{Ni}_n\text{O}_{2n+2}$  (R=La, Pr and Nd, n=2, 3 ...), where Ni has a  $(1+[1/n])^+$  valence state and adopt a square planar coordination geometry with oxygen. This structure is similar to the copper-oxygen planes in high-temperature superconducting cuprates, which has led to the investigation of low-valence nickelates as potential superconducting materials. Nickel typically adopts an octahedral coordination geometry due to the 3d<sup>8</sup> electronic configuration that results in a high-spin d<sup>8</sup> configuration. However, the square planar coordination geometry is preferred for low-valence nickel ions with a d<sup>9</sup> electronic configuration.

Stabilizing this low-valence square planar nickelate structure is challenging due to the tendency of nickel to form octahedral coordination, which is energetically more favorable. Additionally, the  $d^9$  configuration is highly unstable and prone to oxidation, which can lead to the formation of undesirable nickel oxide phases.

Several research groups have undertaken the synthesis of  $\text{LaNiO}_2$  compounds in thin film as well as bulk forms. The initial synthesis of these materials succeeded in the early 1980s, preceding the groundbreaking cuprate research of Bednorz and Müller [14]. Nickelates typically exhibit octahedral coordination, characterized by a network of Ni atoms surrounded by four oxygen in one plane and two additional oxygen above and below it, called apical oxygen. In 1983, a group of researchers discovered that by starting with a 3D perovskite structure,  $\text{LaNiO}_3$ , and treating it with hydrogen gas, it could be reduced (by removing apical oxygen from Ni-O octahedra) to a 2D planar structure,  $\text{LaNiO}_2$  [44]. In the perovskite phase, the structure consists of alternating planes of LaO and  $\text{NiO}_2$ . By reducing the perovskite, roughly a third of the oxygen atoms (the apicals) are removed, leaving behind a  $\text{NiO}_2$  framework with planes separated only by La atoms. This type of phase change by means of low-temperature reduction is called topotactic reduction. The resulting layered structure ( $\text{LaNiO}_2$ ) possesses both a square-planar geometry and a transition-metal oxidation state similar to that of cuprates. Topotactic transitions differ fundamentally from conventional chemical doping, as they entail a long-range ordered structural phase change with a topotactic nature. Therefore, this approach serves as an effective means of creating new oxide materials or introducing new oxide phases. Consequently, it allows for the exploration of previously unseen properties through the fabrication of novel materials. Unlike traditional synthesis methods pushed by means of thermodynamics, topotactic transitions are predominantly driven through kinetics and can arise at low temperatures. This function is particularly substantial because the low synthesis temperature of topotactic transitions permits for the stabilization of metastable metallic oxides that would in any other case be inaccessible at higher temperatures.

The synthesis of polycrystalline powders in 1983 and subsequent attempts faced challenges due to the high surface-to-volume ratios and random orientation of crystals, leading to issues such as the introduction of defects and decomposition. A significant advancement was the replacement of  $\text{H}_2$  gas with a metal-hydride reducing agent, which improved safety and reliability [45]. The process of topotactic reduction, whereby oxygen atoms are removed from layered nickelate

structures, has emerged as a promising method for achieving low-valence nickelates with unique electronic and magnetic properties. However, it was not until 2009 that the epitaxial growth of a single-crystal thin film of the reduced planar structure was achieved by growing the film on a strontium titanite ( $\text{SrTiO}_3$ ) substrate, and the reaction process became more controllable [46].

## 1.5 Superconductivity in infinite layer nickelates

After successfully reducing  $\text{LaNiO}_3$  to  $\text{LaNiO}_2$  using  $\text{CaH}_2$ , multiple research groups were able to successfully follow the recipe of reduction on thin films and bulk nickelates [28], [45], [47]–[50]. By mid-2019, superconductivity with a critical temperature ( $T_c$ ) of approximately 15K was observed in thin films of  $\text{Nd}_{0.8}\text{Sr}_{0.2}\text{NiO}_2$ , realized by  $\text{CaH}_2$  based reduction of  $\text{Nd}_{0.8}\text{Sr}_{0.2}\text{NiO}_3$ , deposited by pulsed laser deposition (PLD) on strontium titanate (STO) substrates and capped by STO [11]. However, synthesizing high-quality superconducting films still remains a challenging task that requires optimization of multiple growth parameters to avoid unwanted phases of multilayer nickelates and other secondary phases [51]. The initial variation in  $T_c$  among these samples suggests subtle differences in composition or structure, but subsequent research improved the synthesis process and demonstrated a  $T_c(x)$  with a superconducting dome similar to, and with comparable hole concentrations as, the cuprates [52], [53].

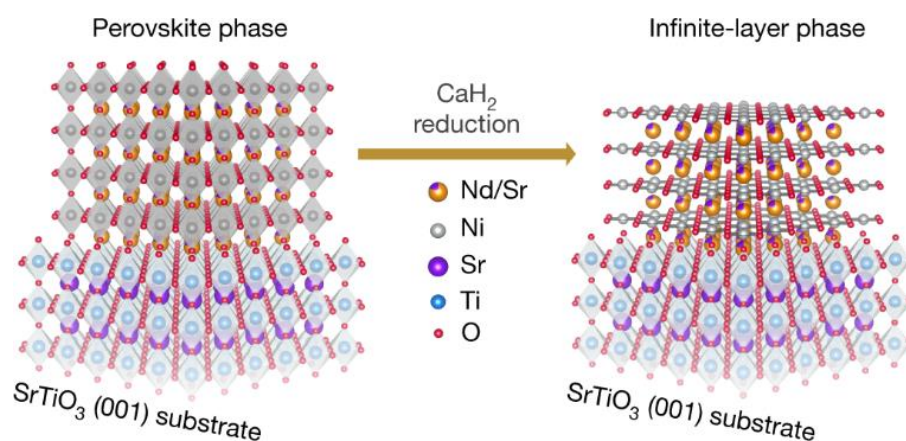
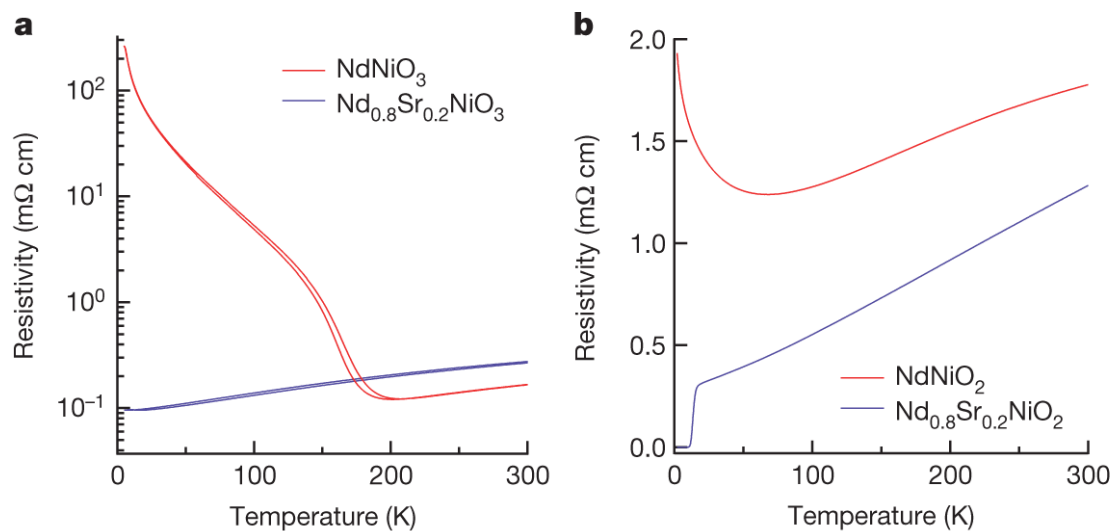


Figure 1.1

*Schematic crystal structures of  $\text{Nd}_{0.8}\text{Sr}_{0.2}\text{NiO}_3$  (left) and  $\text{Nd}_{0.8}\text{Sr}_{0.2}\text{NiO}_2$  (right) thin films on the  $\text{TiO}_2$ -terminated single-crystal  $\text{SrTiO}_3$  (001) substrate. Upon low-temperature reduction, the films undergo a topotactic transition from the perovskite phase to the infinite-layer phase. from ref. 11*



*Figure 1.2*

*a) Resistivity versus temperature plots of as-grown NdNiO<sub>3</sub> and Nd<sub>0.8</sub>Sr<sub>0.2</sub>NiO<sub>3</sub> films.*

*b) Resistivity versus temperature plots NdNiO<sub>2</sub> and Nd<sub>0.8</sub>Sr<sub>0.2</sub>NiO<sub>2</sub> films. from ref. 11*

The superconductivity in infinite layer nickelates was extended by realizing superconductivity in systems with different rare earth elements (Pr, La), different cation substitutions (Ca), and on a different substrates (LSAT) [54]–[57]. Additionally, the observation of superconductivity in infinite-layer Ca-doped LaNiO<sub>2</sub> implies that the appearance of superconductivity in infinite-layer nickelates is not reliant on the 4f electrons of the rare-earth element and suggests that higher T<sub>c</sub> in infinite-layer nickelates can be stabilized using smaller rare-earth ions. The discovery is also encouraging for the field because it shows that superconductivity may not be reliant on the thin-film geometry, which means that the creation of superconducting bulk crystals should be possible.

### 1.5.1 Synthesis aspects

Only five research teams have independently reported the successful synthesis of superconducting infinite-layer nickelates thin films so far\*. Most of the experiments were reported by Harold Hwang's group at Stanford University, who first found superconductivity in  $\text{Nd}_{1-x}\text{Sr}_x\text{NiO}_2$  thin films. The other groups are Hai-Hu Wen's group at Nanjing University [58]–[60], Ariando's group at the National University of Singapore [61]–[63], Xingjiang Zhou's group at Chinese Academy of Science [64], [65] and Zhiqi Liu's group at School of Beihang University [66], [67]. The only method that has successfully transformed  $\text{Nd}_{1-x}\text{Sr}_x\text{NiO}_3$  into superconducting  $\text{Nd}_{1-x}\text{Sr}_x\text{NiO}_2$  so far is the soft chemical topotactic reduction. This process typically involves  $\text{CaH}_2$  powder as a reducing agent,  $\text{Nd}_{1-x}\text{Sr}_x\text{NiO}_3$  samples wrapped in aluminum foil, and a vacuum environment such as sealed glass or quartz tubes. For instance, for the first report of superconducting  $\text{Nd}_{1-x}\text{Sr}_x\text{NiO}_2$  thin films, they deposited  $\text{Nd}_{1-x}\text{Sr}_x\text{NiO}_3$  films on  $\text{TiO}_2$ -terminated  $\text{SrTiO}_3$  substrates by pulsed laser deposition (PLD) with epitaxial  $\text{SrTiO}_3$  capping layers [68]. Then, they vacuum-sealed the  $\text{Nd}_{1-x}\text{Sr}_x\text{NiO}_3$  samples loosely covered by aluminum foils with  $\text{CaH}_2$  powder in a Pyrex glass tube and heated it to 260-280°C for 4-6hrs. Finally, they obtained superconducting nickelate thin films with a thickness range of 9-11nm. A similar reduction procedure was used by another group on 6nm thick  $\text{Nd}_{1-x}\text{Sr}_x\text{NiO}_3$  thin films grown by reactive molecular beam epitaxy, without  $\text{SrTiO}_3$  capping layers and achieved superconducting  $\text{Nd}_{1-x}\text{Sr}_x\text{NiO}_2$  films. A slightly different method for reduction was employed by Ariando's group at the National University of Singapore. They performed solid chemical reduction reactions in a PLD chamber instead of a vacuum glass tube. The PLD chamber contained aluminum foils that were wrapped in  $\text{CaH}_2$  powder and pre-grown  $\text{Nd}_{1-x}\text{Sr}_x\text{NiO}_3$  thin films with a thickness of 35nm. The chamber was then heated for 80-120min at 340-360°C [63]. The superconducting dome of  $\text{Nd}_{1-x}\text{Sr}_x\text{NiO}_2$  appears to be narrower in comparison to  $\text{Pr}_{1-x}\text{Sr}_x\text{NiO}_2$  and  $\text{La}_{1-x}\text{Sr}_x\text{NiO}_2$ . This observation suggests a potential connection between the range of superconductivity and the modulation of the lattice constant. The discovery of superconductivity in Cu- and Fe-based materials was first made in their bulk forms. However, a major challenge in this novel nickelate superconductivity is that bulk nickelates have not shown any superconductivity yet [69]–[72]. This

---

\* As of 03/30/2023

has hindered the progress of the novel infinite-layer Ni-based superconductors because many techniques that can analyze bulk materials are more available, such as neutron diffraction, nuclear magnetic resonance, and angle-resolved photoemission spectroscopy that can directly map out electronic band structures

### 1.5.2 Crystal structure

The infinite layer nickelates have a  $P4/mmm$  crystal structure consisting of edge-sharing  $NiO_4$  squares forming a nearly perfect square planar coordination of the Ni atoms. The structure has a 4-fold rotational symmetry axis along the c-axis and a mirror plane perpendicular to the c-axis. The primitive cell of  $P4/mmm$  consists of a single nickelate layer and has a lattice parameter  $a$  that is equal to the in-plane distance between the nickel atoms in the layer, while the c-axis lattice parameter is equal to the distance between adjacent nickelate layers along the c-axis. The cuprate-like band dispersion is a key feature of the electronic structure in the  $P4/mmm$  structure, which arises from the edge-sharing  $NiO_4$  square network and allows for strong covalent bonding between the Ni atoms and the neighboring O atoms. Epitaxial strain can induce structural distortions, such as antiphase rotations of the  $NiO_4$  squares around the c-axis, leading to a  $P4/mmm \rightarrow I4/mcm$  structural transition. For example, if a thin film of  $LaNiO_2$  is grown on a  $SrTiO_3$  substrate, the lattice parameter of the substrate will impose a strain on the film, which can affect its electronic and structural properties. In this context, the lattice parameter of  $SrTiO_3$  is  $3.905\text{\AA}$ , while the lattice parameters of bulk  $LaNiO_2$  are  $a = 3.96\text{\AA}$  and  $c = 3.37\text{\AA}$ . Thus, for thin films of  $LaNiO_2$  grown on  $SrTiO_3(001)$  with the c-axis oriented perpendicular to the substrate, the epitaxial strain yields a value of  $-1.4\%$  [73]–[76].

Epitaxial strain in thin films is not limited to changes in the in-plane lattice parameter, as it can also affect the out-of-plane lattice parameter. In general, a reduction of the in-plane lattice parameter is accompanied by an increase in the out-of-plane lattice parameter as the system tries to relax the stress in that direction. This means that an in-plane compression at the interface between the film and substrate will result in out-of-plane tensile strain. Conversely, in-plane tensile strain due to a different substrate can be expected to produce an out-of-plane compression.

The process of relieving epitaxial strain in thin films is intricate and influenced by factors such as the film's thickness and distance from the interface. Eventually, the lattice parameters of the film will restore to their bulk values with increasing film thickness. This has been studied in the case of  $\text{Nd}_{1-x}\text{Sr}_x\text{NiO}_2$  films on STO, where the  $c$  lattice parameter was observed to be decreasing as the thickness increased, and the superconducting transition temperature ( $T_c$ ) has been found to correlate with the decrease in the strain, increasing from 6 to 13 K [77]. In contrast, for  $\text{Pr}_{1-x}\text{Sr}_x\text{NiO}_2$  thin films grown on  $(\text{LaAlO}_3)_{0.3}(\text{Sr}_2\text{AlTaO}_6)_{0.7}$  (LSAT) substrate, the  $T_c$  has been reported to increase compared to  $\text{SrTiO}_3$  substrate, for 8nm-thick thin films in both cases. This increase has been attributed to the additional strain induced by the LSAT substrate. However, the degree of in-plane compressive (out-of-plane tensile) strain seems to play a critical role in determining the  $T_c$  in this case [78], [79]. The observed differences in the  $T_c$  of these films may be attributed to various factors such as stoichiometry, sample quality, and growth conditions.

### *1.5.3 Electronic structure*

The electronic properties of nickelates have been subject to intensive research, with a particular focus on their superconducting behavior. While nickelates and cuprates share some similarities in their electronic structure, such as the presence of partially filled  $d$ -orbitals in transition metal ions, they also display important differences [80]. A notable difference is that the parent cuprates exhibit antiferromagnetic insulating behavior, while the parent infinite-layer nickelates are metallic and lack long-range magnetic order [81], [82]–[85]. First-principles calculations indicate that the electronic structure of nickelates is distinct, with different energy levels of oxygen  $p$  orbitals and the direct doping of holes into nickel  $d$  orbitals. These differences suggest that nickelates may be better understood as a self-doped Mott insulator, with two types of charge carriers, namely the itinerant  $\text{Nd-5d}$  electrons and the  $\text{Ni-3d}$  holes, on a lattice of magnetic  $\text{Ni-3d}$  moments [86]. The interplay between the Kondo effect and the Mott physics in nickelates has led to the proposal of an extended  $t$ - $J$ - $K$  model for their low-energy properties [81]. The  $t$  term represents the hopping of electrons between the  $\text{Ni-3d}$  orbitals on the square lattice. The  $J$  term represents the antiferromagnetic exchange interaction between the localized  $\text{Ni}$  spins. The  $K$  term represents the Kondo coupling between the  $\text{Ni}$  spins and the conduction electrons from the  $\text{Nd-5d}$

orbitals. The extended t-J-K model is proposed to describe the low-energy properties of correlated electron systems, such as nickelates. It is an extension of the t-J model, which describes the motion of electrons in a strongly correlated system where double occupancy is forbidden. The K term in the extended t-J-K model accounts for the Kondo effect, which arises from the coupling between the localized d-electrons and the itinerant electrons. This model includes additional terms to describe the effects of electron-electron interactions, such as the on-site Coulomb repulsion, and allows for the study of the interplay between Mott physics and Kondo physics in correlated electron systems [87]–[90]. Experimental measurements using Raman scattering and resonant inelastic X-ray scattering (RIXS) have confirmed the presence of hybridization between Ni-3d and Nd-5d orbitals, as well as the suppression of the antiferromagnetic long-range order due to the Kondo coupling, where a magnetic impurity interact with non-magnetic metal resulting in impurity spins are screened by the conduction electrons [89], [91]–[93]. The parent or underdoped nickelate compounds may be viewed as a Kondo semimetal, while for large hole doping, the Ni-3d electrons become more itinerant, and the Kondo effect breaks down, leading to an abrupt change of the charge carriers. Theoretical studies have shown that the Fermi surface of infinite layer nickelates is similar to that of copper oxides, with the exception of additional bands around the Fermi level of predominant Nd-5d character. These bands overlap with the Ni- $d_{x^2-y^2}$  orbital, resulting in a multi-orbital electronic structure [80], [86], [94], [95]. Undoped infinite layer NdNiO<sub>2</sub> behaves like doped cuprates due to the presence of these electron pockets, which leads to a hole-doped Ni- $d_{x^2-y^2}$  orbital [96]. According to another first-principle study of the Sr-doping effect in Nd<sub>1-x</sub>Sr<sub>x</sub>NiO<sub>2</sub>, the comparison of the band structures at the two doping endpoints suggests that Sr doping in infinite-layer NdNiO<sub>2</sub> is a nontrivial process involving redistribution of charge carriers on different bands that differs from a simple hole-injection or rigid band shift (RBS) picture [97]. So, the self-doping effect in NdNiO<sub>2</sub> is strongly suppressed during the doping process.

The valence of the Ni cation in NdNiO<sub>2</sub> is about 1<sup>+</sup>, which means that the attraction from the nucleus is small, leading to the lifting of the energy level of the 3d orbitals. This, in turn, increases the charge-transfer energy between the Ni-3d and O-2p orbitals, reducing the hybridization between them. The charge transfer energy in nickelates is much larger than in cuprates, which puts them outside the bounds of superconductivity in the cuprate context [96].

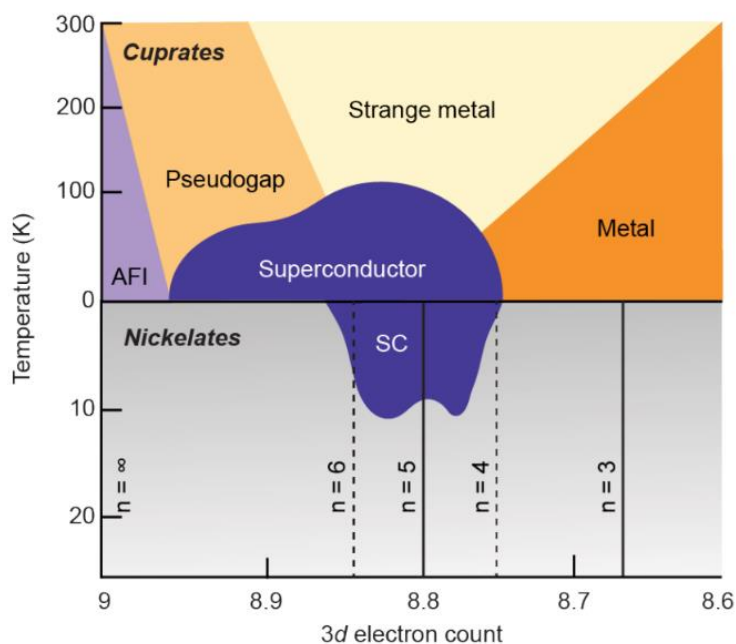


Figure 1.3: Schematic phase diagram for the electronic phases of the cuprates (top) and nickelates (bottom) from ref. 99

A different study put forward the idea that the metallic non-cuprate-like behavior observed in undoped infinite layer nickelate materials can be attributed to the strong Ni-R-Ni off-plane hopping (process of electrons moving from one atom to another in a lattice), resulting in extremely dispersive R-d bands that strongly hybridize with the Ni-d occupied bands. The R-d bands cross the Fermi level, leading to a deviation from half-filling in the Ni- $d_{x^2-y^2}$  band through a self-doping mechanism [98]. The study also demonstrated that the suppression of Ni-Ni off-plane hopping through structural modifications can result in an antiferromagnetic insulating state in RNiO<sub>2</sub> materials in the two-dimensional limit. This same phase can occur naturally in finite-n members of the layered nickelate family, including the recently discovered n=5 layered nickelate superconductor, without requiring any structural changes [99]. These findings suggest that a crucial aspect of the phase diagram of superconducting cuprates, namely the parent insulating antiferromagnetic phase, may also exist in the entire series of layered nickelates. Although the  $n = \infty$  compound is inhibited from exhibiting this phase due to the significant dispersion of off-plane bands, it can be manifested by decreasing dimensionality.

The nature of the insulating state in LVSP nickelates, whether it is a Mott-Hubbard or a charge transfer insulator, has been a topic of debate among researchers. Some studies have supported the Mott-Hubbard picture due to the larger separation between the 3d and O-2p orbitals,

which leads to less metal-ligand hybridization [80], [100]. Density functional theory (DFT) calculations on d9 nickelates have also supported the Mott-Hubbard picture [101]–[103].

In a recent study using resonant inelastic X-ray scattering (RIXS) at the Ni-L2 edge, the electronic structure and charge order of the low-valence nickelate,  $\text{La}_4\text{Ni}_3\text{O}_8$  were investigated [104]. The researchers developed an empirical model for the charge order and validated it using Q-resolved spectroscopy at the charge-order wave-vector. This technique involves measuring the scattering of X-rays or neutrons at different momentum transfers (Q values) and analyzing the energy dependence of the scattered signal to obtain information about the electronic and magnetic properties of the material, such as charge ordering, spin correlations, and band structure.

The study revealed that, unlike cuprates, where the spatial charge modulation mainly arises from ligand orbitals, the charge order in  $\text{La}_4\text{Ni}_3\text{O}_8$  primarily originates from the Ni sites due to the larger charge-transfer energy in low-valence nickelates. The Ni- $3d_{x^2-y^2}$  and O- $2p\sigma$  orbitals were found to play a crucial role in determining the low-energy physical properties of low-valence nickelates, while the Ni  $3d_{z^2-r^2}$  and rare-earth 5d orbitals fine-tune the electronic structure. These findings suggest that low-valence nickelates exhibit multiorbital physics, indicating that several ground states are close in energy. This complexity may lead to a richer phenomenology compared to their cuprate counterparts, while charge order remains an intrinsic characteristic of these strongly correlated materials.

The lack of long-range magnetic order led to the initial assumption that magnetism was not a critical ingredient for superconductivity in  $\text{RNiO}_2$ -based systems, despite many theories linking superconductivity in cuprates to strong antiferromagnetic correlations. Recent experiments have shown the presence of strong antiferromagnetic correlations in  $\text{NdNiO}_2$ , and NMR and muon spectroscopy studies have also supported this finding [89], [105], [106].

#### *1.5.4 Role of hydrogen*

Theoretical studies have posited the existence of topotactic hydrogen in infinite-layer nickelates obtained by metal hydride-based topotactic reduction. The incorporation of hydrogen could exert a significant influence on the electronic and magnetic properties of these reduced nickelates, as an example, the realization of a two-orbital Mott insulator via  $\text{LaNiO}_2\text{H}$  [107], [108].

A study conducted previously detected a suggestion of hydrogen incorporation in topotactically reduced  $\text{NdNiO}_3$  films, which demonstrated an oxyhydride  $\text{NdNiO}_{3-x}\text{H}_y$  phase with a defect-fluorite structure in the surface region [109]. Furthermore, topotactic hydrogen can be found in  $\text{SrTiO}_3$  thin films, which are commonly employed as substrates and capping layers for infinite-layer nickelate films, thereby furnishing another conceivable avenue for the inclusion of hydrogen in infinite-layer nickelate thin films [110].

A recent study confirmed that hydrogen plays a critical role in superconductivity in nickelates by enhancing the electron correlation and inducing a charge transfer between Ni and O orbitals [111]. They used Secondary-Ion Mass Spectrometry (SIMS), which is a technique used to study the composition of solid surfaces and thin films. It works by bombarding the surface of a specimen with a focused beam of primary ions, which sputters atoms and molecules from the surface. These ejected particles are then ionized, separated, and detected by a mass spectrometer. It is important to note that SIMS is very sensitive to the mass of elements, but it cannot determine

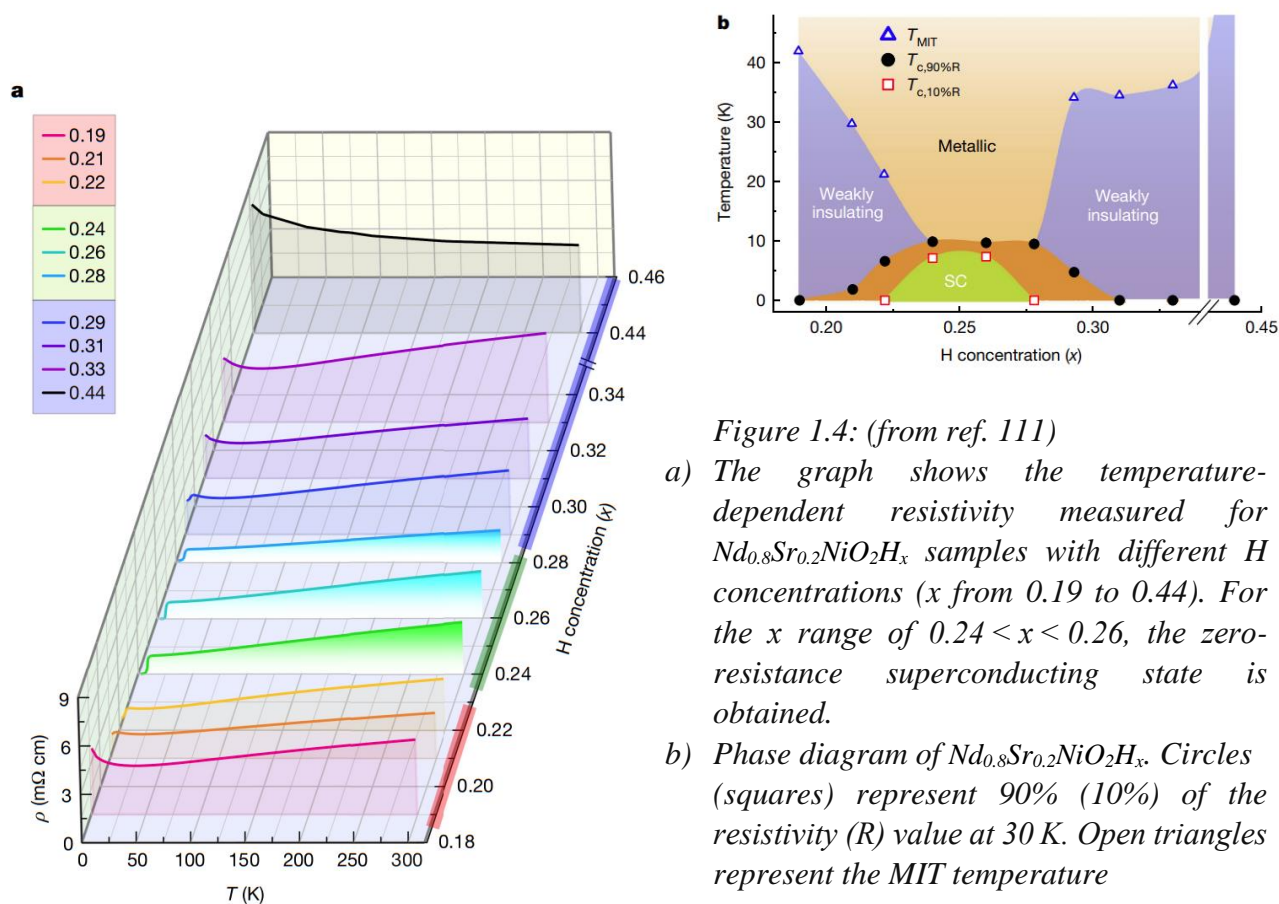


Figure 1.4: (from ref. 111)

- a) The graph shows the temperature-dependent resistivity measured for  $\text{Nd}_{0.8}\text{Sr}_{0.2}\text{NiO}_2\text{H}_x$  samples with different H concentrations ( $x$  from 0.19 to 0.44). For the  $x$  range of  $0.24 < x < 0.26$ , the zero-resistance superconducting state is obtained.
- b) Phase diagram of  $\text{Nd}_{0.8}\text{Sr}_{0.2}\text{NiO}_2\text{H}_x$ . Circles (squares) represent 90% (10%) of the resistivity ( $R$ ) value at 30 K. Open triangles represent the MIT temperature

their location or valence state ( $H^+$  or  $H^-$ ). The study found that hydrogen enhances the electron correlation by reducing the bandwidth of Ni 3d orbitals, making them more localized and less hybridized with O 2p orbitals. Hydrogen also induces a charge transfer by donating electrons to O 2p orbitals, creating holes in Ni 3d orbitals. These effects make nickelates more similar to cuprates, which have a two-orbital Mott insulator as their parent compound. The study also investigated the temperature-dependent resistivity and Hall coefficient of  $Nd_{0.8}Sr_{0.2}NiO_2H_x$  samples with varying concentrations of hydrogen (H). The results showed that for low and high H concentrations, the samples exhibited weakly insulating behavior with an upturn in resistivity at around 30 K. For intermediate H concentrations, a superconducting-like resistivity transition was observed, but zero resistance could not be achieved. However, for the H concentration range of  $0.24 < x < 0.26$ , the samples exhibited a zero-resistance superconducting state. The phase diagram showed that the critical H concentration for the transition from a superconducting-like state to a weakly insulating state was around  $x = 0.26$ . The temperature dependence of the Hall coefficient showed a metallic behavior, with a maximum value at around  $x = 0.24$ . As the H concentration increased beyond this point, the metallic behavior decreased. In summary, this particular study implicates the essential role of hydrogen in achieving superconductivity in nickelates by tuning their electronic structure and creating favorable conditions for pairing mechanisms.

### *1.5.5 Nickelate superconductivity: current challenges*

Experimental progress is limited, and this leads to theoretical research that is diverse and inconsistent. Some theories may not fit or may even oppose later experimental findings. In contrast, most of the experiments that have been done are in line with each other until now [88], [112], [113].

Reproducibility and synthesis challenges in infinite-layer nickelates are major obstacles to the development and understanding of these materials. One of the main challenges in the synthesis of infinite-layer nickelates is to stabilize the doped perovskite phase  $RNiO_3$ , which is the precursor for the topotactic reduction to  $RNiO_2$ . This requires precise control of the growth parameters, such as temperature, pressure, oxygen partial pressure, and laser fluence. However, even with optimal conditions, the perovskite phase can be easily contaminated by secondary phases, such as

Ruddlesden-Popper phases  $R_2NiO_4$  or pyrochlore phases  $R_2Ti_2O_7$ , which can degrade the quality and superconductivity of the final product [51]. Another challenge is to balance between complete topotactic reduction and subsequent decomposition of  $RNiO_2$ , which requires careful control of the annealing parameters, such as temperature, time, and hydrogen partial pressure. The reduction process can be incomplete or irreversible, leading to oxygen vacancies or excess hydrogen intercalation in  $RNiO_2$ , which can alter the electronic structure and properties of the material. The oxygen content plays a crucial role in determining the doping level, lattice parameters, electronic structure, and superconducting properties of infinite-layer nickelates [114].

In addition, achieving a high-quality interface between the infinite layer nickelate film and the substrate is a challenging task that has a strong influence on superconductivity. The interface may introduce a polar discontinuity, strain effects, charge transfer, intermixing, and disorder, all of which can modify the electronic and magnetic properties of the film [115], [116]. Recent research by Goodge et al. revealed that the interface between  $Nd_{0.8}Sr_{0.2}NiO_2$  and  $SrTiO_3$  is characterized by a single intermediate layer of  $Nd(Ti,Ni)O_3$ , which alleviates the polar discontinuity but also introduces a potential barrier for charge transport [116].

The reproducibility of infinite-layer nickelate superconductivity poses a further challenge due to the material sensitivity to various factors. Different research groups have reported different values of the superconducting transition temperature ( $T_c$ ), ranging from 9 K to 25 K, depending on factors such as rare earth elements, doping level, film thickness, substrate choice, measurement technique, and sample preparation. Additionally, some groups have encountered difficulties in reproducing superconductivity in their samples or observing it only in a fraction of their samples. The origin of these discrepancies is not fully understood and may be related to subtle variations in oxygen stoichiometry, interface quality, strain effects, or sample degradation [112], [113], [117], [118]. Furthermore, a group demonstrated that  $Nd_{0.8}Sr_{0.2}NiO_2$  superconducting state is highly stable and can persist for at least 47 days under continuous exposure to air at 20°C and 35% relative humidity. Additionally, they found that immersing the material in de-ionized water at room temperature for 5 hours led to the disappearance of superconductivity. Still, the material was observed to retain its superconducting properties under ionic liquid gating conditions with an applied voltage of approximately 4V, which proved to be even more stable than conventional perovskite complex oxides [119].

The realization of superconductivity in bulk nickelates is hampered by the material's thermodynamic instability and sensitivity. Unlike thin films, bulk nickelates necessitate high temperatures and pressures to synthesize and stabilize the infinite layer phase, which is prone to oxidation and decomposition. In addition to the difficulties faced in thin film nickelate synthesis, bulk synthesis can also introduce defects, impurities, disorder, and phase separation, which can potentially suppress or destroy superconductivity [71], [88], [113], [120]. Another challenge is to minimize the formation of nickel clusters and nickel deficient regions in bulk nickelates, as these can interfere with superconductivity. A study suggested that the non-uniform distribution of oxygen atoms in bulk nickelates can result in local variations in the valence and magnetic state of nickel atoms, leading to the formation of these regions. These regions can act as magnetic impurities or potential barriers that can disrupt superconducting pairing or transport [121].

Besides these synthesis challenges, there are also many open questions and perspectives in nickelate superconductivity research, such as:

- (i) Understanding the role of hydrogen and its effect on the electronic structure and superconducting properties of nickelates.
- (ii) Developing more reliable reduction techniques.
- (iii) Developing new synthesis methods to produce bulk or single-crystal samples of nickelates and exploring other possible doping elements and rare-earth substitutions.
- (iv) Investigating the phase diagram, magnetic correlations, charge density waves, and pairing mechanism of nickelates using various experimental and theoretical techniques.
- (v) Comparing and contrasting nickelates with cuprates and other unconventional superconductors to reveal the common and distinct features of high-temperature superconductivity.

## 1.6 $K_2NiF_4$ -type rare earth nickelates

The homologous RP-type nickelate series includes  $Ln_2NiO_{4+\delta}$  and related compounds, which are  $n=1$  members of the series, also referred to as  $K_2NiF_4$ -type phases. The A-site Ln cations are positioned at the boundary of two layers and are coordinated by nine oxygen ions in

stoichiometric  $\text{Ln}_2\text{NiO}_4$  compounds. Conversely, the B-site Ni cations are found in the center of octahedra created by six oxygen anions. The  $\text{NiO}_6$  octahedra share corners in the a-b plane, which forms a 2D network.  $\text{Ln}_2\text{NiO}_{4+\delta}$  has a distorted tetragonal symmetry ( $P4_2/nm$ ) or orthorhombic symmetry ( $Fmmm$ ) depending on the lanthanide elements, the oxygen stoichiometry  $\delta$ , and temperature [122]–[129]. Over the past few years, there has been a growing interest in studying a particular type of nickelates that has a tetragonal structure with  $\text{K}_2\text{NiF}_4$ -type. In the case of  $\text{Nd}_2\text{NiO}_4$ , researchers have found that replacing neodymium with strontium significantly affects their crystal and electronic structure. To investigate this further, scientists have used various methods to create samples with different levels of strontium doping, ranging from  $x=1.0$  to 1.6, and have studied their properties using techniques like X-ray diffraction and electrical conductivity measurements [125], [130]–[137].

Their findings suggest that the strontium doping compensates for acceptor-type substitution by electron-holes and oxygen vacancies, with the latter becoming more prominent at higher temperatures. In addition, the level of strontium content influences the oxygen nonstoichiometry, resulting in anisotropy of tetragonal lattice expansion and anomalous dilatometric behavior. Interestingly, the highest conductivity was observed at  $x=1.2$ , indicating that these materials exhibit mixed conductivity, with a non-negligible contribution of ionic transport to the total conductivity. Further research has also revealed that exposing these materials to an inert gas atmosphere leads to the ordering of oxygen vacancies, causing a reduction of the lattice symmetry to orthorhombic [131]. In terms of the impact of strontium on the  $\text{Nd}_2\text{NiO}_4$  structure, the incorporation of  $\text{Sr}^{2+}$  ions into the Nd sites can help reduce the stress in the bonds between the Nd ions and oxygen atoms. This is because the ionic radius of  $\text{Sr}^{2+}$  is slightly larger than that of  $\text{Nd}^{3+}$ . By taking up space in the rare-earth sublattice of  $\text{Nd}_{2-x}\text{Sr}_x\text{NiO}_{4+d}$ , the Sr ions can effectively release tension in the Nd-O bonds. As a result, the Ln and O ions can be in a more relaxed state, reducing the stress in the bonds between them [138].

The field of nickelates has established a robust foundation in the realm of condensed matter physics, predating the recent discovery of superconductivity in 2019. As the synthesis and growth of nickel oxides with extreme oxidation states continue to improve, there is a heightened potential for unveiling novel insights into previously unanswered questions. The near future holds great

promise for the study of both superconducting and non-superconducting nickelate systems, as unexpected surprises are likely to arise from these investigations.



**Investigation of the physical,  
chemical, and structural properties  
of polycrystalline  $\text{Nd}_{0.8}\text{Sr}_{1.2}\text{NiO}_4$  and  
topotactically reduced  $\text{Nd}_{0.8}\text{Sr}_{1.2}\text{NiO}_3$**

## 2.1 Introduction

The recipe for achieving superconductivity in nickelates is still under investigation. Furthermore, it has been firmly established that the valence of nickel is a critical parameter in the quest for a nickelate superconductor. Attaining a valence of +1.2 for nickel, which could electrically resemble Cu in HTS cuprates, is both challenging and considered essential for this endeavor. The challenges stem from the fact that nickel is a transition metal with multiple valence states, and its valence can be affected by various factors, such as oxygen stoichiometry, crystal structure, and doping level. The manipulation of the valence of nickel in nickelates requires precise control over the synthesis conditions, such as the temperature, pressure, atmosphere, and chemical composition. To this end, layered nickelates are particularly attractive as they offer the possibility of topotactic reduction, whereby the layered structure is retained even after the removal of oxygen.

Ruddlesden-Popper (RP)  $\text{Nd}_{0.8}\text{Sr}_{1.2}\text{NiO}_4$  is a highly promising material for studying the effects of  $\text{CaH}_2$  reduction on bulk nickelates. This material is of particular interest because its nickel valency ( $\text{Ni}^{3.2+}$ ) closely resembles that of the parent perovskite phase of superconducting infinite-layer nickelates. Most importantly,  $\text{Nd}_{0.8}\text{Sr}_{1.2}\text{NiO}_4$  is more stable and easier to synthesize in comparison with the perovskite analog. The ability to tune the nickel valency in RP  $\text{Nd}_{0.8}\text{Sr}_{1.2}\text{NiO}_4$  through the use of  $\text{CaH}_2$  reduction allows for the systematic exploration of the electronic properties of bulk nickelates and study impacts of  $\text{CaH}_2$  reduction in structural and physical properties of nickelates. A thorough investigation of the electronic and magnetic properties of RP  $\text{Nd}_{0.8}\text{Sr}_{1.2}\text{NiO}_4$ , and topotactically reduced phase could help in the comprehension of the underlying mechanisms of superconductivity in infinite-layer nickelates. This can be accomplished by analyzing the changes in electronic and magnetic properties that occur as a result of reduction and by studying the relationship between these properties and the valency of nickel. Such a study could also reveal key factors that contribute to the high-temperature superconductivity observed in nickelates.

## 2.2 Synthesis of polycrystalline $\text{Nd}_{0.8}\text{Sr}_{1.2}\text{NiO}_4$ and $\text{Nd}_{0.8}\text{Sr}_{1.2}\text{NiO}_3$

The solid-state reaction method is a widely used technique for synthesizing complex oxide materials that does not require any solvents. It involves heating and mixing the desired metal oxides or salts in a solid form until a chemical reaction occurs and forms a new phase. This method is simple, cost-effective, and convenient compared to other methods such as sol-gel, hydrothermal, and vapor deposition methods. It is particularly useful for synthesizing bulk nickelates. However, the ease of synthesizing bulk nickelates through the solid-state reaction method primarily relies on the nickel valency of the intended product, which stems from variations in the thermodynamic stability of distinct nickel cations under ambient conditions. In general, this instability demands high-pressure and high-temperature conditions to stabilize the nickelate phase, which can be expensive and not easily accessible for most laboratories. As a result, several approaches and strategies have been proposed to synthesize bulk nickelates using the solid-state reaction method at near-ambient or low pressures.

One such approach is the mixing-grinding-annealing technique. This technique involves mixing metal oxides or salts in a solid form and grinding them together until a fine powder is obtained. The powder is then heated at high temperatures in an oxygen atmosphere to induce a chemical reaction and form the nickelate phase. Although this technique is simple, cheap, and convenient, it may result in particle aggregation, incomplete reaction, and poor homogeneity of the product. The particle size, morphology, and properties of the nickelate materials depend on the choice of precursors, grinding time, annealing temperature, and duration.

The synthesis of  $\text{Nd}_{0.8}\text{Sr}_{1.2}\text{NiO}_4$  involves a multi-step solid-state reaction method. In this method,  $\text{Nd}_2\text{O}_3$ ,  $\text{SrCO}_3$ , and  $\text{NiO}$  are used as precursors. At first, stoichiometric amounts of these precursors are well-ground and mixed to form a light green powder. This powder is then heated at  $1000^\circ\text{C}$  for 24 hours to allow for the evolution of  $\text{CO}_2$ , resulting in a black fine powder. This process is repeated with intermediate grinding and for removing remaining  $\text{CO}_2$ . The resulting powder is then ground and heated in an oxygen flow at  $1250^\circ\text{C}$  for 24 hours. This product is then shaped into bars through pressing and sintering at  $1200^\circ\text{C}$ .

To obtain the reduced phase,  $\text{Nd}_{0.8}\text{Sr}_{1.2}\text{NiO}_3$ , the topotactic reduction method is employed. In this method,  $\text{Nd}_{0.8}\text{Sr}_{1.2}\text{NiO}_4$  bars were subjected to reduction with  $\text{CaH}_2$  powder in a vacuum-sealed quartz tube with an inner and outer diameter of 9mm and 15mm, respectively, and an approximate length of 15cm. The transfer of both the  $\text{Nd}_{0.8}\text{Sr}_{1.2}\text{NiO}_4$  bars of  $\text{CaH}_2$  powder to the tube was performed in a glove box, which provided an inert atmosphere. To prevent direct contact of  $\text{CaH}_2$  powder with the sample, the  $\text{Nd}_{0.8}\text{Sr}_{1.2}\text{NiO}_4$  bars of mass 0.15g were loosely wrapped in aluminum foil, and approximately 0.1-0.2g of  $\text{CaH}_2$  powder was weighed in the glove box prior to transfer. The tube was then vacuum-sealed to an approximate pressure of 0.001mbar, and heated to a temperature range of 280°C-300°C for a duration of 10-20 hours.

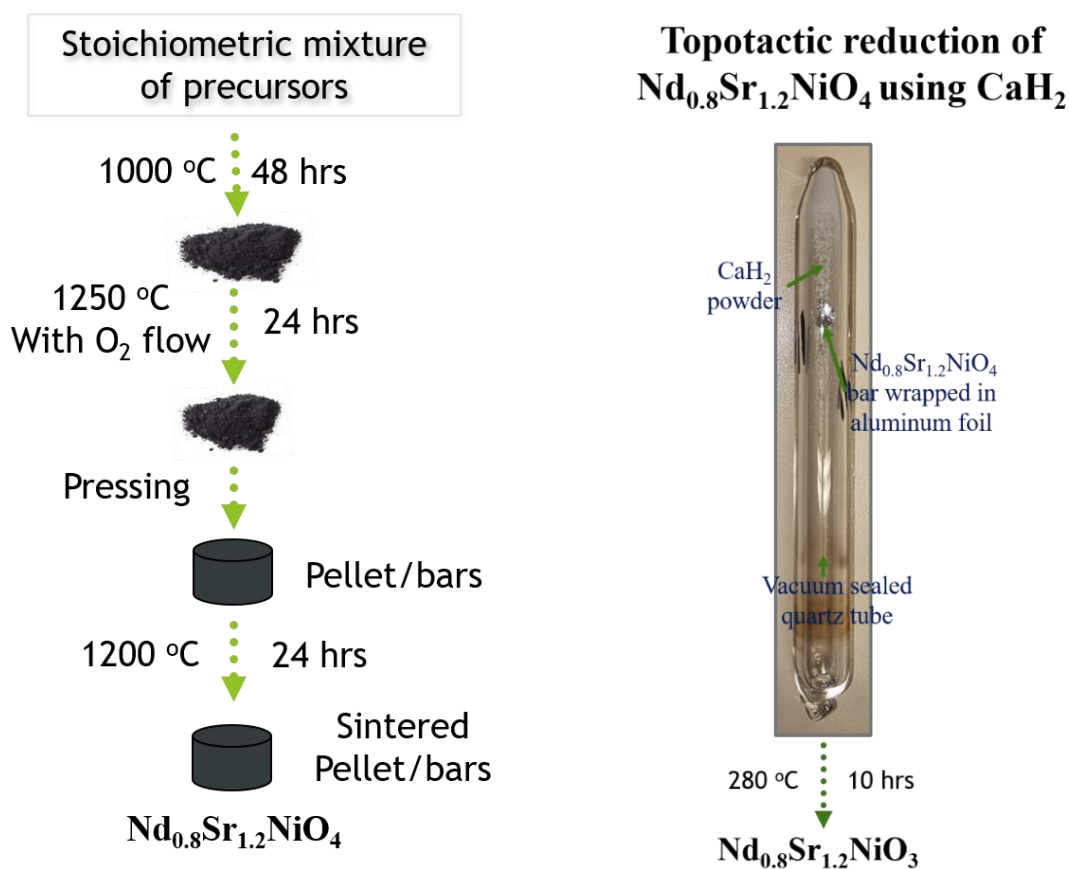


Figure 2.1

Schematic diagram shows

(a) Solid state synthesis steps for  $\text{Nd}_{0.8}\text{Sr}_{1.2}\text{NiO}_4$

(b) Topotactic reduction using  $\text{CaH}_2$  of  $\text{Nd}_{0.8}\text{Sr}_{1.2}\text{NiO}_4$

## 2.3 Structural characterizations

### 2.3.1 $\text{Nd}_{0.8}\text{Sr}_{1.2}\text{NiO}_4$

The sample  $\text{Nd}_{0.8}\text{Sr}_{1.2}\text{NiO}_4$  was subjected to X-Ray diffraction analysis to verify its phase purity and establish its structural relationship with the perovskite framework. The entire diffraction pattern, highlighted by the initial peak at  $d = 6.125 \text{ \AA}$ ,  $2\theta = 11^\circ$  (Figure 2.2), can be fully indexed in a tetragonal cell with the following parameters:  $a = a_p = 3.8030(7) \text{ \AA}$  and  $c = 12.259(3) \text{ \AA}$ , with the space group  $I4/mmm$ . This space group is consistent with the Ruddlesden-Popper ( $n=1$ ) phase [139]. The subsequent structure analysis was conducted within this space group, considering the anticipated Ruddlesden popper ( $n=1$ ) or  $\text{RP1-A}_2\text{BO}_4$  structure. This analysis revealed that Neodymium and Strontium atoms randomly occupy the same crystallographic site. All attempts to introduce order among these atoms yielded unsatisfactory results.

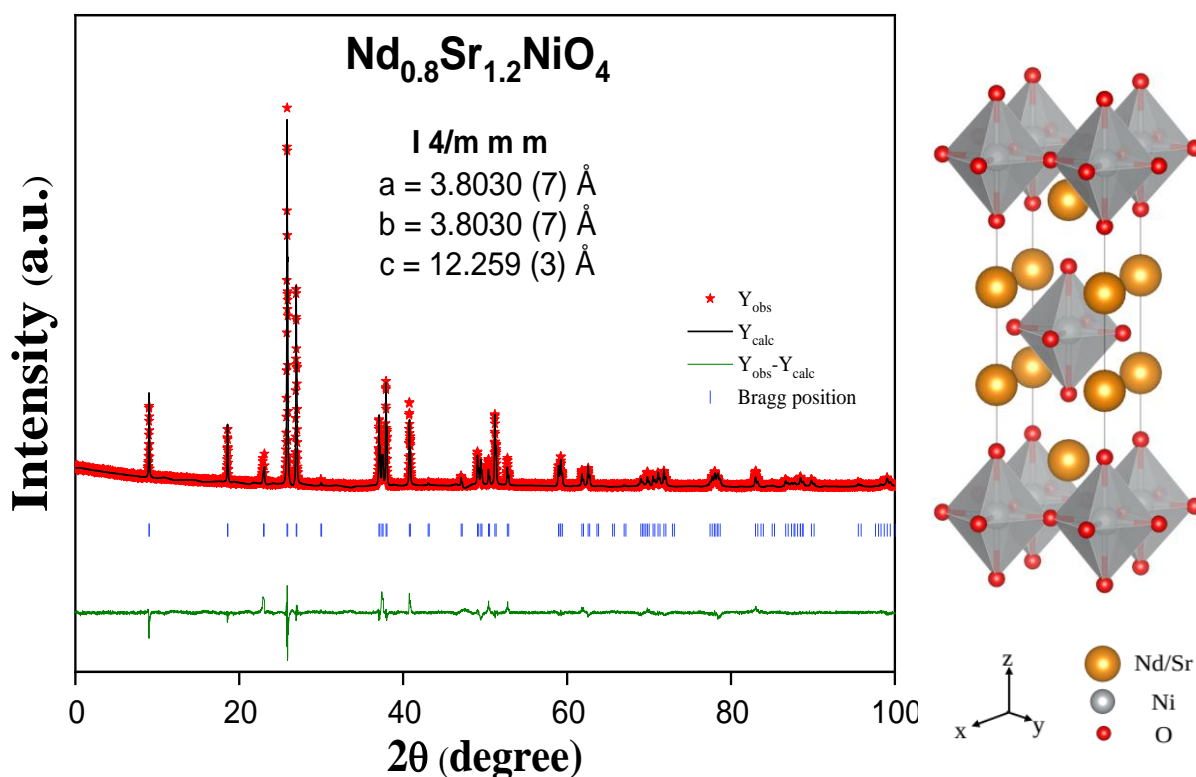


Figure 2.2

*XRD pattern and Rietveld refinement of the monochromated XRPD data recorded at RT for  $\text{Nd}_{0.8}\text{Sr}_{1.2}\text{NiO}_4$ . Corresponding crystal structure is shown (generated using Vesta)*

The final refinements, which included anisotropic thermal displacement parameters for oxygen, yielded the following values:  $R_B = 0.163$ ,  $R_p = 0.066$ ,  $R_{wp} = 0.086$ ,  $\chi^2 = 1.54$ , for the structural parameters listed in Table 2.1. The comparison with the difference diffraction pattern (Figure 2.2) confirms the excellent fit.

Table 2.1: Atomic positions, occupancies, isotropic atomic displacements for  $\text{Nd}_{0.8}\text{Sr}_{1.2}\text{NiO}_4$  from x-ray diffraction:

Atom	x	y	z	Occ	B iso
Nd/Sr	0	0	0.3623	0.125	0.6924
Ni	0	0	0	0.0625	0.3378
O1	0	0.5	0	0.125	0.8876
O2	0	0	0.15496	0.125	0.9535

Considering the precision of the technique in determining oxygen atom positions, the  $\text{NiO}_6$  octahedron displays regularity with a calculated distance of 1.90 Å. This value is in strong agreement with the distance reported by Takeda et al. in the compound  $\text{Nd}_{0.8}\text{Sr}_{1.2}\text{NiO}_4$ , showing a mixed nickel valency of  $\text{Ni}^{3+}$  and  $\text{Ni}^{4+}$  [140].

Table 2.2: Ionic radius of Ni ions for reference[141] [142]

Ion	Coordination	Geometry	Spin state	Ionic radius (pm)
$\text{Ni}^{2+}$	4	tetrahedral	high-spin	69
$\text{Ni}^{2+}$	6	octahedral	high-spin	78
$\text{Ni}^{2+}$	6	octahedral	low-spin	65
$\text{Ni}^{2+}$	4	square planar	low-spin	49
$\text{Ni}^{3+}$	6	octahedral	low-spin	56
$\text{Ni}^{3+}$	6	octahedral	high-spin	60
$\text{Ni}^{4+}$	6	octahedral	low-spin	48

### 2.3.2 Nd<sub>0.8</sub>Sr<sub>1.2</sub>NiO<sub>3</sub>

The reduced sample Nd<sub>0.8</sub>Sr<sub>1.2</sub>NiO<sub>3</sub> was characterized by means of different complementary technics: 3D Electron diffraction (3D-ED, X-ray diffraction and high-resolution image analysis. Because of the weakness of X-ray regarding the oxygen atoms localization, we performed a 3D-ED analysis at room temperature. The conditions of data acquisition are summarized in the table below (Table 2.3), and structure solutions from the analyzed data are summarized in Table 2.4.

Table 2.3: Details of 3D-ED data acquisition for Nd<sub>0.8</sub>Sr<sub>1.2</sub>NiO<sub>3</sub>

Jeol F200 TEM (200 kV)
The sample was crushed in an agate mortar and deposited on a Cu grid with holey C film
Temperature 293 K
PEDT (Precession Electron-assisted Electron Diffraction Tomography) was performed on single crystals
Precession semi angle $\varphi = 1.4^\circ$
Hybrid pixel detector ASI Cheetah
Exposure time 0.5 s per frame
Tilt range $\alpha = -35/+61^\circ$ , Tilt step $1^\circ$ , total number of used frames 88

Table 2.4: Structure solutions for Nd<sub>0.8</sub>Sr<sub>1.2</sub>NiO<sub>3</sub>

Unit cell: $a = 3.838(3) \text{ \AA}$ , $b = 3.643(3) \text{ \AA}$ and $c = 12.573(9)$ , $90^\circ 90^\circ 90^\circ$ , volume 175.8 (computed and refined with <i>Pets2.0</i> )
Crystal system: oI (orthorhombic body centered), Space group: Immm (SG:71)
Structure solution (using Charge Flipping) and refinement computed on <i>Jana2020</i> .
Resolution $\sin(\theta_{\max})/\lambda$ ( $\text{\AA}^{-1}$ ): 0.85
Cumulative coverage: 87.1%

In the initial phase, a meticulous investigation was undertaken to ascertain the space group of the compound. This process involved a comprehensive consideration of both X-ray and electron diffraction pattern information. The reduced compound no longer crystallizes in a tetragonal symmetry; instead, it adopts an orthorhombic configuration, indicating a reduction in symmetry. The *Immm* space group enables the indexing of all reflections and yields the most accurate fitting values with the cell parameters  $a = 3.838(3) \text{ \AA}$ ,  $b = 3.643(3) \text{ \AA}$  and  $c = 12.573(9) \text{ \AA}$  (Le Bail fit x-ray  $\chi^2 = 3.2$ )

Table 2.5: 3D-ED data refinements for  $\text{Nd}_{0.8}\text{Sr}_{1.2}\text{NiO}_3$ 

	Kinematical refinement: file ESR12	Dynamical refinement: ESR12
Measured, observed [ $I > 3\sigma(I)$ ] reflections	313, 313	2015, 1833
No. of refined parameters, restraints	8, 0	106, 0
$R(\text{obs})$ , $R(\text{all})$ , $wR(\text{all})$ , GoF(all)	0.159, 0.164, 0.336, 7.32	0.283, 0.283, 0.592, 27.57
$g_{\text{max}} (\text{\AA}^{-1})$ , $S_{g,\text{max}} (\text{\AA}^{-1})$ , $R_{\text{Sg}}$ , steps		2, 0.01, 0.4, 96

It can be observed that the parameter  $b$  of the cell has significantly decreased (compare to the one of the oxidized compounds), while the parameters  $a$  and  $c$  of the cell have slightly increased. Based on this observation, we infer that the oxygen vacancies are likely to be situated along the  $b$  direction. As a result, the dynamical structure refinement was conducted considering that point. It leads to the results listed in table below.

Table 2.5: 3D-ED data refinements for  $\text{Nd}_{0.8}\text{Sr}_{1.2}\text{NiO}_3$ 

Atom	x	y	z	Occ	ADP
Nd/Sr	0.5	0	0.142217	0.25	0.009243
Ni	0	0.5	0	0.125	0.001752
O1	-0.5	0.5	0	0.125	0.011004
O2	0	0.5	-0.166424	0.25	0.011716

A meticulous examination of the stacking arrangement was conducted, taking into account the substantial presence of oxygen vacancies that could potentially introduce local disorder. As depicted in Figure 2.4, a high-resolution image of the basal plane [100] reveals that the stacking pattern remains remarkably consistent and orderly. Several crystals were examined, and no evidence of disorder was detected.

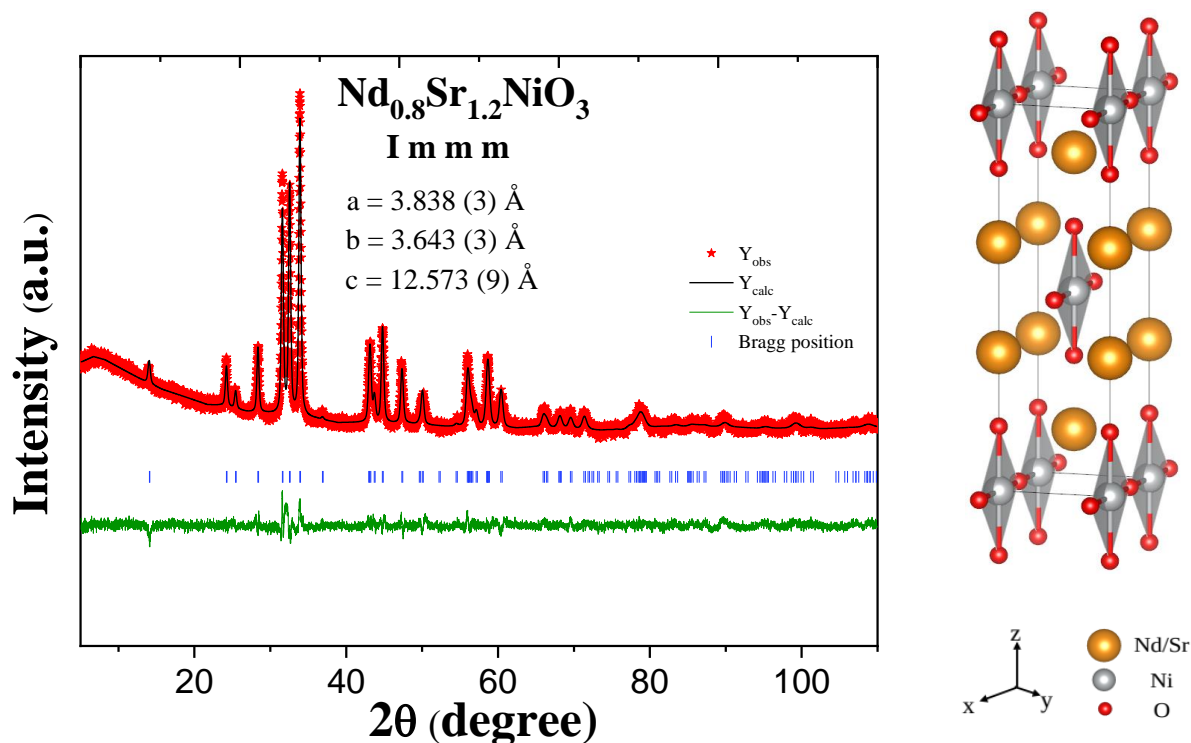


Figure 2.3: XRD pattern and Rietveld refinement of the monochromated XRPD data recorded at RT for Nd<sub>0.8</sub>Sr<sub>1.2</sub>NiO<sub>3</sub>. Corresponding crystal structure is shown (generated using Vesta)

In conclusion, the intergrowth remains unchanged throughout the reduction process, with the oxygen vacancies being distributed along a specific direction that involves a square arrangement of nickel atoms (refer to Figure 2.3). These nickel square planes are corners shared in only one direction (a). The Ni-O distance is 1.98 Å, while it was 1.9 Å in the fully oxidized

compound. This is in agreement with the increase of the ionic radius of Ni implied by the decrease of the oxidation state.

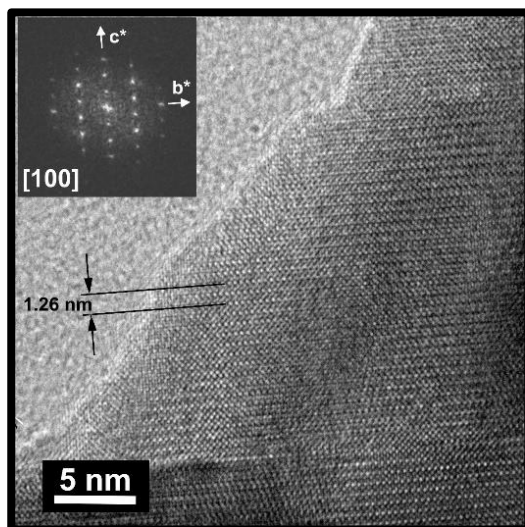


Figure 2.4 : TEM image of  $\text{Nd}_{0.8}\text{Sr}_{1.2}\text{NiO}_3$ . Inset shows FFT of crystallite along (100) direction

## 2.4 Physical characterizations of $\text{Nd}_{0.8}\text{Sr}_{1.2}\text{NiO}_4$

### 2.4.1 Electrical resistivity measurement

After structural characterization, samples are prepared for resistivity measurement. We employed four-probe resistivity measurement and the measurements are carried out using Quantum Design's Physical Property Measurement System (PPMS). The four-probe resistivity measurement method uses four probes to measure the voltage drop across a sample. Four electrodes are attached to the sample in a linear configuration. Voltage is measured using two inner probes while a constant current is passed through the outer electrodes. Using four electrodes instead of two has the advantage of removing the contact resistance that occurs between the electrodes and the sample.

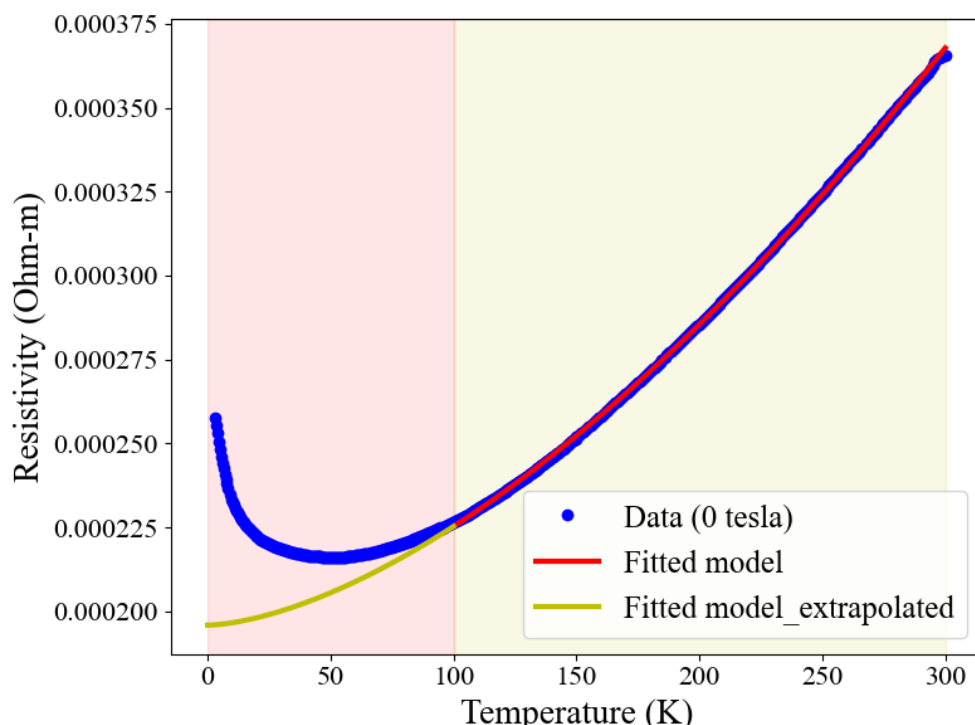


Figure 2.5: Electrical resistivity vs Temperature plot of  $\text{Nd}_{0.8}\text{Sr}_{1.2}\text{NiO}_4$  fitted with eq 2.1

This is particularly important as the contact resistance can be considerable when compared to the resistance of the sample, resulting in measurement errors. The sample used for the measurement is in the shape of a bar with known dimensions and weight. Lead contacts are made on the sample in a linear pattern, and the resistance is measured using PPMS by applying a constant current of 5000

$\mu\text{A}$  over the temperature range of 3-300K. Resistivity is calculated by normalizing the resistance data with dimensions of the sample.

Resistivity shows metallic behavior with resistive upturn observed from temperature below 50K as shown in figure 2.5. In the study of metallic materials, the temperature dependence of their electrical resistivity is often described using a power law model. It is a phenomenological and empirical approximation that works well for some metals in certain temperature ranges. Resistivity, according to power law ( $\rho_{PL}$ ), of a metal is proportional to the  $n^{\text{th}}$  power of the temperature, T, i.e.,

$$\rho_{PL} = \rho_0 + AT^n \quad 2.1$$

where  $\rho_0$  is residual resistivity and A is a coefficient related to the strength of electron scattering, and n is the power law exponent. The value of n depends on the type of metal and the temperature range being considered. Power law is a good choice since nickelates are often considered to deviate from fermi liquid behavior with  $n < 2$  and identified as non-fermi liquid (NFL) [143]–[148]. As shown in figure 2.5, equation 2.1 fits best with temperature range 100-300 K with a value of  $n = 1.5$ . Fit model is extrapolated to 0 Kelvin to indicate the deviation from the model at low temperature where resistive upturn is observed (figure 2.5).

To have an insight into the transport properties of  $\text{Nd}_{0.8}\text{Sr}_{1.2}\text{NiO}_4$ , we relied on the DFT calculations conducted by Alvaro Adrian Carrasco Alvarez (CRISMAT Lab). These calculations reveal that the physics at the Fermi level is strongly influenced by both O 2p and Ni 3d states, resulting in a highly hybridized structure, as depicted in Figure 2.6b. A more extensive analysis by contrasting the projected density of states of  $\text{La}_2\text{NiO}_4$  (undoped) and  $\text{La}_{0.8}\text{Sr}_{1.2}\text{NiO}_4$  (doped), as depicted in Figures 2.6 a and 2.6 b shows that introducing Sr made  $\text{La}_2\text{NiO}_4$  having an insulating ground state to metallic. Figure 2.7 shows projected density of states for  $\text{Nd}_{0.8}\text{Sr}_{1.2}\text{NiO}_4$  obtained using a hybrid DFT functional. This figure clearly demonstrates a resemblance between the electronic structures of  $\text{Nd}_{0.8}\text{Sr}_{1.2}\text{NiO}_4$  and the meticulously computed  $\text{La}_{0.8}\text{Sr}_{1.2}\text{NiO}_4$  (as shown in figure 2.6b). Notably, this similarity underlines the contribution of Ni-d and O-p states to conduction, with a significant degree of hybridization. These findings lend further support to the analogy they have drawn between the La and Nd compounds. Therefore, the electronic structure

insights collected from  $\text{La}_{0.8}\text{Sr}_{1.2}\text{NiO}_4$  can indeed be extrapolated to provide relevant information for  $\text{Nd}_{0.8}\text{Sr}_{1.2}\text{NiO}_4$  as well.

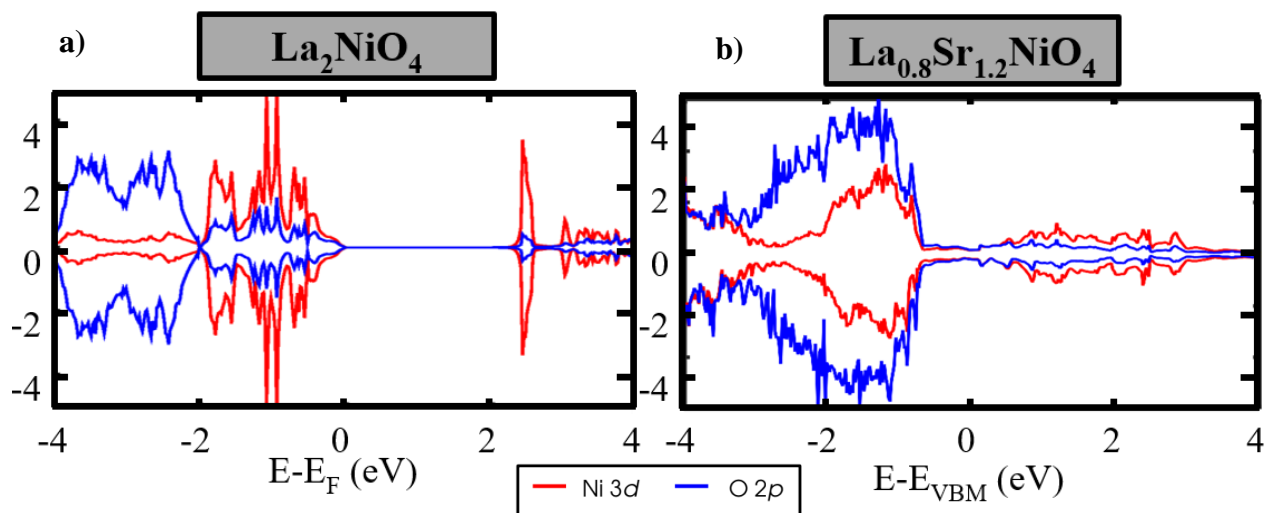


Figure 2.6: Projected density of states (a)  $\text{La}_{0.8}\text{Sr}_{1.2}\text{NiO}_4$ . (b)  $\text{La}_2\text{NiO}_4$ . Red lines on the DOS are Ni  $d$  states and in blue O  $p$  states. Positive and negative DOS corresponds to spin-up and spin-down channels.

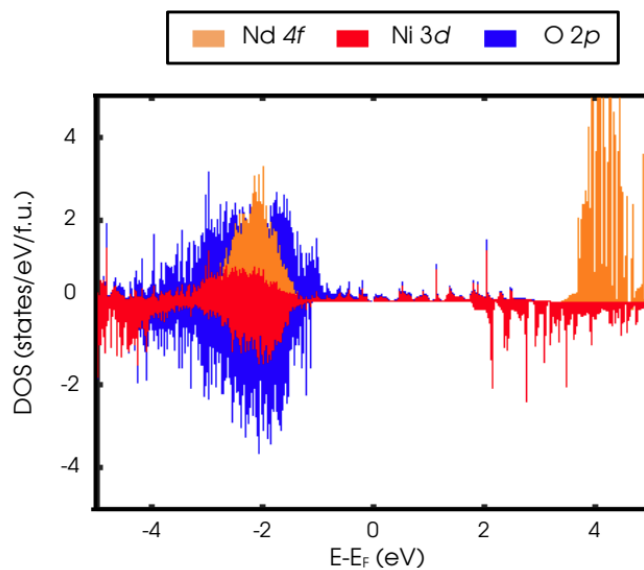


Figure 2.7: Projected density of states for  $\text{Nd}_{0.8}\text{Sr}_{1.2}\text{NiO}_4$ . The negative and positive density of states corresponds to the spin-up and spin-down channels, respectively. Nd  $4f$  states are represented in orange, O  $2p$  states in blue, and Ni  $3d$  states in red.

Furthermore, the doped RP  $n = 1$  compound tends to fall within the CT (charge transfer) regime as evident from the significant overlap between the O 2p and Ni 3d near Fermi energy as shown in figure 2.6b and that an electron can be easily transferred between them. From the observation that ground state electronic band structure of  $\text{La}_{0.8}\text{Sr}_{1.2}\text{NiO}_4$  (or  $\text{Nd}_{0.8}\text{Sr}_{1.2}\text{NiO}_4$ ) in Figures 2.6b and 2.7 is metallic. Hence, the slight increase in resistivity at lower temperatures does not appear to indicate a classic metal-insulator transition. This implies the need for an alternative explanation to account for experimentally observed low temperature resistive upturn.

In order to explain the underlying mechanism of the resistivity upturns observed at low temperatures, we investigated the potential influence of Kondo-like impurity scattering. The Kondo effect is a many-body phenomenon that arises due to the interaction between conduction electrons and a localized magnetic impurity, such as a transition metal or rare earth ion, in a metallic host. At low temperatures, the impurity spin becomes correlated with the conduction electrons, leading to a screening of the impurity and a reduction in its magnetic moment. This screening effect gives rise to the logarithmic temperature dependence in resistivity, which is commonly observed in Kondo systems, calculated using a third-order perturbation expansion of the s-d exchange scattering of conduction electrons from localized spins [149]. The presence of magnetic  $\text{Nd}^{3+}$  ions in the system, with well-localized 4f states 2eV below the Fermi level as shown in figure 2.8. which supports the Kondo scenario from the electronic structure point of view (Since these magnetic  $\text{Nd}^{3+}$  could act as scattering centers for conduction electrons). To test this hypothesis, we incorporated a logarithmic term in temperature into the resistivity equation and evaluated its goodness of fit to the experimental data.

By adding the logarithmic term equation for resistivity expressed in simplest form as

$$\rho(T) = \rho_0 + AT^n + \rho_k \log\left(\frac{T}{T_k}\right) \quad 2.2$$

$\rho_k$  is a constant which is proportional to s-d exchange integral  $J$  and  $T_k$  is Kondo temperature.

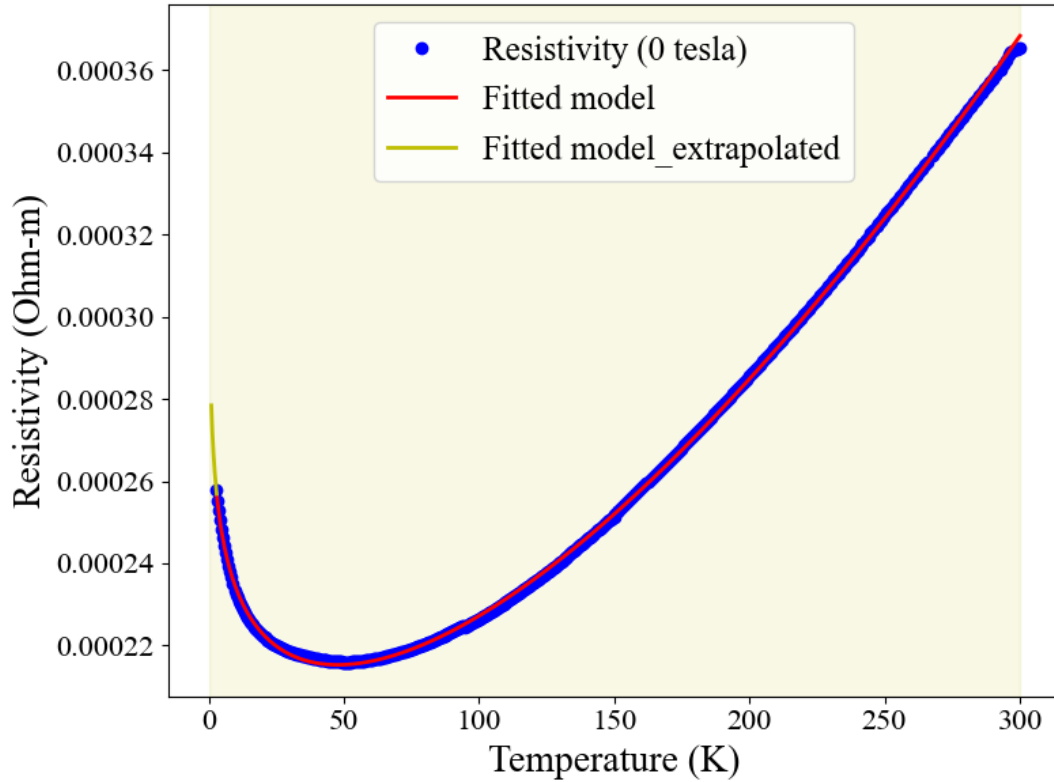


Figure 2.8: Electrical resistivity vs Temperature plot fitted with additional term accounting Kondo effect (eq 2.2)

The fit results suggest that the resistivity model used provides a good fit to the data, as indicated by the very small chi-square value ( $1.9084 \times 10^{-11}$ ), which is a measure of the discrepancy between the observed and expected frequencies of the data, based on the model and the high value of R-squared (close to 1), which is a measure of the proportion of the variance in the data that is explained by the model.

Table 2.7 : Parameters obtained from a fit to the resistivity data using equation 2.2 in the temperature range 3 to 300K

Parameter	Value
$\rho_0$	2.19e-04 ( $\Omega$ -m)
$A$	4.36e-08 ( $m \Omega \text{ cm/K}^n$ )
$n$	1.48
$\rho_k$	-1.97e-05 ( $\Omega$ -m)
$T_k$	19.95 K

$n$  value of 1.48 suggest the non-fermi liquid nature of resistivity and the Kondo crossover temperature,  $T_k$  of 19.95 K marks the transition from a high-temperature regime where the magnetic impurities in a metal behave as independent local spins, to a low-temperature regime where they form a coherent state with the conduction electrons.

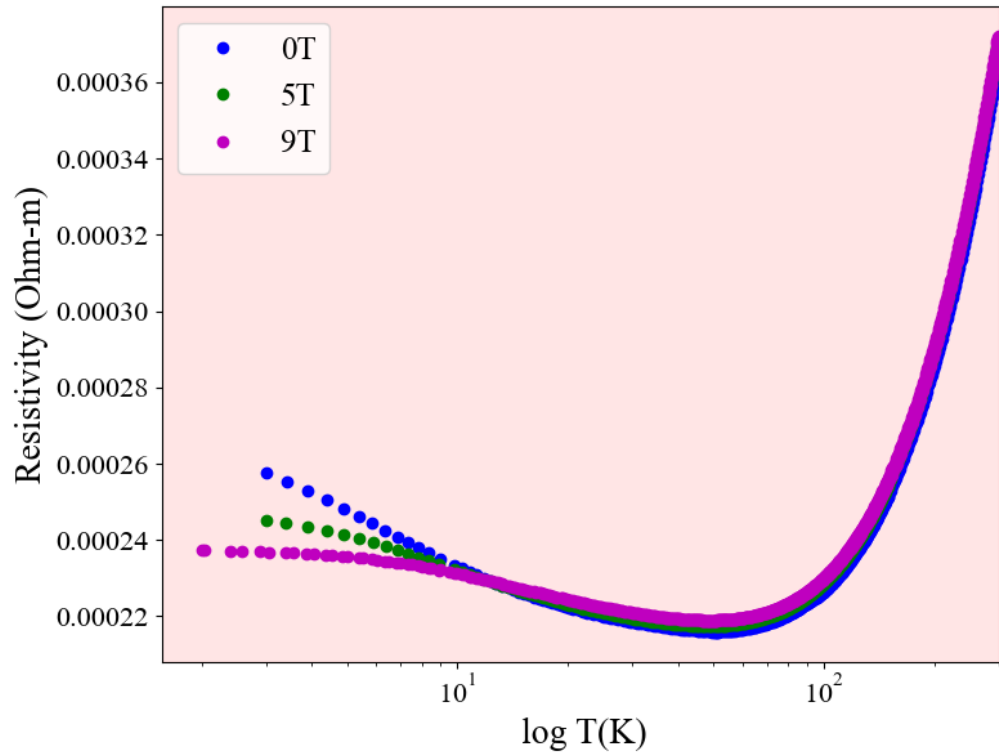


Figure 2.9: Resistivity plot at different applied magnetic fields

Low-temperature upturn in resistivity without applied magnetic is observed to be decreased by application of magnetic field as shown in figure 2.9, which give rise to negative magnetoresistance (NMR) at low temperature. Furthermore, the semi-logarithmic resistivity curve indicates a deviation from linear behavior at low temperatures for applied magnetic fields of 5T and 9T, as compared to the data obtained without a magnetic field.

### 2.4.2 Magnetoresistance (MR)

The MR measurements were carried out using a standard four-probe technique with a magnetic field applied perpendicular to the current direction. Figure 2.10a shows the percentage

magnetoresistance (%MR) plot against applied magnetic field at different temperatures. %MR at a certain temperature is defined as

$$\%MR = \left( \frac{\rho_B - \rho_0}{\rho_0} \right) * 100 \quad 2.3$$

$\rho_B$  is resistivity at applied magnetic field B and  $\rho_0$  is zero field resistivity

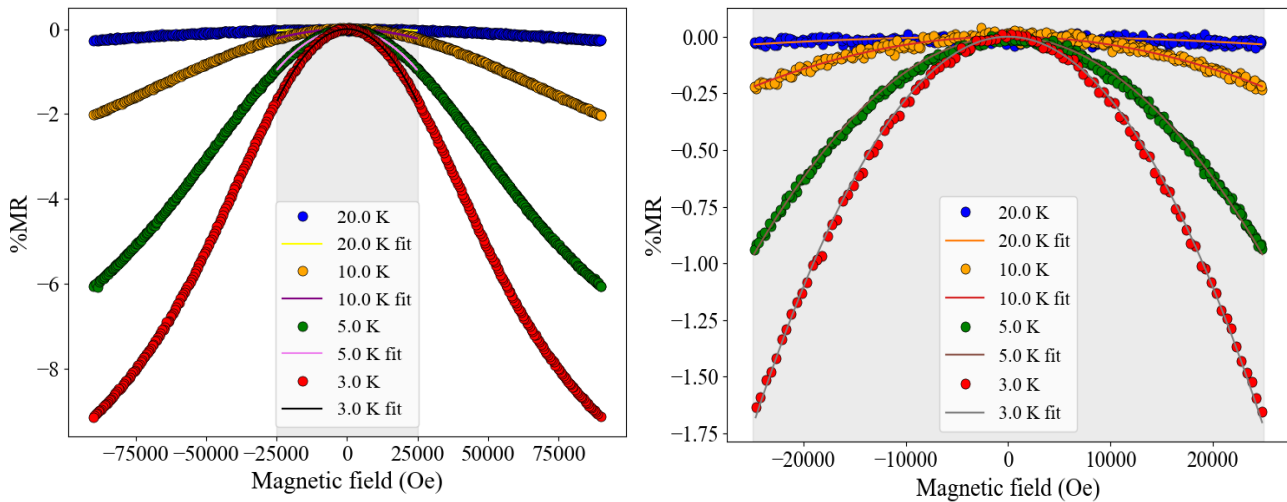


Figure 2.10 : (a) Magnetoresistance vs applied magnetic field for  $Nd_{0.8}Sr_{1.2}NiO_4$  at 3K, 5K, 10K and 20K. (b) Parabolic fit using eq 2.4 for low field (-2.5 to 2.5T)

Experimental studies have shown the parabolic dependence of MR in various Kondo systems such as metals with dilute magnetic impurities, heavy-fermion metals, and magnetic semiconductors. Theoretical models based on the Kondo effect, such as the Anderson model and the Kondo lattice model, also predict the parabolic dependence. To verify this we fit low field magnetoresistance with

$$\%MR = S(T) H^2 \quad 2.4$$

$S(T)$  is magnetoresistance coefficient and depends on the temperature  $T$  and the carrier concentration  $n$ . Fit is performed for the field range -2.5 Tesla to 2.5 Tesla where the MR follows a parabolic dependence with field as observed in Kondo systems (for fit results refer Appendix-A7).

The phenomenon of Negative Magnetoresistance (NMR) was believed to be an artifact from inhomogeneities and disorders in the material. However, later studies showed that the NMR

can also be explained by the scattering of conduction electrons from a localized magnetic moment in the impurity band, which is aligned by the external magnetic field. Khosla and Fischer used 3rd order perturbation theory to come up with a semi empirical formula to explain NMR which is given as [150]

$$\frac{\Delta\rho}{\rho} = -a^2 \ln(1 + b^2 H^2) \quad 2.5$$

the parameters a and b are given by the formula

$$a = A_1 J \rho_F [S(S + 1) + \langle M^2 \rangle] \quad 2.6$$

and

$$b^2 = \left[ 1 + 4S^2 \pi^2 \left( \frac{2J\rho_F}{g_0} \right)^4 \right] \frac{g_0^2 \mu^2}{(\alpha kT)^2} \quad 2.7$$

Here the parameter  $A_1$  is the measure of spin scattering to the total MR,  $J$  is the exchange interaction energy,  $S$  is the spin of the localized magnetic moment,  $g_0$  is the Lande  $g$  factor,  $\langle M^2 \rangle$  is the average magnetization,  $\rho_F$  is the density of state of the fermi energy and  $\alpha$  a numerical constant.

We fit magnetoresistance data with equation 2.5

As evident from the fit, the Khosla and Fischer model that we used does not fully capture the NMR behavior of our system. In particular, the deviation is more prominent for high field values and low temperature (for fit results refer Appendix-A8). The Khosla and Fischer model is based on the assumption that the spin fluctuations are isotropic and Gaussian, which means that they are random and symmetric in all directions.

However, this assumption may not be valid for some systems, especially at high fields and low temperatures, where the impurity spins are more aligned with the external field. Therefore, the Khosla and Fischer model may deviate from the experimental data in this regime

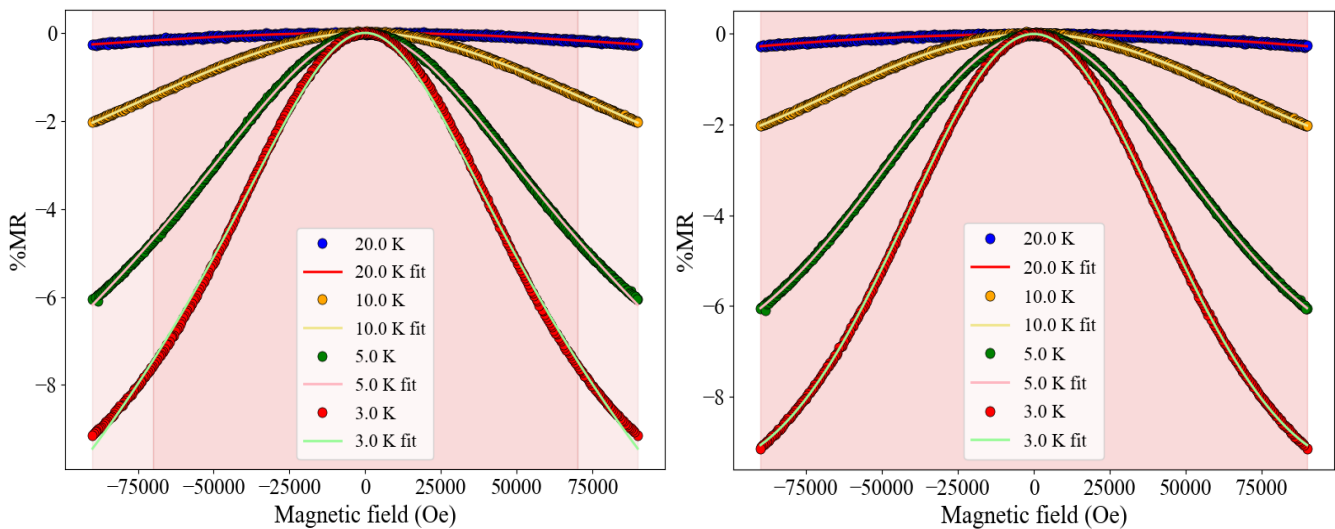


Figure 2.11 : Magnetoresistance vs applied magnetic field for  $Nd_{0.8}Sr_{1.2}NiO_4$  at 3K, 5K, 10K and 20K

(a) fitted with eq 2.5

(b) fitted with eq 2.9

To improve the accuracy and validity of the Khosla and Fischer model, we can use a spin polarization function as a correction term. The spin polarization function is a way of describing how the spin of the impurity atoms is affected by the external magnetic field. It introduces a factor of  $(1 - L^2)$ , where  $L$  is the Langevin function, which describes how much impurity spins are aligned with the field. This factor reduces resistivity at high fields and low temperatures, where impurity spins are more polarized. To incorporate correction term to NMR, we used modified Hamann formula [151] for zero field Kondo resistivity (eq<sup>n</sup> 2.8).

$$\rho(T, B) = \rho_k \rho(T) * \left( 1 - L^2 \left[ \frac{\mu B}{k_B T_{eff}} \right] \right) \quad 2.8$$

$\rho(T)$  is resistivity as a function of temperature.  $T_{eff}$  is defined as  $T_{eff} = \sqrt{T^2 + T_W^2}$ ,  $T_W$  is a measure of the effective RKKY interactions, which are exchange interaction between magnetic moments mediated by conduction electrons in a metal [152].  $T$  is replaced by  $T_{eff}$  in Hamann formula to account for impurity spin  $S$ . Langevin function is mathematically defined as  $(x) = \coth(x) - \frac{1}{x}$ . Now correction to magnetoresistance

$$\left( \frac{\Delta\rho}{\rho} \right)_c = \frac{\rho(T, B) - \rho(T, B = 0)}{\rho(T, B = 0)}$$

$$\left( \frac{\Delta\rho}{\rho} \right)_c = \rho_k L^2 \left[ \frac{\mu B}{k_B T_{eff}} \right]$$

$$\frac{\Delta\rho}{\rho} = -a^2 \ln(1 + b^2 H^2) + \rho_k L^2 \left[ \frac{\mu B}{k_B T_{eff}} \right] \quad 2.9$$

Table 2.8: Parameters from fit to MR data using equation 2.9

Temperature (K)	a	b	$\rho_k$
3.0	$3.61 \pm 0.03$	$-2.19\text{e-}11 \pm 1.31\text{e-}13$	$-1.59\text{e-}09 \pm 2.87\text{e-}11$
5.0	$3.05 \pm 0.02$	$-1.89\text{e-}11 \pm 8.01\text{e-}14$	$-3.92\text{e-}10 \pm 6.33\text{e-}12$
10.0	$3.08 \pm 0.20$	$-1.03\text{e-}11 \pm 4.05\text{e-}13$	$-1.18\text{e-}10 \pm 1.56\text{e-}11$
20.0	$0.0189 \pm 0.0071$	$6.48\text{e-}04 \pm 0.0077$	$-4.51\text{e-}11 \pm 3.43\text{e-}13$

Fit results indicate that our correction provides a good description of the Magnetoresistance. The fitted parameters, including  $a$ ,  $b$  and  $\rho_k$ , are estimated with relatively small uncertainties, indicating the precision of the fit. The low chi-square values for all temperature points further support the goodness of fit (refer appendix A-9). The extracted parameters from the fit provide insights into the temperature dependence of the magnetoresistance.

In absence of a magnetic field, Kondo effect arises from coupling between localized magnetic moments and conduction electrons, leading to formation of singlet states that screen magnetic impurities. In presence of magnetic field, Zeeman effect on localized magnetic moments causes them to align with the field. The Zeeman effect is splitting of energy levels of a magnetic system due to an external magnetic field. It depends on effective magnetic moment of localized magnetic moments and strength of external magnetic field. As result, formation of Kondo singlets is disrupted, leading to decrease in Kondo effect. This is because aligned moments can no longer effectively interact with conduction electrons to form singlet states. The interaction between localized magnetic moments and conduction electrons is mediated by exchange interaction, which tends to align their spins in opposite directions. The exchange interaction depends on overlap between wave functions of localized magnetic moments and conduction electrons. When localized magnetic moments are aligned with the field, their wave functions become more narrow and less overlapping with conduction electrons, which reduces exchange interaction and disrupts formation of Kondo singlets.

Furthermore, magnetic field can increase energy scale associated with Kondo effect, making it less dominant at higher field strengths. This occurs because Zeeman energy of localized magnetic moments becomes comparable to or larger than Kondo temperature, leading to reduction in Kondo effect [153]–[155].

### 2.4.3 Magnetization measurements

Magnetization of  $\text{Nd}_{0.8}\text{Sr}_{1.2}\text{NiO}_4$  samples are measured using SQUID (Superconducting Quantum Interference Device) magnetometer. We performed Zero Field Cooled (ZFC) and Field Cooled (FC) measurements. In ZFC measurement, the sample is first cooled down to 3K in the absence of an external magnetic field. Then, the external magnetic field is applied, and the magnetization of the sample is measured as a function of temperature while warming it up. In FC measurement, the process is repeated by cooling the sample with an applied magnetic field. The ZFC and FC curves may exhibit different behavior due to the presence of magnetic domains in the sample. The ZFC curve will be dominated by the magnetic domains that have not yet aligned with the applied magnetic field, while the FC curve will be influenced by the domains that have already aligned with the field during cooling. ZFC and FC curves for the susceptibility of  $\text{Nd}_{0.8}\text{Sr}_{1.2}\text{NiO}_4$  samples are shown in figure 2.12. Interestingly, the ZFC and FC curves showed no notable differences. This indicates that the magnetic properties of the sample do not depend on the history of the sample's cooling process. In other words, the sample does not exhibit any significant magnetic hysteresis. Inset plot in the figure 2.13 shows the inverse susceptibility curve, to show

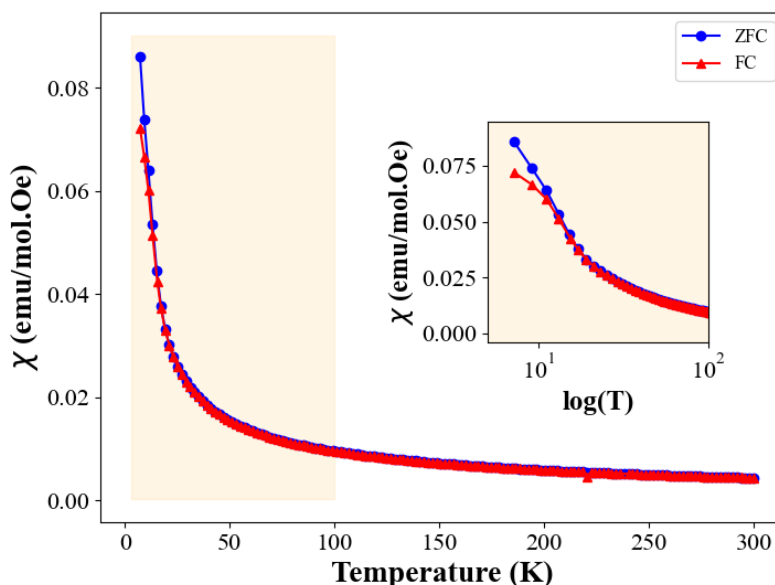


Figure 2.12: ZFC, FC Susceptibility data for  $\text{Nd}_{0.8}\text{Sr}_{1.2}\text{NiO}_4$ , Inset shows low temperature susceptibility in semi-log plot

the linear region is above 130K as below 130K the data clearly deviate from a Curie-Weiss behavior. We analyzed the susceptibility and the inverse susceptibility data for  $\text{Nd}_{0.8}\text{Sr}_{1.2}\text{NiO}_4$  samples using Curie-Weiss law

$$\chi(T) = \frac{C}{T - \Theta} \quad 2.10$$

$\chi$  is the magnetic susceptibility,  $T$  is the absolute temperature,  $C$  is the Curie constant,  $\Theta$  is the modified Curie-Weiss temperature. This law should only be applied to Curie-Weiss region, which identified as linear region in inverse susceptibility curve [156].

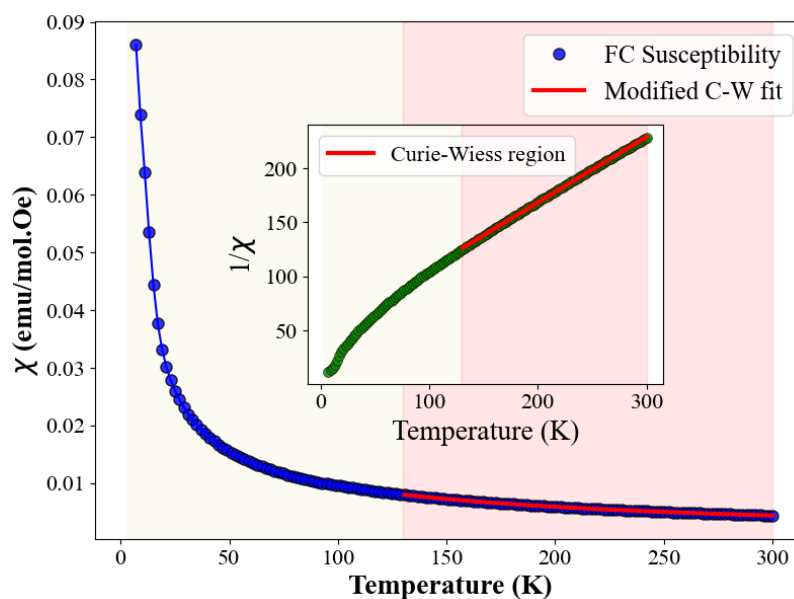


Figure 2.13: ZFC- Susceptibility fitted with modified Curie-Weiss law.

Table 2.9: Parameters obtained from a fit to the Susceptibility temperature for  $\text{Nd}_{0.8}\text{Sr}_{1.2}\text{NiO}_4$  using equation 2.10 in the temperature range 130 to 300K

Parameter	Value from fit
$C$	1.62 (emu-K/mol)
$\Theta$	(-74.30 +/- 0.36) K

Effective magnetic moment can be calculated using the value of the Curie constant obtained from the fit as  $\mu_{eff} = \sqrt{8C} \mu_B$ ,  $\mu_B$  is Bohr magneton.  $\mu_{eff} = 3.6\mu_B$ .

In  $\text{Nd}_{0.8}\text{Sr}_{1.2}\text{NiO}_4$ , we can expect to have  $\text{Ni}^{3+}$  and  $\text{Ni}^{4+}$  in 4:1 ratio and  $\text{Ni}^{3+}$  can be either in low spin (LS) or high spin (HS). The preference for either the low spin or high spin configuration depends on factors such as the strength of the crystal field, the ligand environment, and the electron filling of the d orbitals. These factors influence the energy difference between the available orbitals and the electron-electron repulsion, leading to the stabilization of one configuration over the other. We can calculate spin-only magnetic moment ( $\mu_{SO}$ ) of  $\text{Nd}_{0.8}\text{Sr}_{1.2}\text{NiO}_4$  per formula unit, for both low spin (LS) and high spin (HS)  $\text{Ni}^{3+}$  ions separately.

$$\mu_{SO} = \sqrt{n(n+2)} \mu_B \quad n \text{ is the number of unpaired electrons}$$

- For low spin (LS)  $\text{Ni}^{3+}$ :  $n=1$ ,  $\mu(\text{Ni}_{LS}^{3+}) = 1.41 \mu_B$

$$\text{Per formula unit } \mu(\text{Ni}_{LS}^{3+}) = 0.8 * \mu(\text{Ni}_{LS}^{3+}) = 0.8 * 1.41 = 1.12\mu_B$$

- For high spin (HS)  $\text{Ni}^{3+}$ :  $n=3$ ,  $\mu(\text{Ni}_{HS}^{3+}) = 3.87 \mu_B$

$$\text{Per formula unit } \mu(\text{Ni}_{HS}^{3+}) = 0.8 * \mu(\text{Ni}_{HS}^{3+}) = 0.8 * 3.87 = 3.096\mu_B$$

- For  $\text{Ni}^{4+}$ :  $\mu(\text{Ni}^{4+}) = 0 \mu_B$
- For  $\text{Nd}^{3+}$ :  $\mu(\text{Nd}^{3+}) = 3.62 \mu_B$  (with L-S coupling scheme)

$$\text{Per formula unit } \mu(\text{Nd}^{3+}) = 0.8 * \mu(\text{Nd}^{3+}) = 0.8 * 3.62 = 2.896\mu_B$$

For  $\text{Nd}_{0.8}\text{Sr}_{1.2}\text{NiO}_4$  with LS  $\text{Ni}^{3+}$ :

$$\mu_{eff}(\text{LS}) = \sqrt{[\mu(\text{Ni}_{LS}^{3+})]^2 + [\mu(\text{Nd}^{3+})]^2}$$

$$\mu_{eff}(\text{LS}) = \sqrt{[1.41]^2 + [2.896]^2}$$

$$\mu_{eff}(\text{LS}) = 3.22 \mu_B$$

For  $\text{Nd}_{0.8}\text{Sr}_{1.2}\text{NiO}_4$  with HS  $\text{Ni}^{3+}$ :

$$\mu_{eff}(\text{HS}) = \sqrt{[\mu(\text{Ni}_{HS}^{3+})]^2 + [\mu(\text{Nd}^{3+})]^2}$$

$$\mu_{eff} (HS) = \sqrt{[3.87]^2 + [2.896]^2}$$

$$\mu_{eff} (HS) = 4.83 \mu_B$$

Therefore, the calculated  $\mu_{SO}$  per formula unit of  $\text{Nd}_{0.8}\text{Sr}_{1.2}\text{NiO}_4$ , considering both low spin (LS) and high spin (HS)  $\text{Ni}^{3+}$   $3.22 \mu_B$  for LS  $\text{Ni}^{3+}$  and approximately  $4.83 \mu_B$  for HS  $\text{Ni}^{3+}$ . Comparing the value  $3.6 \mu_B$  obtained from Curie-Weiss fit, it appears we have low spin  $\text{Ni}^{3+}$  along with non-magnetic  $\text{Ni}^{4+}$ . A Curie temperature of  $-74.3$  K obtained from the fit suggests an antiferromagnetic-like ground state.

Further insights on the observed magnetic properties of  $\text{Nd}_{0.8}\text{Sr}_{1.2}\text{NiO}_4$  obtained from DFT calculations. From the electronic structure calculations on  $\text{La}_{0.8}\text{Sr}_{1.2}\text{NiO}_3$ , exploring various magnetic orders such as non-magnetic (NM), ferromagnetic (FM), and different antiferromagnetic (AFM) phases, they found a preference for AFM interactions in the magnetic moments' alignment. This insight further suggested that the ground state magnetic order likely demonstrates paramagnetic (PM) or AFM-like behavior, consistent with the experimental magnetic measurements. They also calculated the average magnetic moment to compare it with the experimental value. The calculated average magnetic moment per formula unit was estimated to be  $(3.29 \pm 0.17) \mu_B$ , which is comparable with the value derived from the Curie-Weiss fit in our magnetic measurements. Furthermore, their investigations revealed no indication of charge or spin stripe ordering, nor any evidence of a complex distortion involving oxygen, thus ruling out the presence of hidden phase transitions that could account for the observed resistivity upturn.

#### 2.4.4 Discussion on the physical properties of $\text{Nd}_{0.8}\text{Sr}_{1.2}\text{NiO}_4$

The observed non-Fermi liquid behavior with  $n = 1.5$  from power law resistivity model implies that our system has entered a regime where the traditional assumptions of Fermi liquid theory no longer hold. Fermi liquid theory is based on the assumption that the interactions between the fermions are weak and that the system can be treated as a collection of non-interacting quasiparticles. This agrees with the fact that our sample,  $\text{Nd}_{0.8}\text{Sr}_{1.2}\text{NiO}_4$  is overdoped and the traditional assumptions of Fermi liquid theory no longer hold. To account for the low temperature resistivity upturn, we managed to fit logarithmic term in  $T$ , which is characteristic temperature dependence on resistivity in Kondo like system at low temperature. Presence of  $\text{Nd}^{3+}$  in the lattice, which could act as a magnetic impurity and as scattering centers for the conduction electrons backed our assumption of Kondo like scattering. Furthermore, the observed negative magnetoresistance (MR) at low temperatures, which fall below the Kondo crossover temperature (19K) determined from the analysis of resistivity data, suggests the presence of Kondo-like behavior in the system. Additionally, the magnetoresistance at low magnetic fields exhibits a parabolic dependence, resembling the characteristic behavior observed in Kondo systems. In the context of Kondo scattering in  $\text{Nd}_{0.8}\text{Sr}_{1.2}\text{NiO}_4$ , the NMR contribution occurs due to the disruption of the Kondo singlet state. When an external magnetic field is applied, it perturbs the Kondo singlet formation, leading to a reduction in the effectiveness of screening the localized magnetic moments by the conduction electrons. As a result, the scattering processes associated with the impurities increase. However, it is important to note that the Kondo contribution to resistivity typically dominates over the scattering processes caused by the impurities, which leads to a strong renormalization of the electron scattering, resulting in a decrease in resistivity. Hence, the disruption of the Kondo singlet state by the applied magnetic field ultimately leads to a decrease in resistivity, contributing to the NMR phenomenon.

## 2.5 Physical characterizations of $\text{Nd}_{0.8}\text{Sr}_{1.2}\text{NiO}_3$

### 2.5.1 Resistivity measurement

We performed the four-probe resistivity measurement for  $\text{Nd}_{0.8}\text{Sr}_{1.2}\text{NiO}_3$  samples, as discussed in the case of  $\text{Nd}_{0.8}\text{Sr}_{1.2}\text{NiO}_4$  samples.  $\text{Nd}_{0.8}\text{Sr}_{1.2}\text{NiO}_3$  samples found to be highly insulating till low temperatures (Resistance measured was beyond the measurable limit of PPMS ( $>10^6 \Omega$ )).

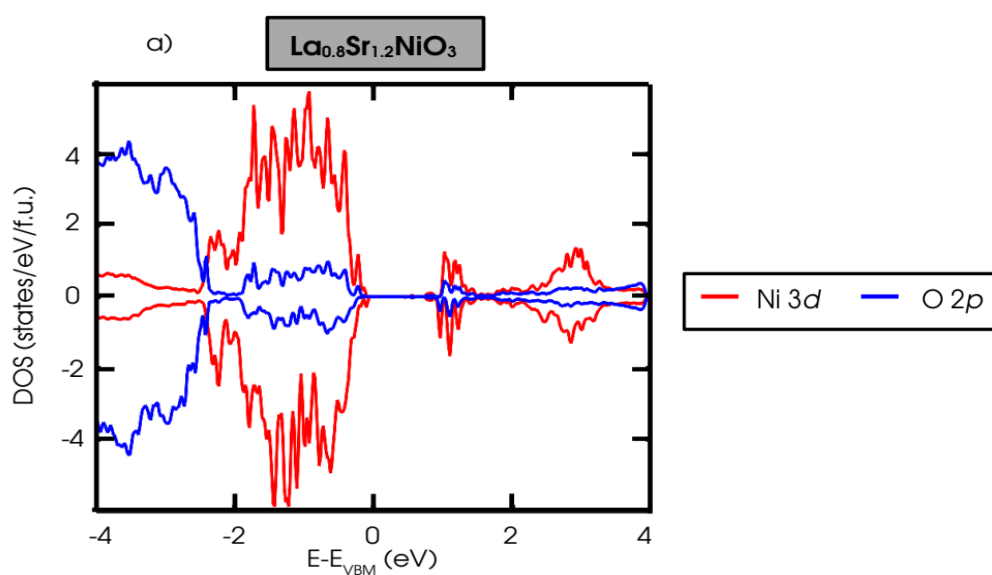


Figure 2.14: Projected density of states on Ni 3d in red and O 2p in blue for  $\text{La}_{0.8}\text{Sr}_{1.2}\text{NiO}_3$

Our findings are corroborated by DFT calculations performed on  $\text{La}_{0.8}\text{Sr}_{1.2}\text{NiO}_3$ . An analysis of the Density of States (DOS) reveals the insulating nature of this system, marked by a bandgap amplitude of  $E_g = 1.1\text{eV}$ , as illustrated in Figure 2.14. The density of states diagram clearly displays a gap between the occupied and unoccupied Ni-3d states, indicative of the material's classification as a Mott insulator. This gap arises due to strong electron-electron interactions, specifically the Coulomb repulsion between electrons in the same atomic or molecular orbitals. This observation is intriguing because the parent compound resides closer to the charge transfer regime, as discussed earlier in Figure 2.7, while the reduced one in the Mott regime. It's

safe to conclude that the removal of in-plane oxygen atoms diminishes the number of carriers and disrupts potential conductive pathways. Consequently, the Ni 3d states assume a prominent role in governing the transport properties of the material.

### 2.5.2 Magnetization measurements

Similar ZFC, FC measurements as discussed in section 2.3.2 performed for the reduced samples. The absence of a paramagnetic region in the temperature range of the measurement indicates that the material being studied does not exhibit paramagnetic behavior within the temperature range where the measurement is carried as shown in figure 2.15. In such cases, it is not possible to perform a Curie-Weiss analysis. Interestingly, ZFC and FC curves starts to bifurcate at very high temperature. Likely explanations for this phenomenon include magnetic relaxation, presence of magnetic impurities, domain wall pinning and spin-glass behavior. Spin-glasses are disordered magnetic systems that exhibit a slow magnetic response, characterized by a frequency-

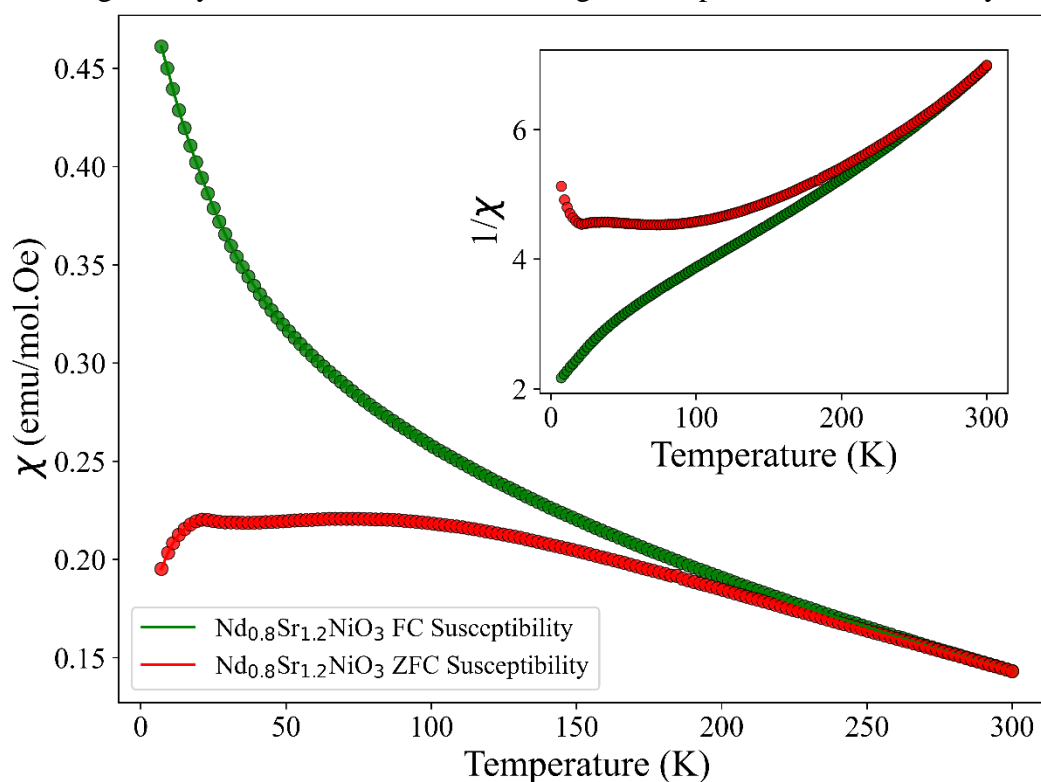


Figure 2.15: Susceptibility vs temperature measured in ZFC and FC method for  $Nd_{0.8}Sr_{1.2}NiO_3$ . Inset shows Inverse susceptibility curve, shows non-Curie-Weiss behavior till 300K

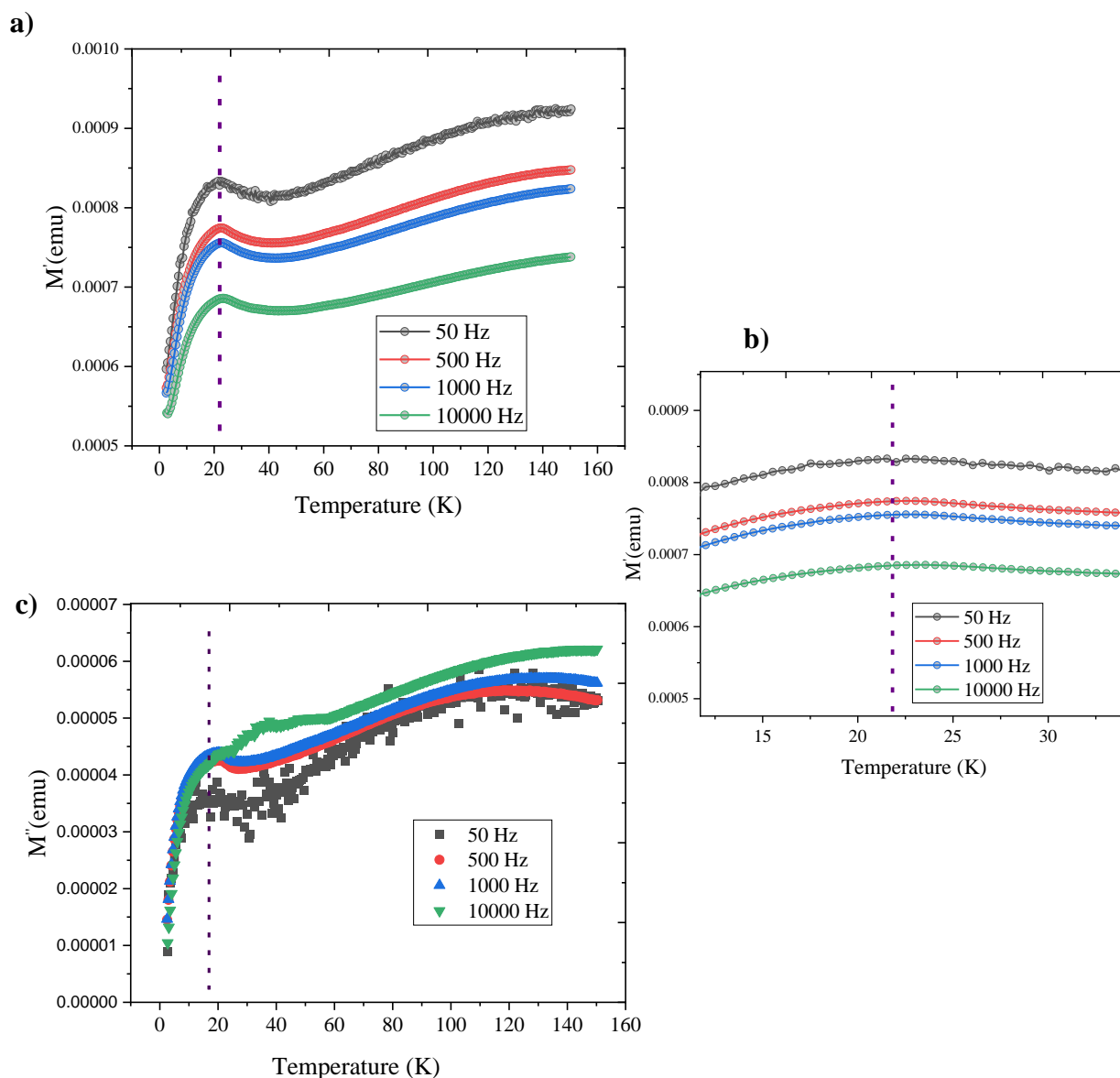


Figure 2.16: AC-susceptibility measured in ZFC method for  $\text{Nd}_{0.8}\text{Sr}_{1.2}\text{NiO}_3$  at different ac frequency

(a) Real part ( $M'$ )

(b) Enlarged view of Real part ( $M'$ ) near peak

(c) Imaginary part ( $M''$ )

dependent peak in the AC susceptibility [157]. Possibility of spin glass behavior is ruled out, as the peak in the AC susceptibility is independent of the frequency as shown in the figure 2.16. The presence of impurities or defects is often associated with ZFC-FC bifurcation in the sample. In our case, the reduction process may have introduced magnetic impurities or defects into the sample,

leading to the observed ZFC-FC bifurcation in the reduced sample. Neutron diffraction studies should be performed to have a conclusive picture of the magnetic structure of the compound and to explain the observed ZFC -FC bifurcation.

## 2.6 SUMMARY AND DISCUSSION

CaH<sub>2</sub> based topotactic reduction successfully transformed tetragonal-I4/mmm Nd<sub>0.8</sub>Sr<sub>1.2</sub>NiO<sub>4</sub> into orthorhombic-Immm Nd<sub>0.8</sub>Sr<sub>1.2</sub>NiO<sub>3</sub>. Both phases are quite stable in ambient. Structural characterizations revealed that, unlike the perovskite case, the O atoms have been removed from the plane and not from the apex of the octahedra, producing a structure of NiO<sub>2</sub> square stripes along one of the in-plane lattice parameters. This can be explained by the fact that unlike perovskite, K<sub>2</sub>NiF<sub>4</sub> type Nd<sub>0.8</sub>Sr<sub>1.2</sub>NiO<sub>4</sub> structure consists of two-dimensional slabs of perovskite-like layers that are one NiO<sub>6</sub> octahedron thick, separated by a layer of Nd/Sr cations which form a rock salt layer with the apical oxygen from the perovskite-like layer. Apical oxygen here are strongly bonded to the Nd/Sr cations in the rock salt layer, which have a lower coordination number and a higher charge than the Ni cations in the perovskite layer. This makes the removal of apical oxygen more difficult or energetically less favorable than in-plane oxygen from perovskite layer. This observation further supported by DFT calculations by comparing the total energy of the different configurations possible from reduction. Transport measurements shown that upon reduction electrical properties of Nd<sub>0.8</sub>Sr<sub>1.2</sub>NiO<sub>4</sub> changes from metallic to highly insulating for Nd<sub>0.8</sub>Sr<sub>1.2</sub>NiO<sub>3</sub> till low temperature. This further supported by calculations on the reduced phase, which suggest an insulating ground state with a gap amplitude  $E_g = 1.1$  eV. In addition, gap between the occupied and unoccupied Ni 3d states suggest that Nd<sub>0.8</sub>Sr<sub>1.2</sub>NiO<sub>3</sub> can be classified as a Mott insulator. This observation is intriguing as it indicates a transition from the charge transfer regime in the parent compound to the Mott regime in the reduced compound. It suggests that by removing the in-plane oxygen atoms, we effectively deplete the charge carriers in the material. This depletion causes a downward shift of the O-2p band towards lower energies, while the Ni-3d states become the primary contributors to the transport properties of the system. From the magnetic studies, Nd<sub>0.8</sub>Sr<sub>1.2</sub>NiO<sub>4</sub> showed paramagnetic behavior in the temperatures above 130K with an antiferromagnetic ground state suggested from Curie-Weiss analysis. In contrast, Nd<sub>0.8</sub>Sr<sub>1.2</sub>NiO<sub>3</sub>

showed ZFC-FC bifurcation starting from above room temperature. The AC susceptibility measurement excluded the possibility of spin-glass-type behavior. To obtain a conclusive understanding of the magnetic structure and to explain the origin of this behavior, further neutron diffraction studies are warranted.



Thin film nickelates:  
Epitaxial growth and topotactic  
reduction

## 3.1 Introduction

As emphasized in the initial chapter, the number of experimental works that have achieved superconductivity represents only a small fraction within the extensive body of follow-up studies. Therefore, it is crucial to acknowledge the issue of reproducibility, particularly regarding the reduction process. Adapting the protocols of research groups who have reported successful attempts does not necessarily lead to the desired results. Besides, for those groups that have achieved success, repeated attempts at synthesis with many samples are still necessary in order to increase the chances of obtaining a superconducting sample. Following the report of superconductivity in infinite layer  $\text{Nd}_{0.8}\text{Sr}_{0.2}\text{NiO}_2$ , our research group at CRISMAT embarked on this task to validate their results. To provide context, I begin by discussing the synthesis methodologies employed by the initial two groups that successfully synthesized and observed superconductivity in infinite-layer nickelates. By understanding their synthesis approaches, we aimed to establish a foundation for our own experimental efforts.

Li et al. from Harold Hwang's group at Stanford University was the first group to report superconductivity in infinite-layer nickelates. They fabricated  $\text{Nd}_{0.8}\text{Sr}_{0.2}\text{NiO}_2$  thin films by pulsed laser deposition (PLD) on  $\text{TiO}_2$ -terminated  $\text{SrTiO}_3$  (STO) substrates, with epitaxial  $\text{SrTiO}_3$  capping layers and sealed samples in a Pyrex glass tube along with  $\text{CaH}_2$  powder and heated to 260-280°C for 4-6 hours [68]. With a protracted effort in optimizing the process parameters, they managed to realize superconducting nickelate thin films with a thickness of  $\sim 10\text{nm}$ . X-ray diffraction analysis showed (figure 3.1a) clear single-crystal peaks corresponding to the (001) and (002) orientations of  $\text{Nd}_{0.8}\text{Sr}_{0.2}\text{NiO}_2$ . The temperature-dependent resistivity measurements (figure 1.2b) revealed a superconducting transition with an onset temperature of 14.9K for the hole-doped  $\text{Nd}_{0.8}\text{Sr}_{0.2}\text{NiO}_2/\text{SrTiO}_3$  thin film. Here, capping the nickelate film with a subsequent  $\text{SrTiO}_3$  layer provided an epitaxial template to the top region of the nickelate film, much like the substrate. This helped them to stabilize superconducting single-phase  $\text{Nd}_{0.8}\text{Sr}_{0.2}\text{NiO}_2$  (001) epitaxial thin films up to  $\sim 10\text{nm}$ .

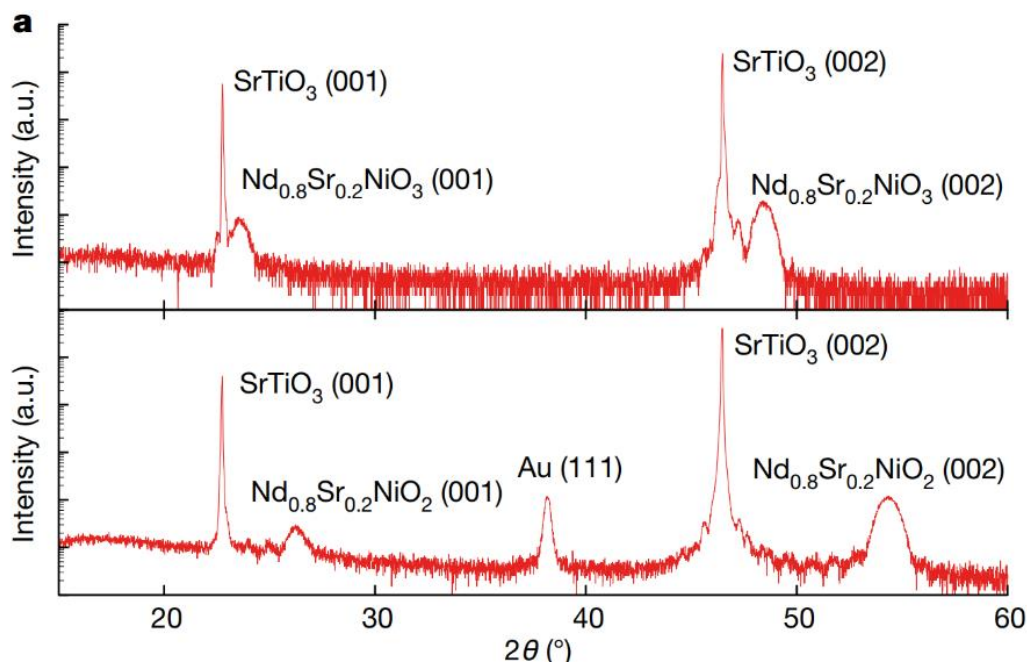


Figure 3.1: (adapted from ref 11) X-ray diffraction  $\theta$ - $2\theta$  symmetric scans  $\text{Nd}_{0.8}\text{Sr}_{0.2}\text{NiO}_3$  and  $\text{Nd}_{0.8}\text{Sr}_{0.2}\text{NiO}_2$  of films capped with 20-nm-thick  $\text{SrTiO}_3$  layers grown on  $\text{SrTiO}_3$  (001) substrates

Zeng et al. from Ariando's group at the National University of Singapore adapted an alternative approach for the synthesis of superconducting nickelate thin films without capping film with of STO layer [63]. In contrast to sealed tube chemical reduction method, they utilized a pulsed laser deposition (PLD) chamber for reduction. They wrapped pre-grown  $\text{Nd}_{1-x}\text{Sr}_x\text{NiO}_3$  thin films, with a thickness of 35 nm in aluminum foils, embedded within  $\text{CaH}_2$  powder, were then introduced into the PLD chamber. The PLD chamber was subsequently heated to temperatures ranging from 340 to 360 °C, and the process was carried out for a duration of 80 to 120 minutes. Figure 3.2(b) shows resistivity versus temperature ( $\rho$ -T) curves of the  $\text{Nd}_{1-x}\text{Sr}_x\text{NiO}_2$  thin films synthesized by Zeng et al. for different values of  $x$  ranging from 0.08 to 0.3. For  $x$  values between 0.08 and 0.12, the samples exhibit a metallic behavior at high temperatures, with a resistivity minimum observed between 27K and 35K. Below this temperature range, a weakly insulating behavior is observed. In the range of  $0.135 \leq x \leq 0.22$ , the samples exhibit superconductivity, and the  $\rho$ -T curves resemble those of a metal above the superconducting transition temperature. They observed a superconducting dome spanning the range of  $x$  values between 0.12 and 0.235 in the  $\text{Nd}_{1-x}\text{Sr}_x\text{NiO}_2$  thin films

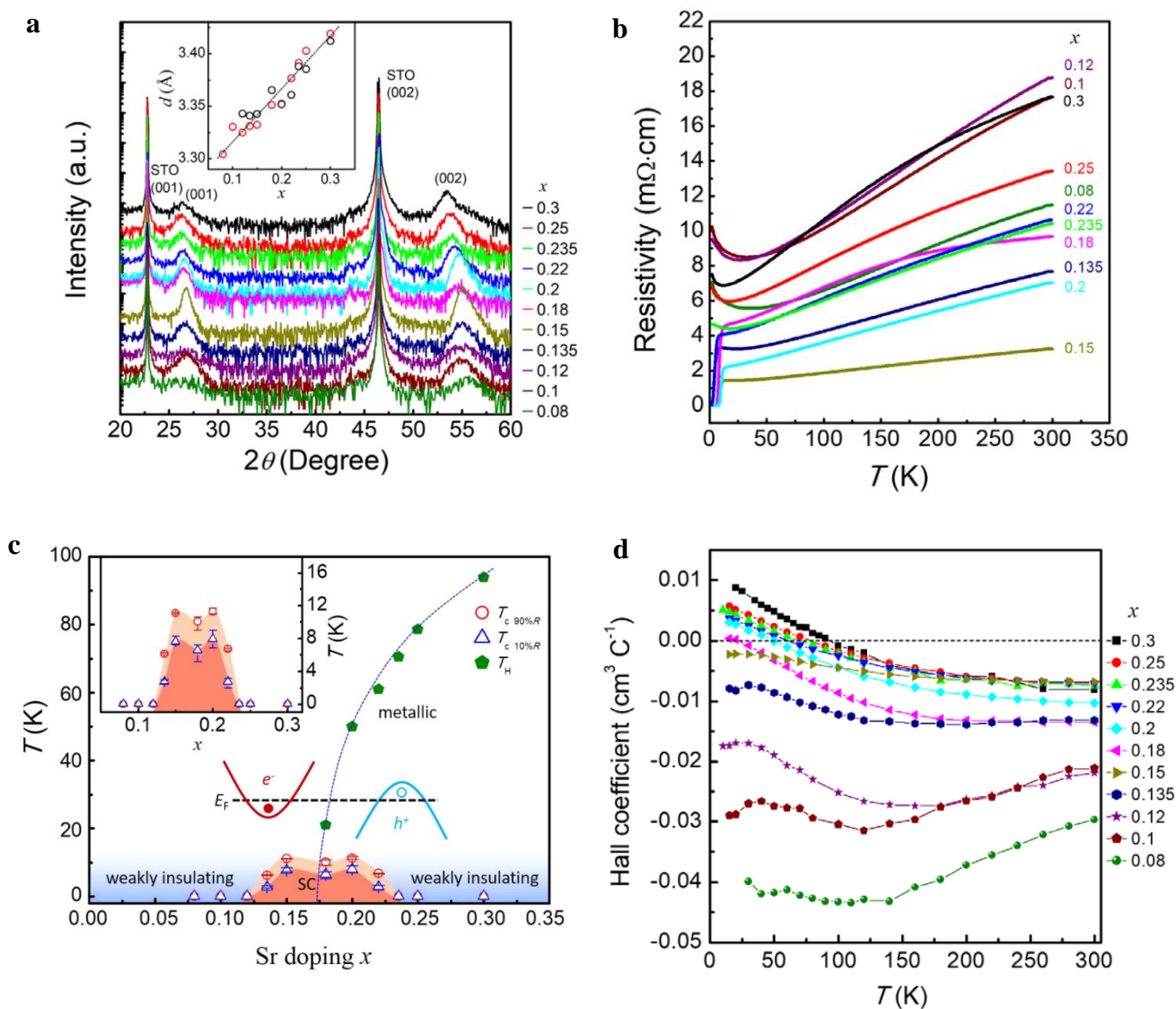


Figure 3.2 (adapted from ref 63):

- The XRD  $\theta$ - $2\theta$  scan patterns of the  $\text{Nd}_{1-x}\text{Sr}_x\text{NiO}_2$  thin films on a STO substrate
- The resistivity versus temperature ( $\rho$ - $T$ ) curves of the  $\text{Nd}_{1-x}\text{Sr}_x\text{NiO}_2$  thin films with Sr doping level  $x$  from 0.08 to 0.3
- Superconducting dome of  $\text{Nd}_{1-x}\text{Sr}_x\text{NiO}_2$ . The inset in the upper left corner provides an enlarged view of the superconducting dome, while the bottom inset schematically illustrates the electron band ( $e^-$ ) and hole band ( $h^+$ ) that dominate the charge carriers in the two panels separated by the  $T_H$ - $x$  curve. The black dashed line in the inset represents the Fermi energy ( $E_F$ ).
- The temperature dependence of the  $R_H$  for the  $\text{Nd}_{1-x}\text{Sr}_x\text{NiO}_2$ . A blue dashed line is included as a visual guide

Figure 3.2c provides information on the critical temperature ( $T_c$ ) and the temperature ( $T_H$ ) at which the Hall coefficient ( $R_H$ ) changes from negative to positive. The  $T_{c\ 90\%R}$  ( $T_{c\ 10\%R}$ ) values indicate the temperature at which the resistivity drops to 90% (10%) of the value at 15 K, which marks the onset of superconductivity.  $T_H$  is defined as the temperature at which the  $R_H$  curve intersects the zero axis in Figure 3.2d.

The two major technical issues reported by the groups in the synthesis were the stabilization of the doped perovskite phase and the balance between complete topotactic reduction vs subsequent decomposition. The presence of Ruddlesden-Popper-type secondary phases is problematic for the synthesis of superconducting infinite-layer nickelates because they introduce impurities and structural defects that can negatively impact the superconducting properties of the material. To achieve single-crystalline, single-phase superconducting  $\text{Nd}_{0.8}\text{Sr}_{0.2}\text{NiO}_2$ , it is essential to stabilize the precursor perovskite  $\text{Nd}_{0.8}\text{Sr}_{0.2}\text{NiO}_3$  thin film without visible impurity phases. In the parent compound  $\text{NdNiO}_3$ , the Ni ion typically has a 3+ valence state. However, when Sr dopants are introduced, the additional Sr ions need to accommodate the charge balance. To maintain overall charge neutrality, the Ni ion must adopt a higher valence state than 3+ to compensate for the additional positive charge from the Sr dopants. Achieving a higher valence state for Ni can be challenging due to the electronic configuration and stability of the transition metal ions. The 3+ valence state of Ni is already quite stable, and promoting it to a higher valence state requires additional energy. It may involve overcoming energy barriers associated with electron transfer and electronic restructuring within the crystal lattice. The difficulty in synthesizing the parent compound  $\text{Nd}_{1-x}\text{Sr}_x\text{NiO}_3$  may arise from the need to precisely control and stabilize the higher valence state of Ni.

## 3.2 Preliminary works on infinite layer nickelates in CRISMAT

Motivated by the exciting results on superconductivity in infinite layer nickelates, our group immediately started investigating the nickelate system. Our objective was to validate the results and investigate further on the physical and chemical properties of this new superconducting family.

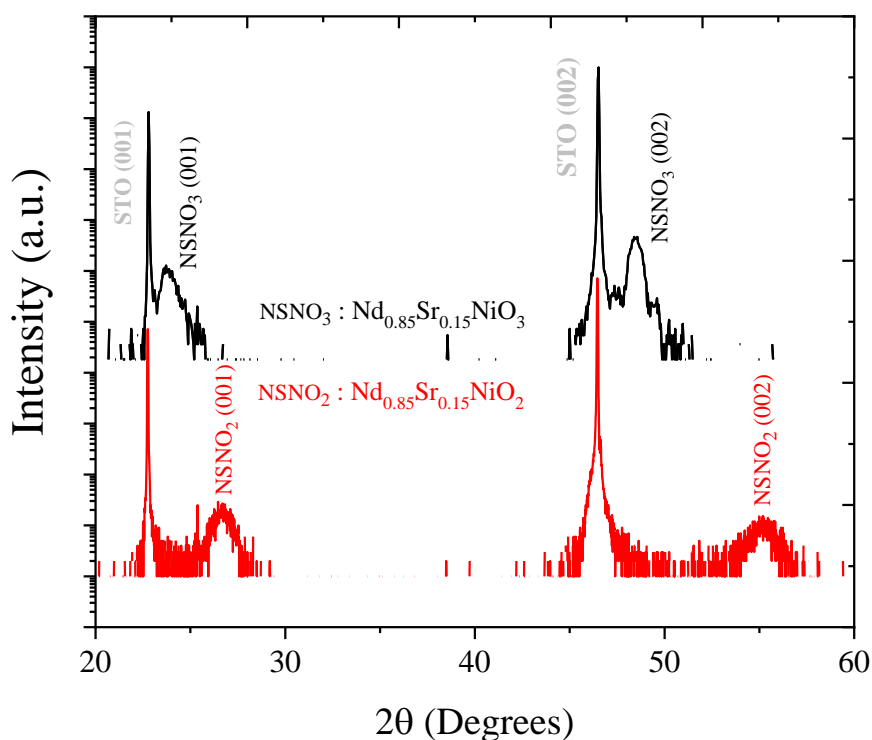


Figure 3.3

*Thin film XRD patterns of  $\text{Nd}_{0.85}\text{Sr}_{0.15}\text{NiO}_3$  and  $\text{Nd}_{0.85}\text{Sr}_{0.15}\text{NiO}_2$  thin films on STO substrate*

Dr. Maryline NASR from our group focused on synthesizing  $\text{Nd}_{1-x}\text{Sr}_x\text{NiO}_3$  and reducing it to infinite layer  $\text{Nd}_{1-x}\text{Sr}_x\text{NiO}_2$  using  $\text{CaH}_2$ . Furthermore, she made concerted efforts to enhance the phase purity of the PLD target and employed various chemical techniques to promote the prevalence of perovskite phases within the PLD target, a task that posed considerable challenges.

Primary task was to optimize PLD parameters for perovskite  $\text{Nd}_{0.85}\text{Sr}_{0.15}\text{NiO}_3$  thin films on STO substrate. Key PLD parameters, including an oxygen partial pressure of 0.15mbar, a laser operating conditions of output energy of 200mJ with a repetition rate of 2Hz, a target-to-substrate distance of 4 cm, and a substrate temperature of 600°C, were determined as optimal for the deposition process. Perovskite  $\text{Nd}_{1-x}\text{Sr}_x\text{NiO}_3$  films on STO (001) substrates are characterized by second order peak close to  $2\theta = 48^\circ$  and presence of well-defined first order diffraction peak in the thin film x-ray diffraction pattern. Figure 3.3 displays thin film XRD pattern for the  $\text{Nd}_{0.85}\text{Sr}_{0.15}\text{NiO}_3$  film on an STO (001) substrate. A distinct second-order peak at  $2\theta=48.4^\circ$  corresponds to a lattice parameter of 3.79Å and a well-defined first order diffraction peak confirms the prevailing perovskite nature of our film. This perovskite dominance is a crucial prerequisite for

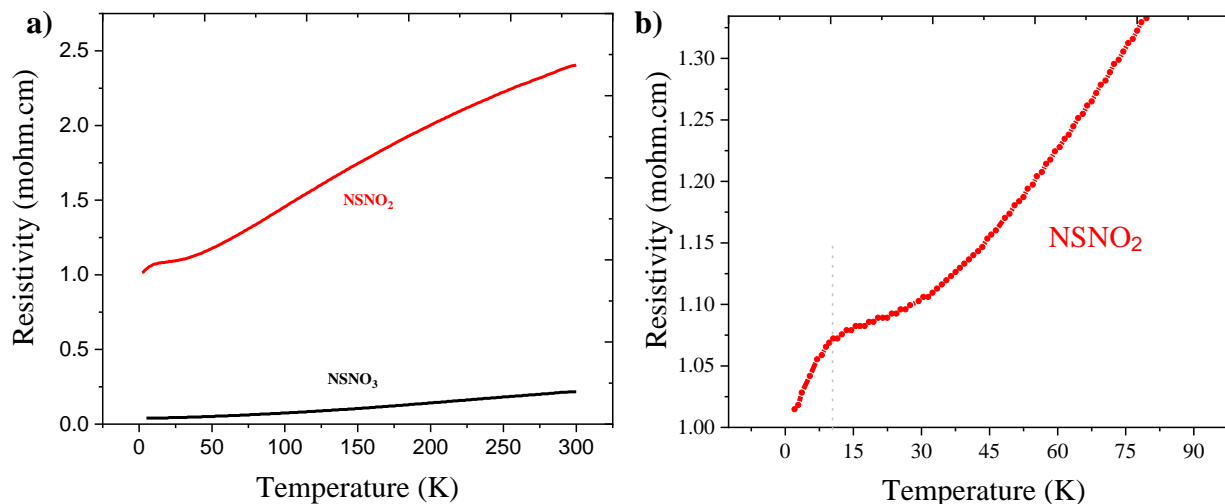


Figure 3.4:

(a) Four probe resistivity measurements on  $\text{Nd}_{0.85}\text{Sr}_{0.15}\text{NiO}_3$  and  $\text{Nd}_{0.85}\text{Sr}_{0.15}\text{NiO}_2$  films

(b) Four probe resistivity measurements on  $\text{Nd}_{0.85}\text{Sr}_{0.15}\text{NiO}_2$  films (enlarged to show sign of resistivity drop)

subsequent reduction aimed at obtaining the infinite layer phase and aligning with the requisite properties outlined in the existing literature. As a next step to realize infinite layer phase, we performed reduction on  $\text{Nd}_{0.85}\text{Sr}_{0.15}\text{NiO}_3$  films in vacuum-sealed quartz tubes using  $\text{CaH}_2$ . After extensive efforts and fine-tuning of reduction parameters, our research team effectively synthesized the infinite layer compound by reducing 12nm thick  $\text{Nd}_{0.85}\text{Sr}_{0.15}\text{NiO}_3$  perovskite film with 0.1g  $\text{CaH}_2$  powder at  $300^\circ\text{C}$  for 3hrs. XRD pattern for reduced film is shown in figure 3.3 (unreduced film on the top and reduced at the bottom). Presence of first and second order diffraction peaks at  $2\theta = 26^\circ$  and  $2\theta = 55^\circ$  respectively corresponding to an out-of-plane lattice parameter of  $3.38\text{\AA}$ , confirms the infinite layer phase and the XRD pattern well matches with pattern reported in the literature for infinite layer nickelate films [51].

Four-probe electrical resistivity measurements shown in figure 3.4a demonstrated a good metallic behavior till down to very low temperature for  $\text{Nd}_{0.85}\text{Sr}_{0.15}\text{NiO}_3$  in agreement with reported behavior in literature [68], [54], [55], [112]. The infinite layer phase exhibited metallic behavior with drop in resistivity near 10K, although complete zero resistivity was not reached, as illustrated in figure 3.4b. This observation presented a nuanced situation, as we cannot definitively ascertain the absence of superconductivity in our film while simultaneously noting that resistivity does not vanish. This scenario encouraged us to consider the possibility that a non-superconducting factor

might be contributing to the measurements from the specific region of the film under investigation. To test this, subsequent resistivity measurements conducted at distinct location on the infinite layer film. Surprisingly, the sample showed a distinct resistivity behavior compared to the previous results shown in figure 3.4b. Notably, when four-probe contacts were established at the same points, the resistivity behavior showed reproducibility. However, similar four-probe measurements carried out at different positions across the film's area unveiled diverse resistivity behaviors. This finding suggests the presence of inhomogeneous resistivity characteristics across the film, implying potential phase inhomogeneity within the nickelate sample. This phenomenon could potentially originate from multiple factors, encompassing the inherent inhomogeneity introduced during the PLD synthesis process, subsequent reduction steps, or even strain induced by the substrate.

Motivated by this intriguing finding, we opted to conduct a more comprehensive investigation into the issue of inhomogeneity. This aspect assumed a central role in my research objectives and became a focal point of my study within the thin film segment of my thesis. In addition, the utilization of  $\text{CaH}_2$ -based reduction has demonstrated its efficacy in stabilizing phases within nickelates that are otherwise difficult to achieve. However, the existing literature lacks a systematic approach to address the practical challenges inherent in the synthesis procedure this reduced phase. Hence, the core objective of my research was to explore into the  $\text{CaH}_2$ -based reduction process of nickelate thin films, aiming at providing a more comprehensive understanding of these crucial aspects.

### 3.3 PLD synthesis of perovskite $\text{Pr}_{0.8}\text{Sr}_{0.2}\text{NiO}_3$ on $\text{SrTiO}_3$ (STO) substrate

My first objective was to optimize growth parameter for perovskite  $\text{Pr}_{1-x}\text{Sr}_x\text{NiO}_3$  thin films using PLD. These films serve as parent compound for infinite layer  $\text{Pr}_{1-x}\text{Sr}_x\text{NiO}_2$  ( $0.12 \leq x \leq 0.24$ ) films that are reported to be superconducting [56], [57]. I started with composition  $\text{Pr}_{0.8}\text{Sr}_{0.2}\text{NiO}_3$  and optimized primary parameters for the deposition on STO (001) substrate. The presence of relatively unstable nickel valency states such as  $\text{Ni}^{3+}$  in  $\text{Pr}_{1-x}\text{Sr}_x\text{NiO}_3$  films poses challenges for stabilizing the pure perovskite phase through pulsed laser deposition (PLD). Moreover, adapting the substrate to minimize lattice mismatch with the infinite-layer phase (bringing it down to -0.4%)

[85] results in significant tensile strain (+2.6% with SrTiO<sub>3</sub> (001)) [8] on the perovskite nickelate film, posing further difficulties to stabilize perovskite phase.

Primary PLD parameters considered for tuning are:

1. Laser energy density: By varying the laser energy density, the ablation rate and kinetic energy of the ablated species can be adjusted. This parameter affects the film deposition rate, crystallinity, and surface morphology. Finding the optimal energy density ensures controlled growth without damaging the film.
2. Substrate temperature: Altering the substrate temperature during deposition influences the adhesion, crystallinity, and phase formation of the thin film. By selecting the appropriate temperature, researchers can optimize film growth and control the properties of the deposited material.
3. Growth pressure and background gases: Modulating the growth pressure and introducing specific background gases can affect the chemical composition, stoichiometry, and structure of the thin film. These parameters play a critical role in controlling the reaction kinetics during deposition.
4. Pulse repetition rate: Changing the repetition rate of the laser pulses modifies the frequency at which the target material is ablated. Adjusting this parameter allows for control over the deposition rate and can influence film properties such as thickness and crystallinity.
5. Target-substrate distance: Adjusting the distance between the target and the substrate affects the deposition rate and plume dynamics. Finding the optimal distance ensures uniform film thickness and minimizes any potential shadowing effects.
6. Target composition and stoichiometry: The composition and stoichiometry of the target material have a direct impact on the chemical composition and properties of the deposited film. Precise control of the target composition ensures the desired film properties are achieved.

Idea is to tune these parameters systematically within a specific range, which can establish a growth window where the thin film exhibits the desired characteristics.

Stoichiometric Pr<sub>0.8</sub>Sr<sub>0.15</sub>NiO<sub>3</sub> PLD targets are synthesized by following these steps: First, a stoichiometric mixture of Pr<sub>6</sub>O<sub>11</sub> (Alfa Aesar, 99.5%), SrCO<sub>3</sub> (Alfa Aesar, 99%), NiO (Cerac,

99%) powders is grinded with the help of ball milling. Next this mixture is heated to 1000°C for 3 hours with a heating and cooling rate of 150°C per hour. After cooling, Rhodoviol (Polyvinyl Alcohol) is added and mixed to form a paste and let it dry. Finally, the powder is pressed to 30mm pellets and the pellet is sintered on Pt metal at 1400°C for 4 hours with a slow ramp rate of 150°C/hour for both heating and cooling.

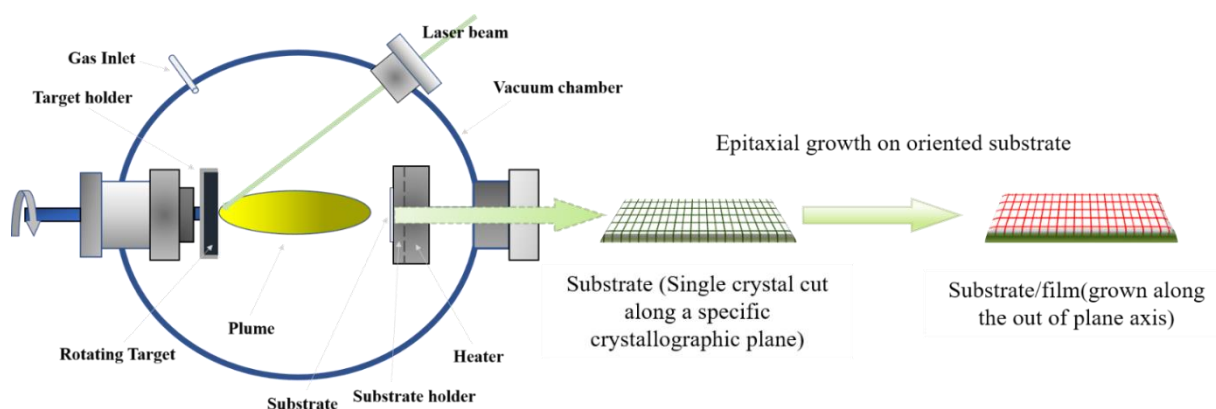


Figure 3.5: Schematic of Pulsed laser deposition process

Figure 3.6 shows thin film XRD pattern of thin film deposited with different substrate temperature. Perovskite  $\text{Pr}_{0.8}\text{Sr}_{0.2}\text{NiO}_3$  films on STO (001) substrates are identified by (002) peak close to  $2\theta = 48^\circ$  and presence of (001) peak in the thin film x-ray diffraction pattern. From the previous knowledge of PLD growth of nickelates carried in our PLD system, we had a good grasp on the growth window  $\text{Pr}_{0.8}\text{Sr}_{0.2}\text{NiO}_3$  films. This allowed us to fix laser-operating condition to output energy of 200mJ with a repetition rate of 2Hz, and target and substrate to keep at distance of 5cm. In order to determine the ideal deposition temperature and pressure, a fixed deposition temperature of 700°C is chosen, and the XRD patterns of thin films deposited at varying oxygen pressures are compared. The thin film XRD results presented in Figure 3.6a reveal that oxygen partial pressures 0.1mbar is ideal as a deposition pressure lower than 0.1 mbar led to formation of undesired phases within the film. This is evident from the presence of a peak near  $2\theta = 29^\circ$  for the film deposited at 0.01mbar.

Additionally, to identify the optimal substrate temperature for obtaining perovskite  $\text{Pr}_{0.8}\text{Sr}_{0.2}\text{NiO}_3$ , depositions are conducted at different temperatures while maintaining a deposition pressure of 0.1mbar, which was determined as optimal in previous depositions. Figure 3.6b provides a comparison between thin films deposited at 600°C and 700°C. The presence of a (001)

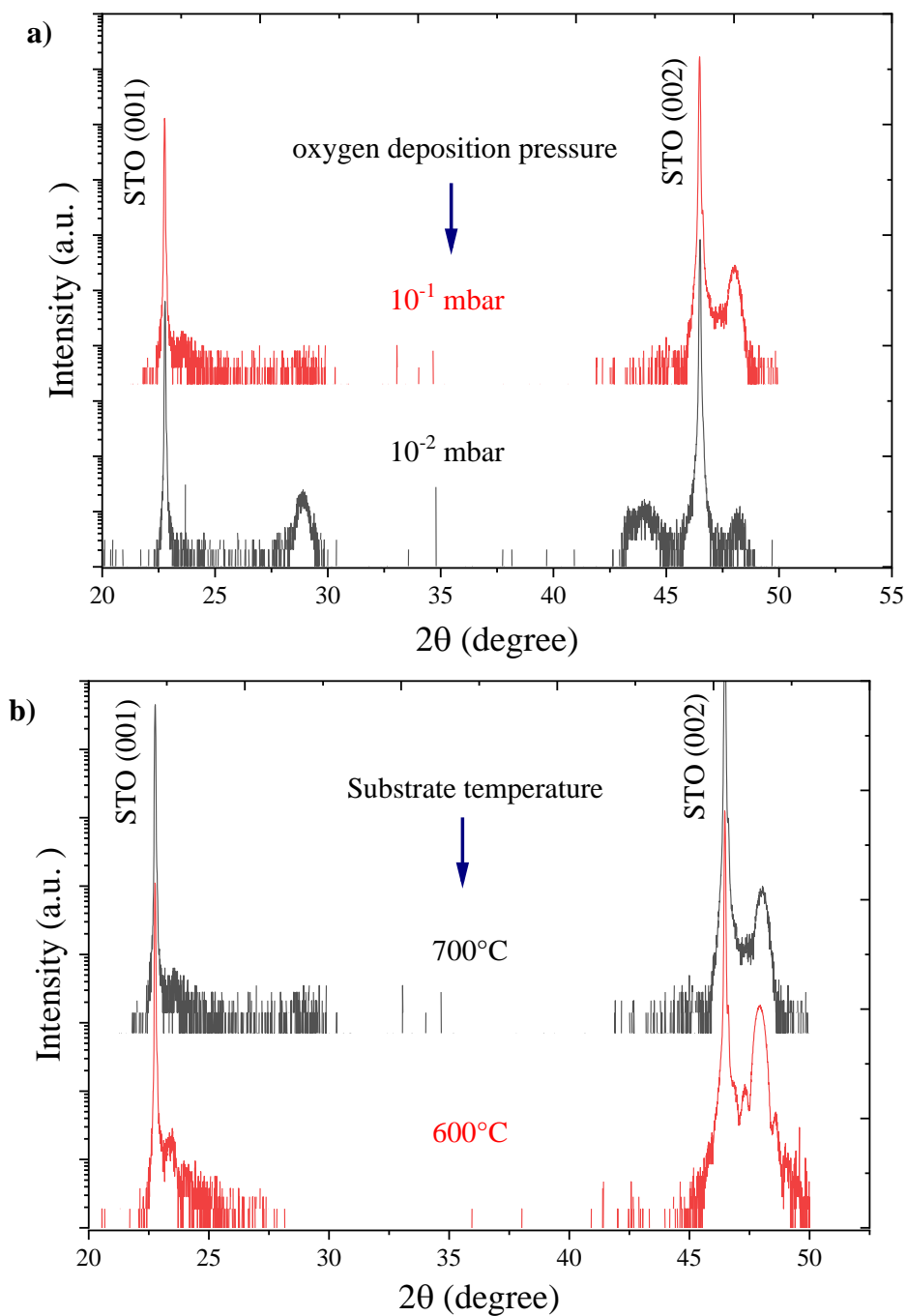


Figure 3.6: Thin film XRD pattern for  $\text{Pr}_{0.8}\text{Sr}_{0.2}\text{NiO}_3$  films

a) Deposited at different oxygen pressure at temperature  $700^\circ\text{C}$ .

b) Deposited at different temperature with oxygen pressure 0.1 mbar

diffraction peak and the appearance of Laue fringes alongside the film peak indicate that the thin film deposited at  $600^\circ\text{C}$  exhibits superior quality [56], [57]. Therefore,  $600^\circ\text{C}$  is identified as the

optimal temperature for the growth of  $\text{Pr}_{0.8}\text{Sr}_{0.2}\text{NiO}_3$  films on STO substrates.

In the context of nickelate PLD growth, there can be preferential ablation of ions from the target, which is a selective removal of certain elements or ions from the target material at different rates leading to a non-stoichiometric plume. The preferential ablation of ions can result in a non-stoichiometric plume composition, where the relative concentrations of different elements in the plume may deviate from the desired stoichiometry. This can influence the composition and properties of the deposited thin film [51]. To account for this problem our target surfaces were often polished and resurfaced.

To improve film quality, pre-annealing substrate in vacuum at an elevated temperature is a commonly employed technique in epitaxial thin film growth on STO substrates. During pre-annealing in vacuum, the elevated temperature promotes the migration and diffusion of atoms on the substrate surface. This thermal energy allows the surface atoms to find their most stable positions and form a reconstructed surface with minimized surface energy. As a result, any surface defects, impurities, or contaminants present on the initial substrate surface are effectively eliminated [160]–[163]. Post-annealing, also known as annealing or thermal treatment after thin film deposition is performed in oxygen ambient to regulate oxygen content in the film thereby improving phase purity and crystallinity of the deposited thin film. The substrate acts as a template, affecting crystalline orientation of the epitaxial growth, controlled annealing the film after deposition in a certain oxygen pressure could further help to align the film with the substrate's crystallographic arrangement, enhancing epitaxial growth quality [164]–[166]. Figure 3.7 shows XRD pattern comparison of pre and post annealed depositions. Series of depositions are performed to find suitable conditions. Comparing XRD pattern at different annealing conditions in figure 3.7, it is evident that the pre-annealing effect on crystallinity becomes redundant when combining post-annealing and pre-annealing processes. Although our efforts have resulted in improved film quality, we cannot conclusively state that our film exhibits a purely perovskite nature. Despite the

presence of the first-order (001) diffraction peak, the possibility of coexistence with RP type secondary phases exists, which has been reported in the literature [51].

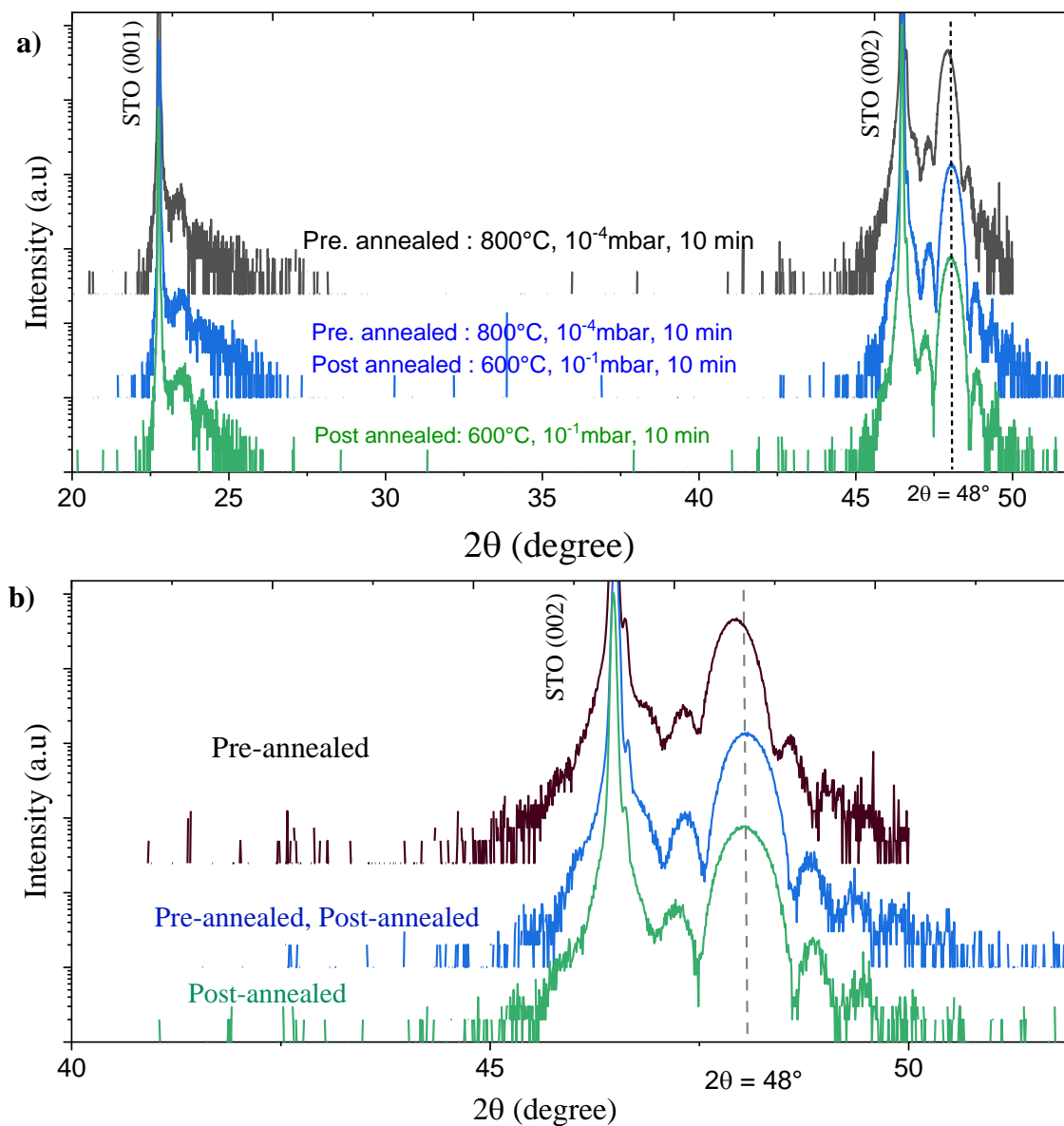


Figure 3.7:

- a) Thin film XRD pattern for  $Pr_{0.8}Sr_{0.2}NiO_3$  films went through different annealing conditions.
- b) Enlarged view of (002) peak. Dashed line indicates  $2\theta = 48^\circ$

The evaluation of deposited film quality can be extended through resistivity measurements, especially considering that perovskite  $\text{Pr}_{0.8}\text{Sr}_{0.2}\text{NiO}_3$  films exhibit metallic behavior down to lower temperatures. Any deviation from this behavior could signal the presence of undesirable phases [56]. As depicted in Figure 3.8, four-probe resistivity measurements on films subjected to various annealing conditions. Notably, films deposited without subsequent annealing displayed a deviation from metallic behavior below 50K, with small upturn in resistivity. Conversely, post-annealing led to a notable improvement in the metallic behavior of the films, extending to lower temperatures. Which further confirms post annealing film after deposition helps to stabilize perovskite phase for  $\text{Pr}_{0.8}\text{Sr}_{0.2}\text{NiO}_3$  films.

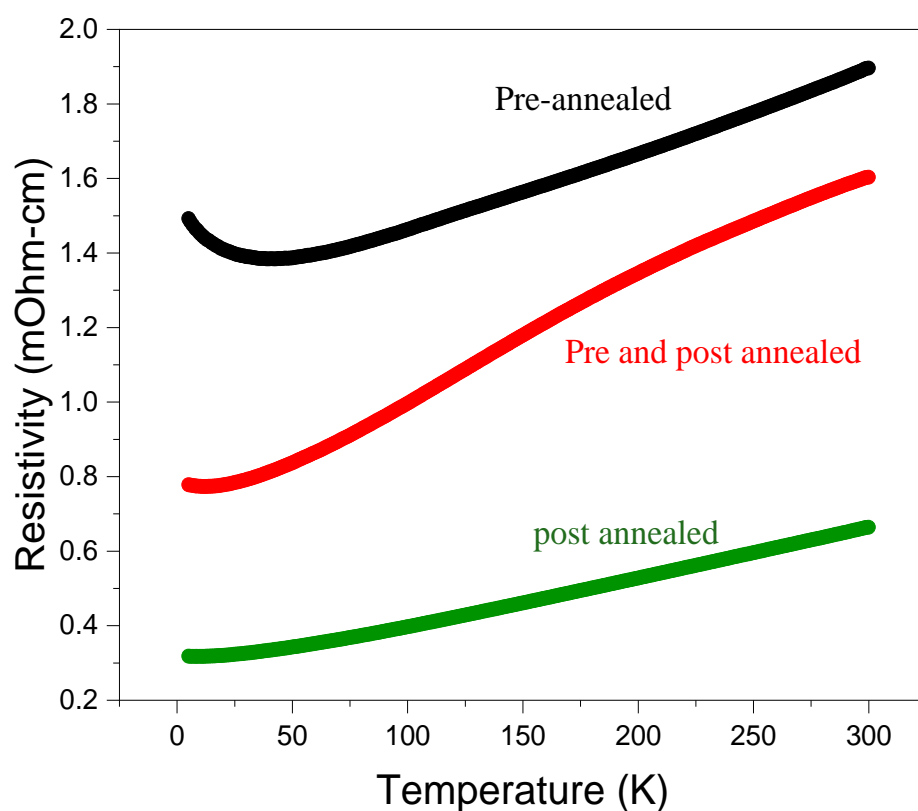
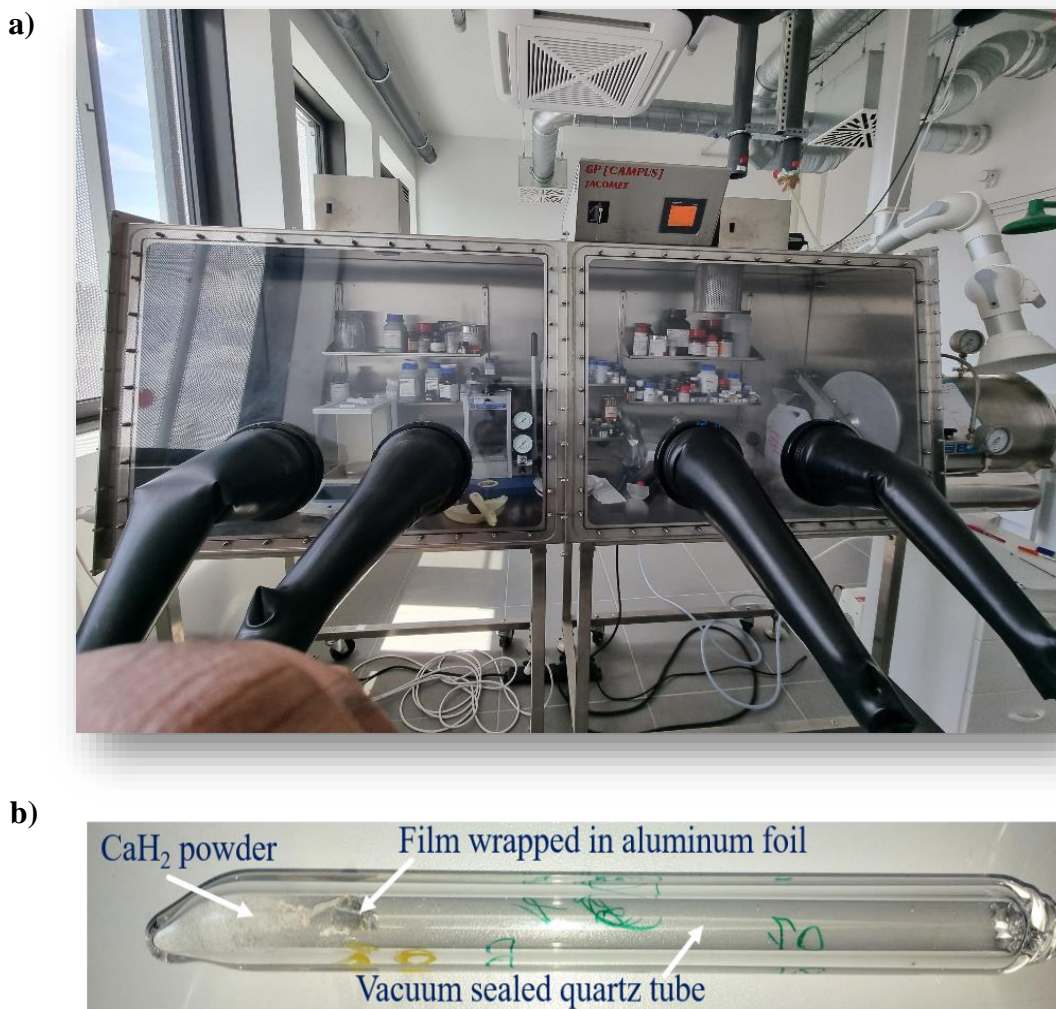


Figure 3.8: Four probe electrical resistivity measurement on films corresponding to films with diffraction pattern shown in figure 3.7

Having obtained films exhibiting perovskite phases, our focus now shifts to exploring the behavior of these films under  $\text{CaH}_2$ -based topotactic reduction. The objective is to investigate the feasibility of stabilizing the infinite layer phase from the perovskite phase through reduction process.

### 3.4 Reduction of $\text{Pr}_{0.8}\text{Sr}_{0.2}\text{NiO}_3$ on $\text{SrTiO}_3$ (STO) substrate

By leveraging our expertise in vacuum-sealed tube reactions, we were able to implement Li et. al's reduction method for the synthesis. Glove box provide us inert atmosphere for handling  $\text{CaH}_2$ , as it is a reactive compound that can undergo chemical reactions with atmospheric moisture or oxygen.



**Figure 3.9:**

a) Glove box setup in CRISMAT laboratory.

b) Vacuum sealed quartz tube containing thin film sample as well as  $\text{CaH}_2$  powder

Figure 3.10 shows XRD patterns from the series of reduction experiments on four distinct thin films, all of which initially displayed identical XRD peaks. It is worthwhile to mention here that we were able to reproduce films using optimized PLD parameters as evident from their identical XRD peaks. Following the deposition process, the as-grown  $\text{Pr}_{0.8}\text{Sr}_{0.2}\text{NiO}_3$  films were wrapped in aluminum foil, with approximately 0.1g of  $\text{CaH}_2$  powder placed inside a vacuum-sealed (pressure < 0.1mTorr) Pyrex glass tube of an inner and outer diameter of 9mm and 15mm respectively and an approximate length of 15cm. Thin film samples used for reduction are either dimensions of 5mm x 5mm or 5mm x 2.5mm and the film thickness of 10-20nm. This tube was then heated to a certain temperature and maintained at this temperature for a specific duration of time. The main objective was to determine an appropriate temperature range ( $T_R$ ) at which films can stabilize the infinite layer phase. Additionally, it aimed at identifying the optimal duration ( $t_R$ ) for which the films should be maintained at this temperature with minimal film degradation and achieving a complete transformation into the infinite layer phase.

In Figure 3.10a, the XRD patterns of the first film before and after reduction at 280°C for 4 hours are presented. Following the reduction, the XRD pattern exhibited the absence of the thin film peak. This observation indicates that while the reduction process influenced the film, it did not culminate in a phase transformation; instead, it led to film degradation. Subsequently, the second film underwent reduction at 260°C for four hours. As illustrated in Figure 3.10b, the XRD pattern revealed a subtle shift towards the higher angle side. This minute change suggested a minor decrease in the lattice parameter, implying some structural alteration. Although not conclusively signaling an infinite layer phase, this shift serves as evidence that the reduction process was exerting an influence on the film. Reduction on the third film involved a shorter period of 2 hours at 260°C. The corresponding XRD pattern (Figure 3.10c) displayed a reduction in peak intensity without a significant shift in position. This observation indicates that the reduction process might not be inducing substantial structural changes. Consequently, this outcome underscores the necessity for further optimization. Transitioning to the fourth film, reduction was carried out for 2 hours at 280°C. The resulting XRD pattern (Figure 3.10d) displayed a slight shift towards the higher angle side, accompanied by a decrease in peak intensity. Although this shift was not substantial enough to confirm a phase transformation, it did verify that the reduction process was indeed impacting the film's structure. From this series of reduction attempts, a significant insight was collected: for  $\text{Pr}_{0.8}\text{Sr}_{0.2}\text{NiO}_3$  films with a thickness ranging from 10-20nm, the optimal

reduction conditions appear to be within the temperature range of 260-280°C. Temperatures above this range led to complete film degradation, while temperatures below yielded no noticeable reduction.

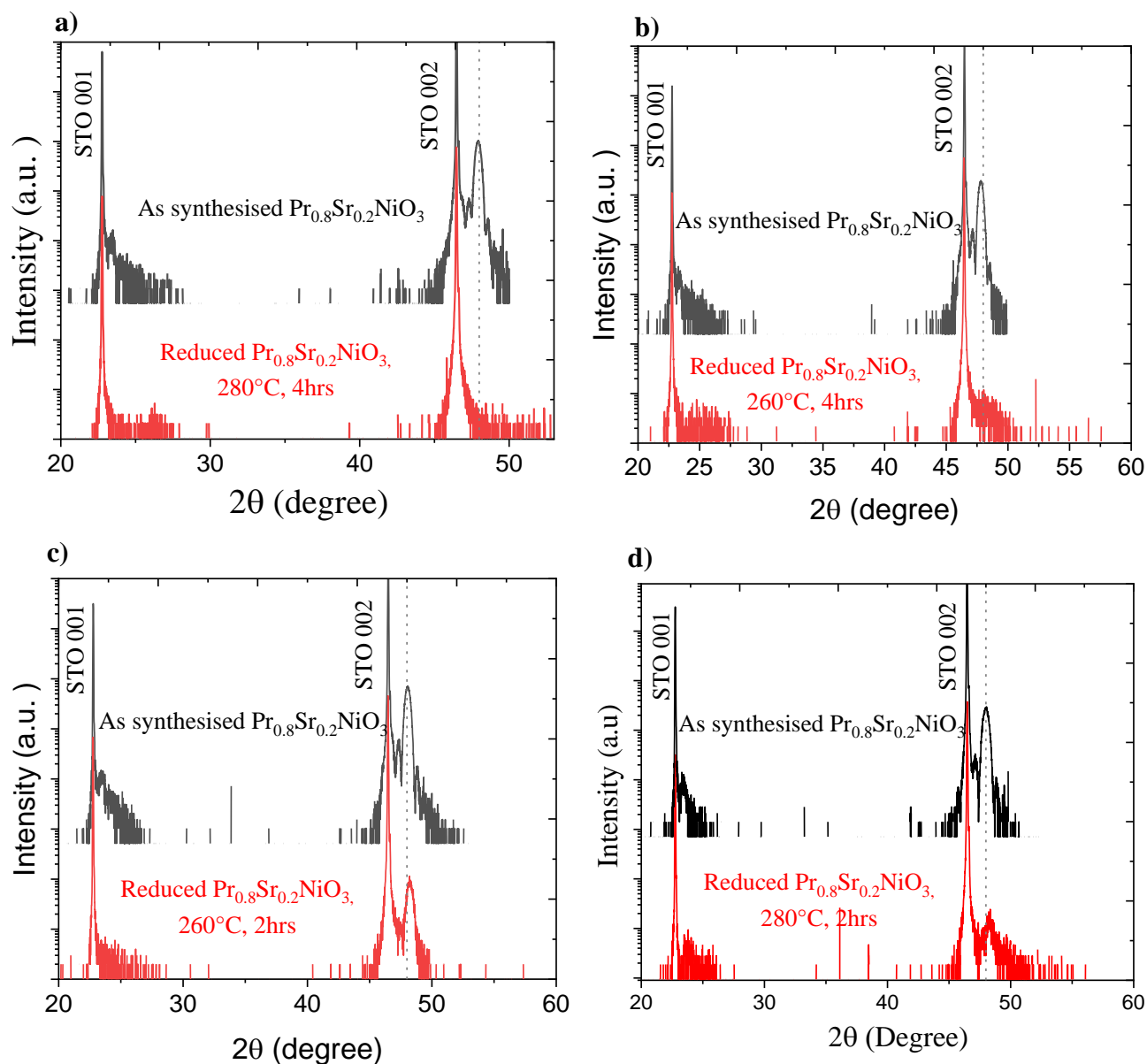


Figure 3.10:

Figure shows thin film XRD patterns before and after reduction on  $\text{Pr}_{0.8}\text{Sr}_{0.2}\text{NiO}_3$  films. Dashed line indicates  $2\theta = 48^\circ$

An additional reduction was performed on the fourth film sample, which had already undergone partial reduction. The XRD of the film recorded after additional reduction performed for 40 minutes on the sample that previously reduced for 2hrs at 280°C is shown in Figure 3.11. The objective was to determine whether a shorter duration of additional reduction could potentially lead to the stabilization of the infinite layer phase in the film. However, the XRD pattern after this reduction exhibited the absence of any crystalline peak, with the exception of the substrate peak. This observation strongly indicates the complete degradation of the film upon short time reduction on a partially reduced film, as evidenced by the lack of discernible film-related peaks in the pattern after second reduction.

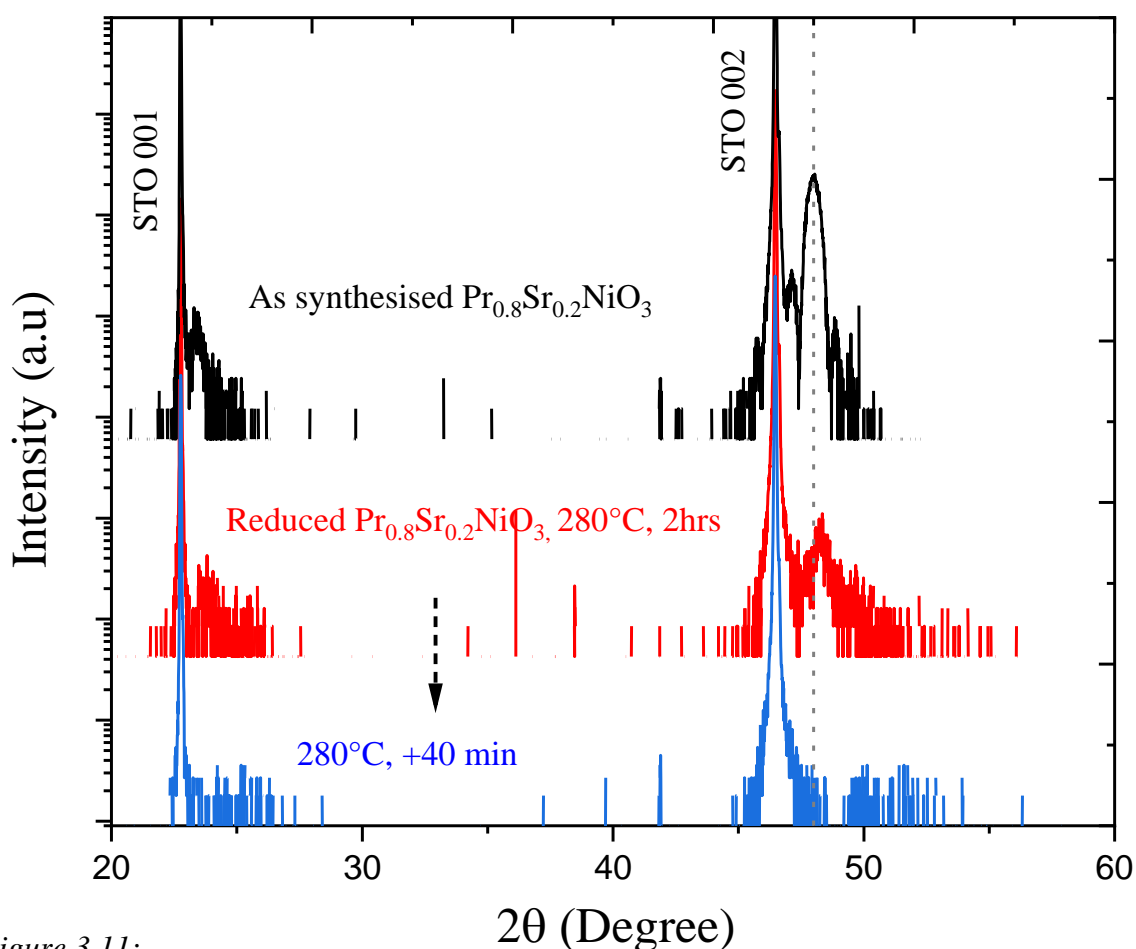


Figure 3.11:

Figure shows thin film XRD patterns before and after consecutive reductions on  $\text{Pr}_{0.8}\text{Sr}_{0.2}\text{NiO}_3$  films. Dashed line indicates  $2\theta=48^\circ$

Four-probe resistivity measurements were conducted on the fourth film after an additional 40-minute reduction. The measurements demonstrated insulating behavior as demonstrated by the resistivity vs temperature plot shown in figure 3.12. Prior research from our group by Dr. NASR had revealed inconsistent resistivity behaviour in the infinite layer material  $\text{Nd}_{0.85}\text{Sr}_{0.15}\text{NiO}_2$  when measuring resistivity across various regions of the reduced sample.

Inspired by these findings, I carried out resistivity measurements at multiple locations within the thin film to assess the uniformity of the reduction process. Intriguingly, the reduced sample displayed inhomogeneous resistivity behaviour (figure 3.12). The prevailing evidence suggests that this inhomogeneity arises from the reduction process rather than being associated with the infinite layer phase. This conclusion is substantiated by the fact that even in the absence of a complete transition to the infinite layer phase, the observed resistivity variation remains heterogeneous across the sample.

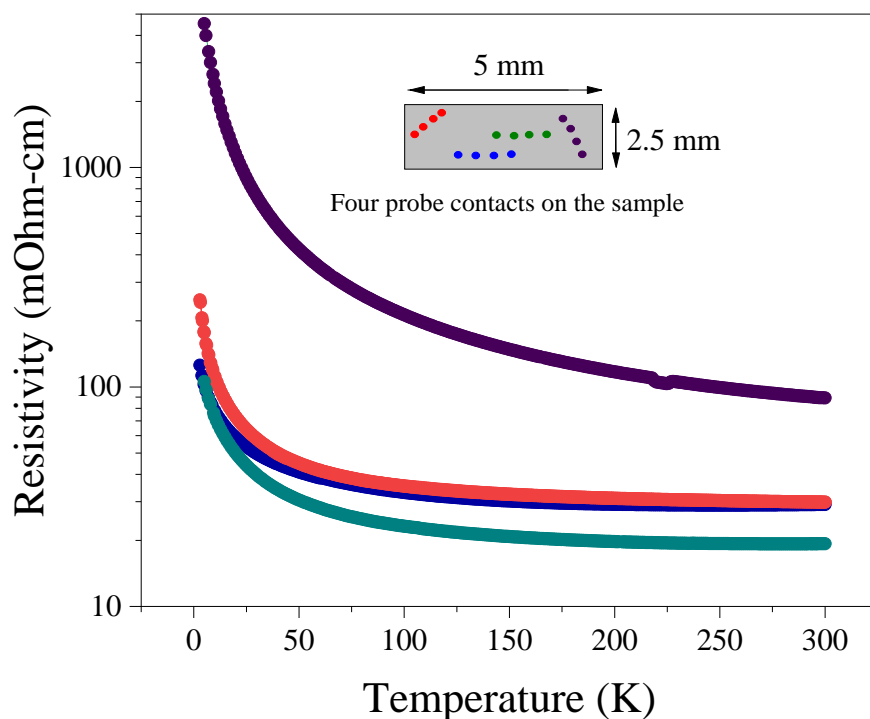


Figure 3.12: Electrical resistivity measurements corresponding to XRD pattern in blue color in figure 3.11. Inset shows four probe contacts on the sample. Matched with color code of the resistivity plot.

To gain deeper insights into the reduction process, we embarked on a detailed investigation by subjecting a single film to successive shorter reduction cycles. The objective was to identify if there is any intermediate temperature at which the film undergoes reduction without a substantial loss of crystallinity. Building on the findings presented in figure 3.11, where we observed the impact of a short additional reduction, we opted to initiate the reduction at 260°C. The results of this series of reductions are illustrated in the thin film XRD patterns featured in figure 3.13.

A noteworthy observation was the shift in the XRD peak towards higher angles, a clear indicator of the reduction-induced decrease in the lattice parameter of the film. This shift signifies notable structural modifications occurring within the film. Additionally, a decrease in the intensity (area) of the film peak was apparent, signalling a reduction in the amount of crystalline material present. Moreover, the peak exhibited broadening, indicative of decreased crystallinity. While it's crucial to emphasize that our film did not undergo a full transformation into the desired infinite layer phase, it is pertinent to recognize that the reduction process does bring about distinct effects. The inset in figure 3.13b provides a visual representation of the intensity evolution of the peak, alongside the corresponding lattice parameter calculated from the peak's position for each reduction cycle. This representation succinctly illustrates the changes observed throughout the reduction process. Starting from an initial lattice parameter of around 3.79Å for the unreduced film, a gradual decrease is observed with each subsequent reduction cycle. It is important to note that the complete transformation into the infinite layer phase would manifest in an XRD pattern with the first-order peak close to  $2\theta=26^\circ$  and the second-order peak close to  $2\theta=55^\circ$ , aligning with a lattice parameter of approximately 3.38Å. In our case, film peak shifted to an angle ranging between 48 and 49, signifying significant progress yet still distant from the target  $2\theta=55^\circ$ . This discrepancy underscores the complexity of achieving a comprehensive transformation to the infinite layer phase.

In light of these findings, it becomes evident that the reduction process indeed introduces changes in the lattice parameter and the characteristics of the XRD peak. These changes point to structural modifications within the film's crystal lattice, directly attributed to the CaH<sub>2</sub>-based reduction. Nevertheless, the realization of the ultimate goal of complete transformation into the infinite layer phase through controlled reduction remains a challenging endeavour.

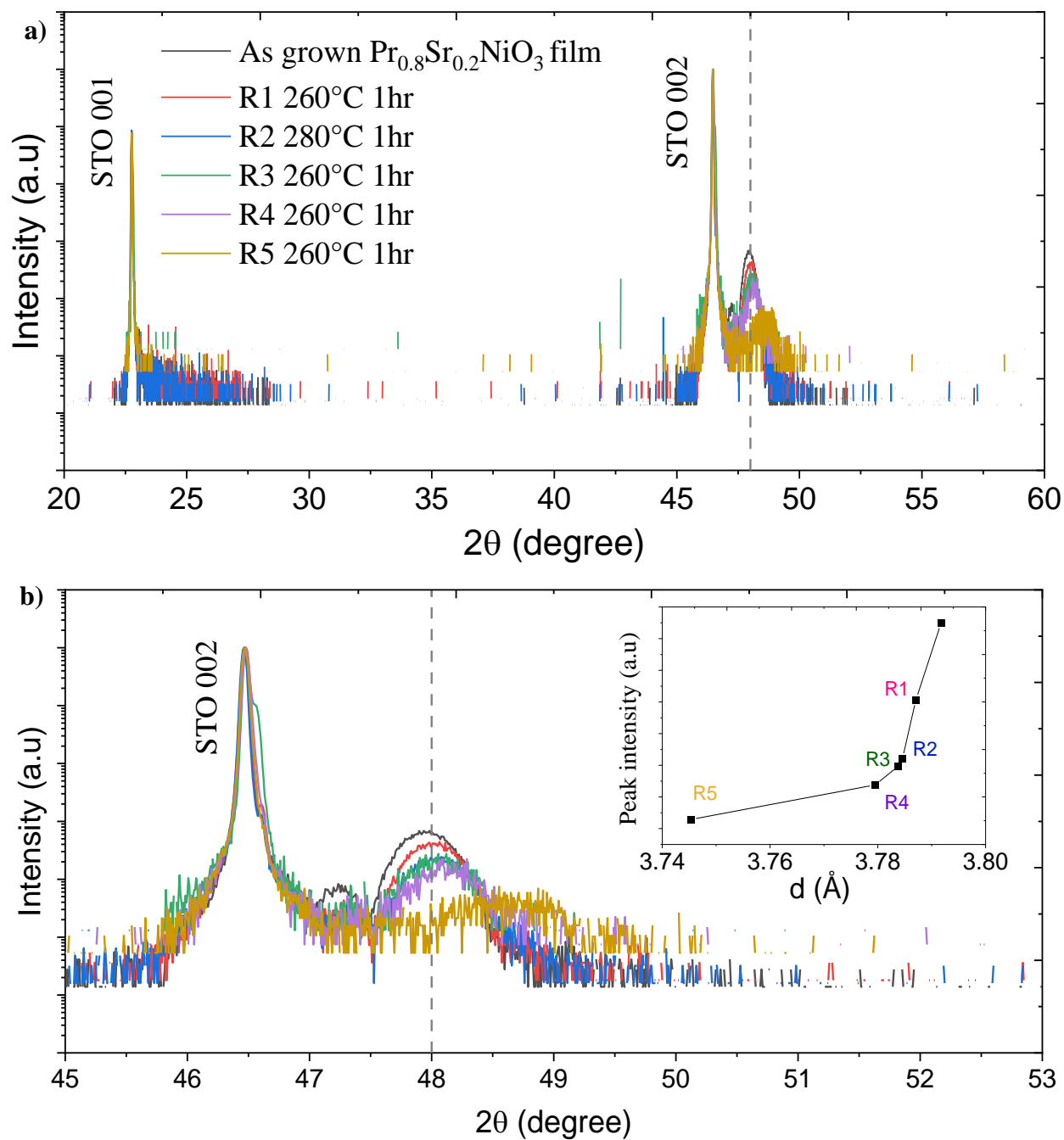


Figure 3.13:

- Evolution of thin film XRD pattern upon series of reduction performed.
- Enlarged view focused on Second order diffraction peaks. Inset shows corresponding change in the out of plane lattice parameter vs peak intensity upon each reduction.

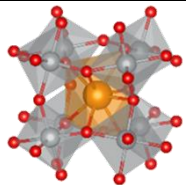
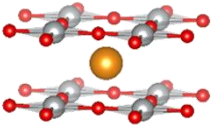
Another crucial aspect to consider is that films with no sign of first-order diffraction peak, yet displaying a second-order peak close to  $2\theta = 48$  degrees, but shifted towards the lower angle, could potentially be more of non-perovskite RP-like phases. Difficulty in reduction could stem from the presence of distinct phases that react differently to the reduction. It is plausible that the variations observed in the reduction results can be attributed to either an unsuccessful reduction or the possibility that seemingly identical thin films, despite displaying similar peak patterns, may possess differing quantities of non-perovskite phases. This underlines the complexity of the reduction process and its interaction with the film's composition, crystalline structure, and various phases present.

Considering the impact of lattice constant mismatch on the stabilization of the perovskite phase during PLD and subsequent reduction for infinite layer phase formation, we turned our attention to a substrate with a different lattice constant compared to  $\text{SrTiO}_3$ . This variable strain could potentially play a crucial role in both the PLD stabilization of the perovskite phase and the subsequent reduction process for achieving the infinite layer phase. In the following section, we discuss PLD synthesis and reduction of  $\text{Pr}_{0.8}\text{Sr}_{0.2}\text{NiO}_3$  on a different substrate.

### 3.5 PLD synthesis and reduction of $\text{Pr}_{0.8}\text{Sr}_{0.2}\text{NiO}_3$ on LSAT substrate

Despite being able to observe reduction, we could not succeed in transformation of perovskite to infinite layer on the  $\text{Pr}_{0.8}\text{Sr}_{0.2}\text{NiO}_3$  films deposited on STO substrate. We decided to change substrate to  $(\text{LaAlO}_3)_{0.3}(\text{Sr}_2\text{TaAlO}_6)_{0.7}$  (LSAT). The LSAT substrate is anticipated to induce a lower in-plane tensile strain on perovskite  $\text{Pr}_{0.8}\text{Sr}_{0.2}\text{NiO}_3$  compared to the strain caused by STO. This is attributed to LSAT having a smaller lattice constant of 3.869 Å, in contrast to the lattice constant of STO which is 3.905 Å [167]. Consequently, this may facilitate the stabilization of the perovskite  $\text{Pr}_{0.8}\text{Sr}_{0.2}\text{NiO}_3$  phase on LSAT, potentially reducing the occurrence of RP-type defects. However, it is important to note that the infinite layer phase has a larger lattice constant than both LSAT and STO, resulting in LSAT applying a relatively higher compressive strain on infinite layer  $\text{Pr}_{0.8}\text{Sr}_{0.2}\text{NiO}_2$  compared to STO. For comparison epitaxial mismatch of  $\text{NdNiO}_3$  and  $\text{NdNiO}_2$  on STO and LSAT substrates are tabulated below. Moreover, LSAT substrate provides a higher chemical stability compared to STO, particularly during the reduction process [69], [116], [168].

Table 3.1: Epitaxial mismatch of  $\text{PrNiO}_3$  and  $\text{PrNiO}_2$  on  $\text{SrTiO}_3$  and LSAT substrates. Adapted from reference [170].

Phase	Mismatch on STO (3.905 Å)	Mismatch on LSAT (3.869 Å)
 Perovskite $a = 3.85 \text{ \AA}$ [169]	+1.4% (Tensile strain)	+0.6% (Tensile strain)
 Infinite-Layer $a = 3.920 \text{ \AA}$ [56]	-0.4% (Compressive strain)	-1.3% (Compressive strain)



The deposition window for  $\text{Pr}_{0.8}\text{Sr}_{0.2}\text{NiO}_3$  on LSAT (001) substrate was found to be similar to that on STO (001) substrate, with a slight adjustment required in laser energy. As depicted in Figure 3.14, optimal outcomes were achieved on the LSAT substrate at a laser energy of 150mJ, as evidenced by well-defined (001) and (002) peaks at approximately  $2\theta=48^\circ$ . Notably, the LSAT (001) substrate demanded a lower laser energy of 150mJ, in contrast to the 200mJ required on the

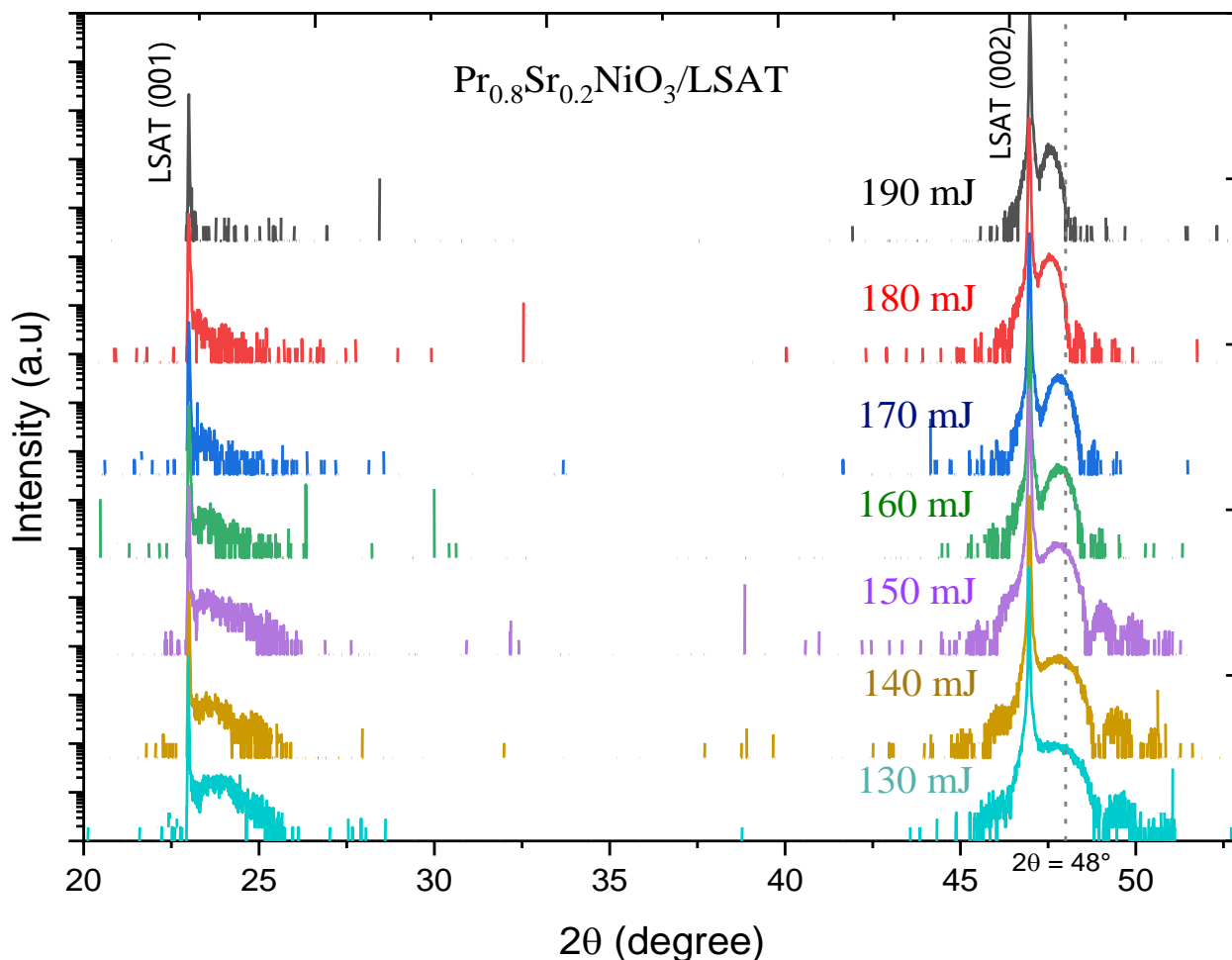


Figure 3.14: Thin film XRD pattern for  $\text{Pr}_{0.8}\text{Sr}_{0.2}\text{NiO}_3$  on LSAT substrate deposited with different laser output energy. Patterns are vertically shifted for clarity

STO (001) substrate. Additionally, the XRD data displayed the presence of Laue reflections near the film peaks, further indicating the favorable film quality on the LSAT substrate.

The LSAT substrate has demonstrated its ability to provide a superior growth environment for  $\text{Pr}_{0.8}\text{Sr}_{0.2}\text{NiO}_3$  films, resulting in enhanced crystallinity. Figure 3.15 shows reduction of the films deposited on LSAT (001) with different laser energies. For the sake of comparison, I maintained consistent reduction parameters of  $260^\circ\text{C}$  and 3 hours for all films, to observe how these films

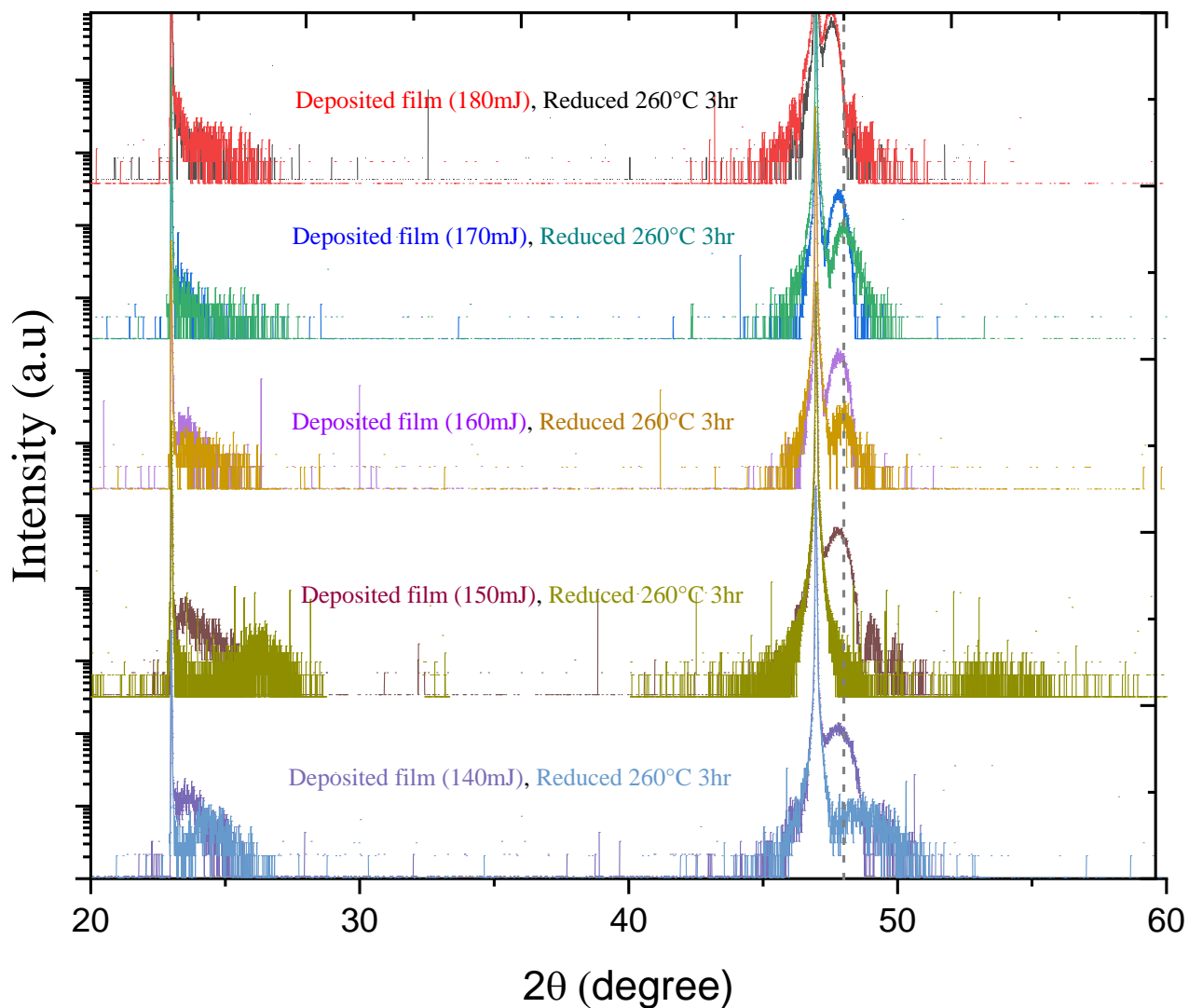
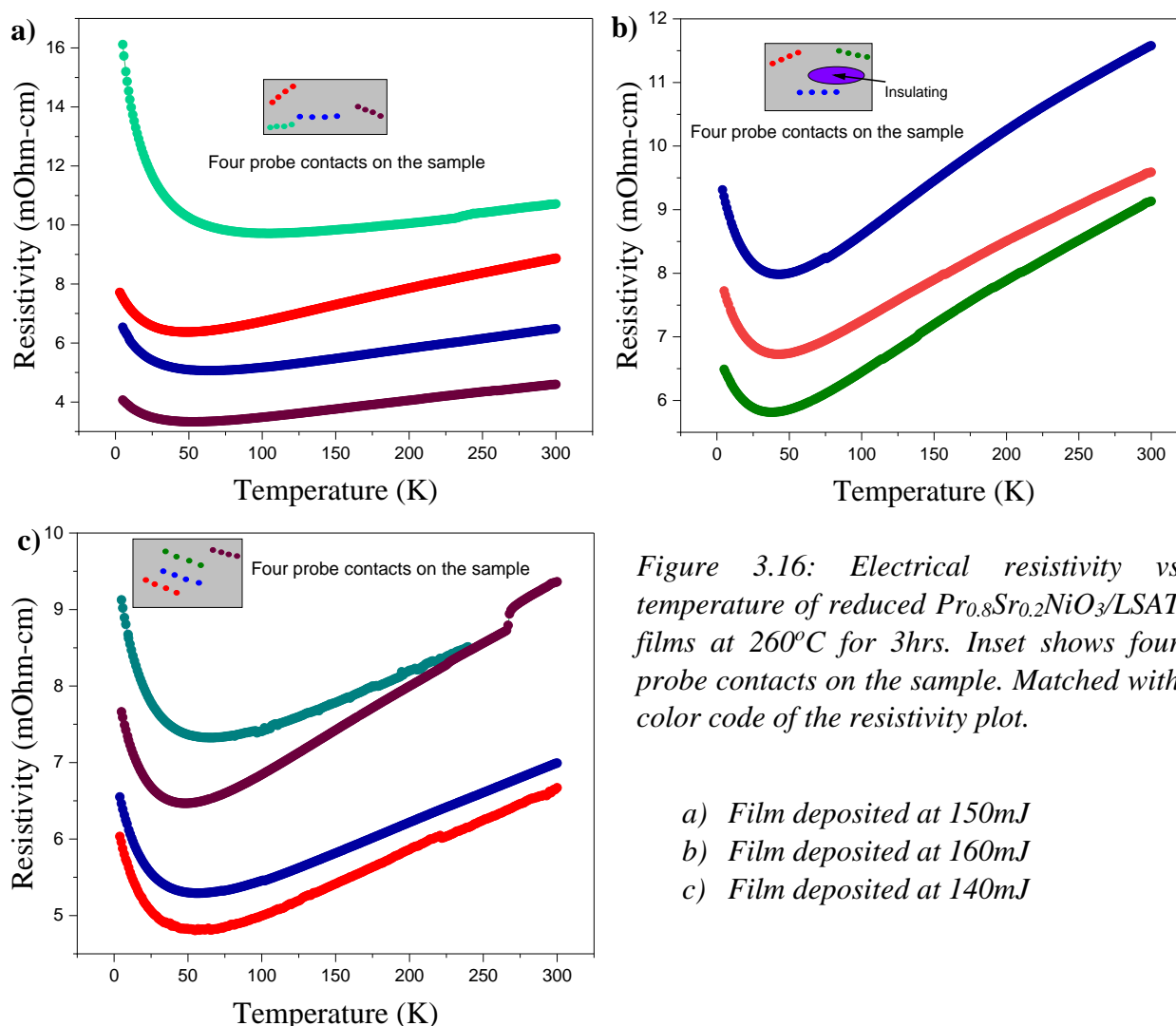


Figure 3.15: Thin film XRD patterns for as deposited and reduced  $\text{Pr}_{0.8}\text{Sr}_{0.2}\text{NiO}_3$  films on LSAT substrate deposited with different laser output energy and reduced at  $260^\circ\text{C}$  for 3hrs. Patterns are vertically shifted for clarity

respond to the reduction process. This choice of temperature and duration was informed by the reduction experiments discussed in Section 3.3. This series of reductions highlights the significant

impact of even minor variations in peak position or crystallinity on the films when subjected to similar reduction conditions. It indicates that subtle differences in the structural properties of the films can result in notable variations in their response to the reduction process. Furthermore, upon reduction of the film deposited at 150mJ, the XRD pattern reveals indications of material at diffraction angles where peaks corresponding to the infinite layer phases are expected (approximately  $26^\circ$  for the (001) peaks and  $53^\circ$ - $54^\circ$  for the (002) peak). This observation suggests that the reduction process might have succeeded in converting the perovskite phase to the infinite layer phase. However, the difficulty to achieve stable crystalline infinite layer phase formation is evident, as the transformed phase did not maintain its crystalline structure.

Resistivity measurements were carried out at various locations on the reduced samples, aiming to assess the uniformity of the reduction process. Notably, the films deposited on LSAT



*Figure 3.16: Electrical resistivity vs temperature of reduced  $Pr_{0.8}Sr_{0.2}NiO_3/LSAT$  films at  $260^\circ C$  for 3hrs. Inset shows four probe contacts on the sample. Matched with color code of the resistivity plot.*

- a) Film deposited at 150mJ*
- b) Film deposited at 160mJ*
- c) Film deposited at 140mJ*

substrates exhibited a higher degree of homogeneity upon reduction. This observation is supported by the relatively lower variation in resistivity across different regions of the sample as illustrated in figure 3.16, when compared to the results obtained from STO substrates. This suggests that while some non-uniform reduction may still occur, the overall uniformity of the reduction process is improved on LSAT substrate. At this point, we decided to go for Transmission Electron Microscopy (TEM) studies on our films to further understand the uniformity and phase.

### 3.6 TEM on nickelate thin films

We have performed energy-dispersive x-ray spectroscopy (EDS) mapping to investigate the elemental composition and distribution of the films. EDS was performed in CRISMAT lab by Denis PELLOQUIN on as grown, unreduced  $\text{Pr}_{0.8}\text{Sr}_{0.2}\text{NiO}_3$  films on LSAT deposited at 190mJ (figure 3.14). The EDS mapping results signals that all the expected elements (Pr, Sr, Ni) are present uniformly throughout the film with no sign of diffusion to the substrate as shown in Figure 3.17a. In addition, Sr is observed in both film and substrate as expected and the difference in its concentration is manifested as color contrast in EDS map. Furthermore, figure 3.17b shows Elemental concentration profile across selected area of cross section, which includes substrate, film and carbon coating. A stable oxygen profile is observed throughout substrate and film as expected for the unreduced film.

Subsequently, we conducted High Resolution TEM (HRTEM) analysis of the same film. HRTEM was performed by Philippe BOULLAY in CRISMAT lab. This particular film was expected to reveal a mix of perovskite and non-perovskite (RP-type) phases. The expectation was based on the absence of a well-defined (001) diffraction peak and the positioning of (002) at a lower angle than anticipated for perovskite, as observed in the XRD image (Figure 3.14, film marked as 190mJ). Figure 3.18a shows cross section TEM images of this film, which shows many defects.

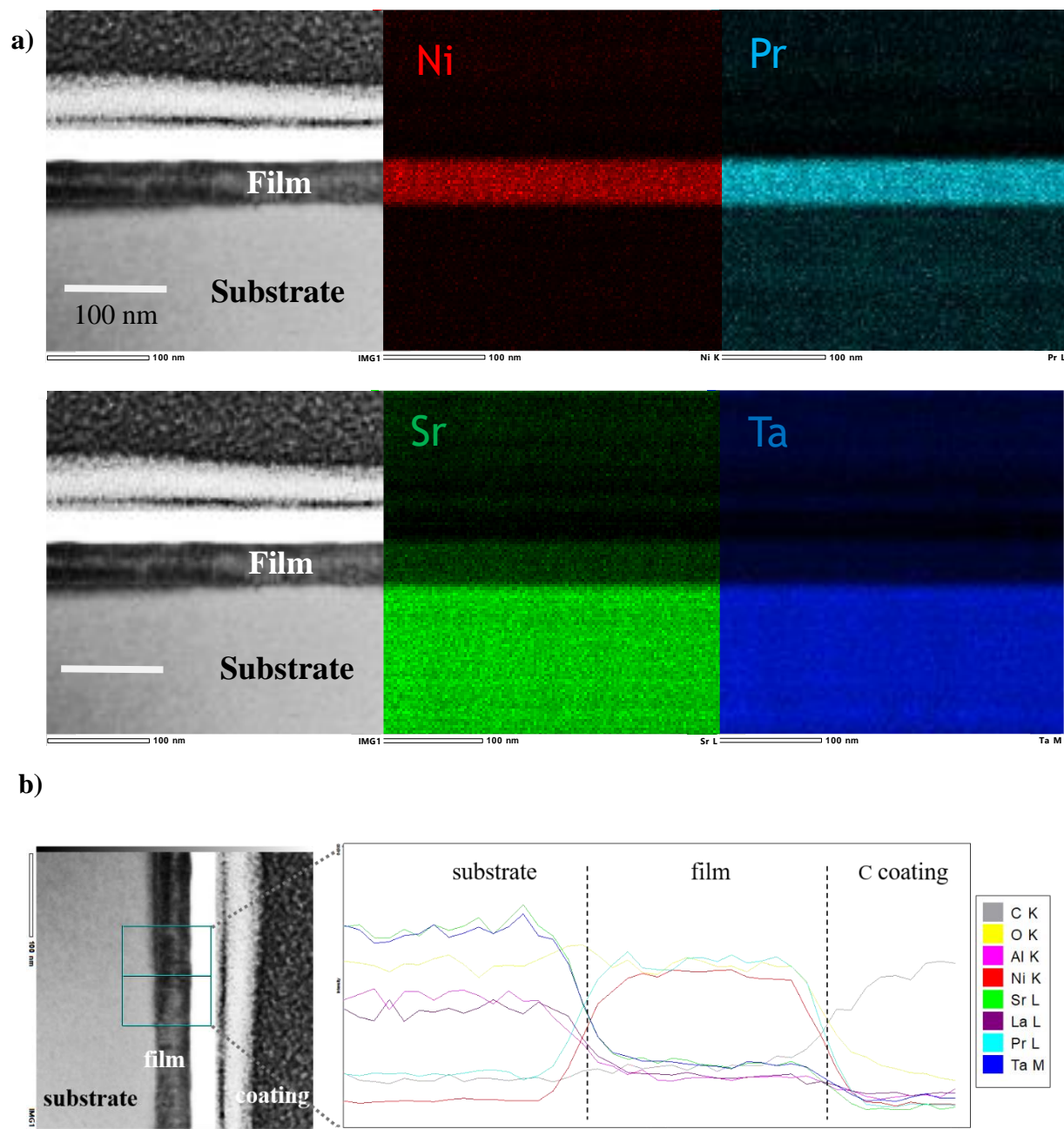


Figure 3.17:

a) Figure EDS mapping of  $\text{Pr}_{0.8}\text{Sr}_{0.2}\text{NiO}$  film on LSAT.

b) Elemental concentration profile across selected area of cross section

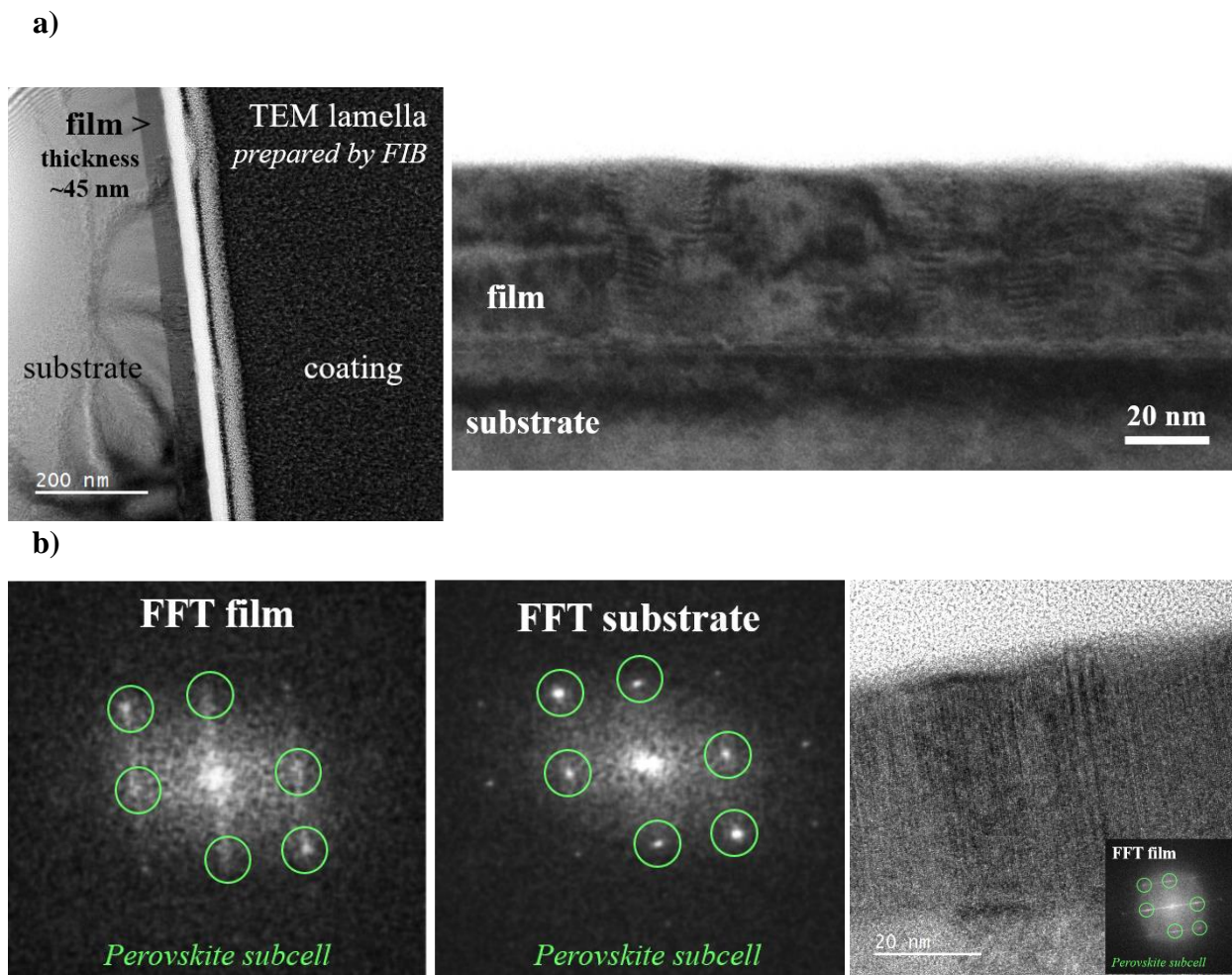


Figure 3.18:

- a) TEM cross section images of  $Pr_{0.8}Sr_{0.2}NiO_3/LSAT$   
 b) FFTs of substrate and film

Figure 3.18b shows The Fast Fourier Transform (FFT) performed for substrate and film. The spots in the FFT correspond to specific crystallographic planes and can be used to determine the orientation and symmetry of the crystal lattice [171]. The positions and intensities of these spots in the FFT pattern hold information about the arrangement of atoms in the crystal. From figure 3.18b the scattering points observed for the substrate are clear signatures of the perovskite crystal structure. Notably, for the films, the presence of numerous stacking faults and defects introduces diffuse scattering, evident as streaks in the diffraction pattern. However, it is essential to emphasize that despite this difference, the reflection positions in both the film and substrate remain identical

to those observed in the perovskite sub-cell. This observation leads to a safe conclusion: while perovskite phases are indeed present in the film, they do not constitute the dominant phase. As a logical progression, we proceeded to perform 3D Electron Diffraction (3D-ED), which could provide us with deeper insights.

Initially, 3D-ED is performed for the substrate. Figure 3.19 shows mapping of data points collected in the reciprocal space into the defined cell, we would typically expect to observe dots at the corners of the cell if the indexing is accurate for perovskite. However, in our indexing using the perovskite sub-cell dimensions of  $a_p * a_p * a_p$  ( $a_p$  – the parameter of the perovskite subcell), we noticed that only 35% of points can be indexed. This suggests the potential presence of a supercell ( $2a_p * 2a_p * 2a_p$ ). There are two possibilities for this supercell structure: Tetragonal (I-4) and Cubic (Fm-3m). After considering both Single Crystal XRD and 3D-ED data, it became more reasonable to conclude that the Cubic (Fm-3m) structure is the most likely one.

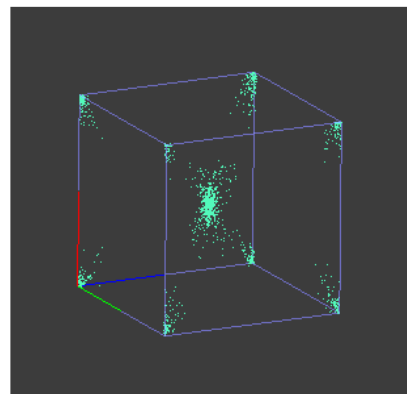


Figure 3.19

*Mapping of 3D-ED data points collected for substrate in the reciprocal space into perovskite  $a_p * a_p * a_p$  unit cell*

Figure 3.20 shows the 3D ED data collected from four distinct regions of the film. Here, we utilized the substrate indexed with a perovskite subcell  $a_p * a_p * a_p$  as our reference. Within the perovskite sub-cell, we observed several reflections concentrated in the middle. The  $I/\sigma$  value of 30 for these reflections signifies their strength and suitability for indexing. However, it's important to note that a significant portion of reflections remained unindexed, a fact reflected in the percentage of indexing.

This observation strongly suggests that the film, or at least a portion of it, possesses a supercell structure in relation to the perovskite. This supercell is likely related to the substrate's supercell. The inability to index a few reflections may be attributed to domains within the film that exhibit different orientations.

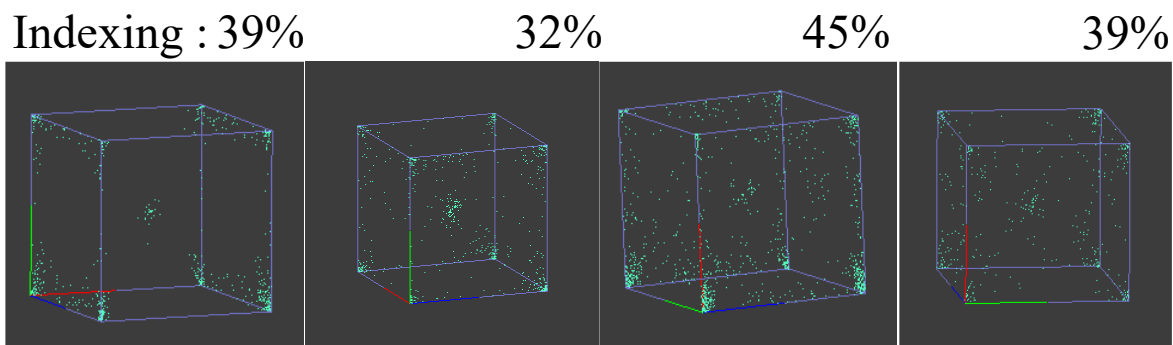


Figure 3.20

*Mapping of 3D-ED data points collected at 4 different regions of the film in the reciprocal space into perovskite  $a_p \cdot a_p \cdot a_p$  unit cell.*

To summarize the results from the TEM analysis, we can conclude that the film contains domains exhibiting a perovskite crystal structure. It is worth noting that we might have observed a predominance of perovskite-type diffraction if we had analyzed the film marked as 150mJ (Figure 3.14, films with a higher proportion of perovskite content have already been utilized in the reduction process). This is evident from the X-ray diffraction results. Furthermore, TEM analysis validates our observation that films lacking the (001) diffraction peak in X-ray diffraction patterns contain only a minimal amount of perovskite. Consequently, such films are not suitable candidates for the reduction process aimed at transforming them into the infinite layer phase.

### 3.7 PLD synthesis and reduction of STO-capped $\text{Pr}_{0.85}\text{Sr}_{0.15}\text{NiO}_3$ films on STO substrate

As discussed earlier, Harold Hwang's group capped their thin films with STO to stabilize perovskite phase and they claimed that it helped in attaining infinite layer phase by reduction. To study reduction of capped films, we investigated the reduction of 15% Sr-doped  $\text{PrNiO}_3$ -STO capped films, which falls within the superconducting dome [57]. The deposition conditions for the 15% Sr-doped samples did not differ significantly from the previous 20% Sr-doped ones. For STO capping the film after deposition and annealing, oxygen pressure in the chamber reduced 0.1mbar to 0.001mbar and other deposition conditions kept the same for STO.

Figure 3.21 shows the XRD patterns of  $\text{Pr}_{0.85}\text{Sr}_{0.15}\text{NiO}_3$  films on STO substrates with varying thicknesses of STO capping layers. An observable impact of upon decrease of the thickness of STO capping is the dominance of the secondary phases like those of RP type, as evidenced by the XRD patterns in figure 3.21. The film peak, positioned near the second-order substrate peak, can be interpreted as a combination of the perovskite phase and the diffraction originating from RP-type secondary phases. This is substantiated by the distinct presence of well-defined first-order and second-order peaks around  $2\theta=48^\circ$ , coupled with the observation of Laue reflections in close proximity to the film peaks. These features become less prominent as the capping thickness decreases. Based on these findings, it is reasonable to deduce, by comparing different film peaks in figure 3.21, that the influence of strain induced by STO significantly contributes to the stabilization of the perovskite phase in nickelates. However, using a thick STO cap might not be ideal for the reduction process.

The reduction of the STO-capped films required higher temperatures and longer duration. The use of STO as a capping introduces a diffusion barrier for oxygen in the film. This barrier hinders the reduction process, requiring higher temperatures to observe any signs of reduction. Figure 3.22 shows the XRD pattern before and after reduction attempts on a film capped with 25u.c of STO. Film did not respond to reduction as the thick STO cap act as a strong barrier for oxygen to diffuse and escape from the lattice. This film was again reduced for higher temperature for

longer duration of time but we did not observe any sign of reduction from XRD which was expected since the capping layer was too thick.

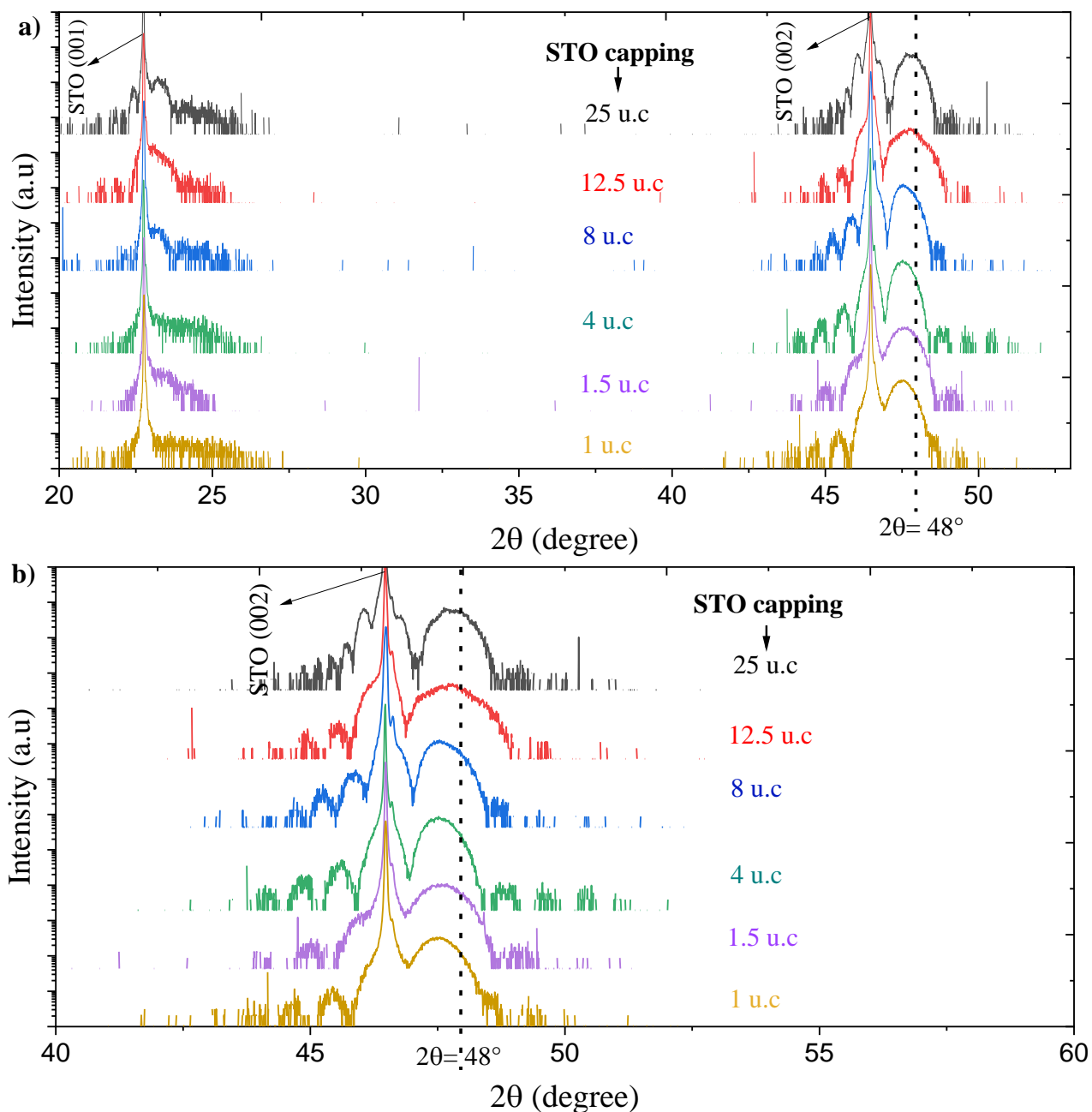
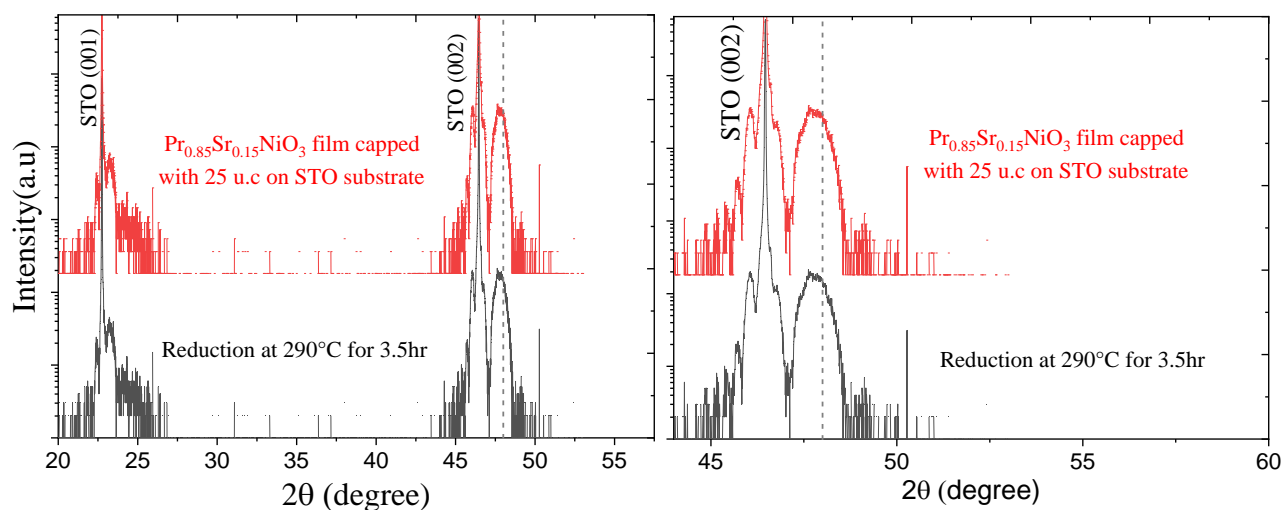


Figure 3.21:

- Thin film XRD pattern for  $\text{Pr}_{0.85}\text{Sr}_{0.15}\text{NiO}_3$  on STO substrate deposited with different STO capping thickness. Patterns are vertically shifted for clarity.
- Enlarged view focused on (002) diffraction peaks



*Figure 3.22: Thin film XRD patterns for as deposited  $Pr_{0.85}Sr_{0.15}NiO_3$  films on STO substrate following by capping the film with 25 unit-cell thickness of STO and corresponding reduced film XRD pattern.*

A comparison is made between films with 8u.c STO capping and those with 1u.c (figure 3.23a and 3.23b). Since the RP-type and perovskite phases react differently to reduction, the perovskite part of the film with 8u.c STO capping displays a reduction in lattice parameter, whereas the RP-type phase exhibits an increase in lattice parameter upon reduction. For films capped with only 1u.c, predominantly consisting of the RP-type phase, higher temperatures are required for reduction, and these films show an increase in lattice parameter upon reduction.

Our investigation into the role of STO capping has provided valuable insights into its influence on the phase composition of nickelate films and its consequences for the reduction process. It is evident that determining the ideal STO cap thickness is pivotal, as it allows us to simultaneously stabilize the perovskite phase and allow reduction on the film, ultimately leading to the optimization of the infinite layer phase without inducing degradation from reduction. However, it's important to note that reaching this balance through a series of deposition, reduction, and characterization processes is a time-consuming process characterization processes is a time-

consuming process, and my current timeline for completing the thesis within the prescribed timeframe is a constraint.

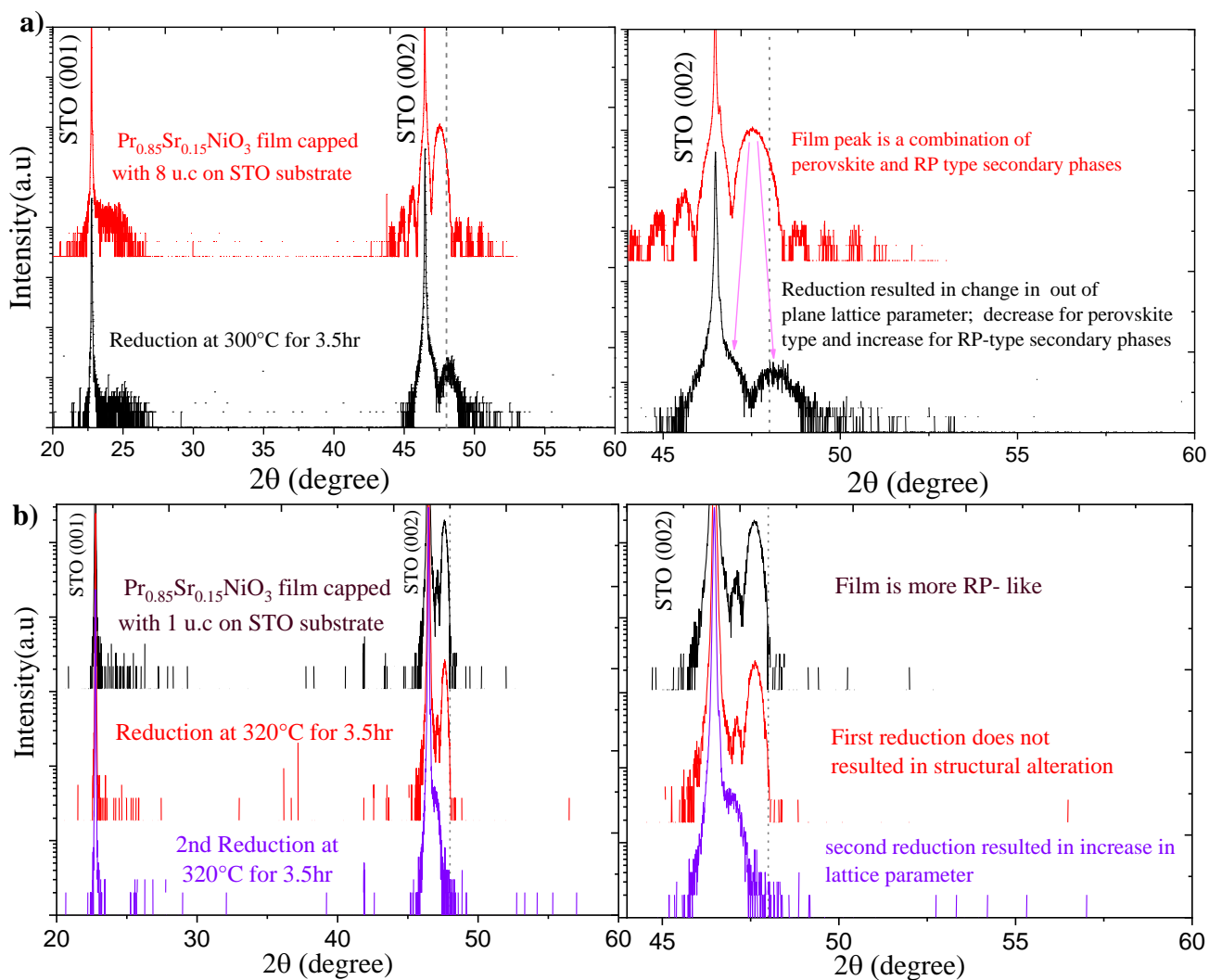


Figure 3.23:

Figure shows thin film XRD patterns for as deposited  $\text{Pr}_{0.85}\text{Sr}_{0.15}\text{NiO}_3$  films on STO substrate following by capping the film with STO and corresponding reduced film XRD pattern.

- a) Capped with 8 u.c of STO
- b) Capped with 1 u.c of STO

### 3.8 Summary and discussion

In this chapter, I aimed to provide a summary of our efforts with nickelates, starting with the optimization of growth parameters for perovskite  $\text{Pr}_{1-x}\text{Sr}_x\text{NiO}_3$  films. These films serve as precursors to the superconducting infinite layer  $\text{Pr}_{1-x}\text{Sr}_x\text{NiO}_2$  films that have been our focus. Despite our strides in enhancing film quality through adjustments in growth parameters and the use of annealing techniques, the persistent presence of coexisting RP type secondary phases posed an ongoing challenge, underscoring the intricacies involved in stabilizing infinite layer nickelate films.

We then turned our attention to examining how these films respond to  $\text{CaH}_2$ -based topotactic reduction, with the ultimate goal of stabilizing the infinite layer phase during the transition from the perovskite phase. In our pursuit of this objective, we conducted additional reduction experiments to explore the feasibility of shorter, more efficient reduction cycles. This approach aimed not only to systematically understand the reduction process but also to identify any stable intermediate phases. Through this, we observed a gradual decrease in the lattice parameters of the films, accompanied by an inevitable degradation of the film, as evidenced by X-ray patterns. This degradation was further reflected in insulating behavior observed in four-probe resistivity measurements.

To deepen our understanding of the phenomenon of inhomogeneous resistivity, we conducted resistivity measurements at different areas within the thin film. As we observed in our infinite layer  $\text{Nd}_{0.85}\text{Sr}_{0.15}\text{NiO}_2$ , diverse resistivity behaviors were evident in the reduced  $\text{Pr}_{0.8}\text{Sr}_{0.2}\text{NiO}_3$  across different regions of the sample. This strongly suggested that the primary source of this inhomogeneity lay within the reduction process itself, rather than issues related to the infinite layer phase.

In our quest to stabilize the perovskite  $\text{Pr}_{0.8}\text{Sr}_{0.2}\text{NiO}_3$  phase through PLD and subsequent reduction for infinite layer phase formation, we explored the use of LSAT substrates. These substrates, possessing a smaller lattice constant compared to STO, were expected to induce less strain and reduce RP-type defects. However, this introduced its own set of challenges due to the mismatch with the infinite layer phase's lattice constant. Optimal deposition conditions for  $\text{Pr}_{0.8}\text{Sr}_{0.2}\text{NiO}_3$  on LSAT closely resembled those on STO, with minor adjustments in laser energy.

Notably, LSAT films exhibited improved crystallinity. During the reduction process, the film deposited at 150mJ on LSAT displayed promising signs of partial conversion to the infinite layer phase. However, achieving stable crystalline formation remained elusive. Nonetheless, resistance measurements indicated an enhanced level of consistency in the reduction process compared to STO, signifying tangible progress in our ongoing research endeavors. TEM analysis performed on a film with poor 001 order diffraction shows film is highly disordered and majority of the film is difficult to index with pure perovskite sub-cell. Our observation aligns with X-ray diffraction results, indicating that films lacking the (001) diffraction peak contain minimal perovskite and are unsuitable for the transformation into the infinite layer phase

To investigate the impact of STO capping on the stabilization of the perovskite and infinite layer phases, we performed reduction on 15% Sr-doped  $\text{PrNiO}_3$ -STO capped films. The deposition conditions for these samples remained same as optimized for 20% Sr-doped ones, with STO capping introduced after deposition. Varying the thickness of the STO capping layer had a notable impact on the film's phase composition. Thinner STO capping layers allowed secondary phases, particularly the RP-type phases, to dominate alongside the perovskite phase. Thicker STO caps, while aiding in perovskite phase stabilization, pose challenges in achieving reduction as the STO act as a diffusion barrier and prevent oxygen from escaping the lattice.



## SUMMARY AND CONCLUSIONS

The research works conducted in this thesis are motivated by the observation of superconductivity in infinite layer nickelates, which is achieved through the reduction of perovskite nickelate thin films using  $\text{CaH}_2$ . Within the scope of this thesis, both thin film and bulk nickelates were explored.

For the investigation of bulk nickelates,  $\text{Nd}_{0.8}\text{Sr}_{1.2}\text{NiO}_4$  was selected due to its unique characteristics. This material offers topotactic reducibility, enabling it to transform into the desired Ni-O square planar structure. Additionally, it has the potential to achieve a nominal nickel valency similar to that of infinite layer superconducting nickelates by topotactic reduction, which identified to have played a key role in superconductivity in infinite layer nickelate. These properties, combined with its stability and ease of synthesis, make it an attractive choice compared to perovskite structures.

To begin the study, we synthesized polycrystalline  $\text{Nd}_{0.8}\text{Sr}_{1.2}\text{NiO}_4$  samples using a solid-state reaction method. Our initial analysis using powder X-ray diffraction (PXRD) revealed that these samples exhibited a tetragonal  $I4/mmm$  symmetry with no visible impurity peaks. Electrical resistivity measurements demonstrated metallic behavior, akin to the parent compound of superconducting infinite layer nickelates.

Subsequently, we topotactically reduced these  $\text{Nd}_{0.8}\text{Sr}_{1.2}\text{NiO}_4$  samples using  $\text{CaH}_2$ , resulting in stable  $\text{Nd}_{0.8}\text{Sr}_{1.2}\text{NiO}_3$  samples. Structural analysis using PXRD and TEM revealed a transition from a tetragonal to an orthorhombic configuration, indicating reduced symmetry within the  $Immm$  space group. During this reduction process, oxygen atoms were removed from the Ni-O plane, leading to the formation of  $\text{NiO}_2$  square stripes along the z-direction (as depicted in Figure 2.3). The transformation of the crystal structure from  $I4/mmm$  to  $Immm$  was accompanied by a shift in transport behavior, transitioning from metallic to highly insulating at lower temperatures. Importantly, no indications of superconductivity were observed.

In contrast to the reduction process in infinite layer nickelates, where oxygen is removed from the apex of the Ni-O octahedra, the reduction in  $\text{Nd}_{0.8}\text{Sr}_{1.2}\text{NiO}_4$  resulted in the removal of

oxygen atoms from the Ni-O plane. These observations suggest the development of a 1D or quasi-1D system, rather than the typical 2D or quasi-2D system seen in infinite layer nickelates. This alteration led to a reduction in the number of charge carriers and disrupted potential conductive pathways.

In summary, our research involving polycrystalline RP1 nickelate reveals that topotactic reduction using  $\text{CaH}_2$  is an effective method for stabilizing phases that are otherwise challenging to synthesize. Furthermore, we have determined that achieving a nominal nickel valence state of  $\text{Ni}^{1.2+}$  and maintaining a Ni-O square planar structure may be necessary conditions, although they are insufficient on their own to induce superconductivity in nickelates.

To deepen our understanding based on our current findings, we can expand our investigations by exploring topotactic reduction of RP1 compounds with different rare-earth elements and experimenting with the doping of other suitable alkaline-earth elements. Additionally, conducting experiments with single crystals of these compounds can help us eliminate any size-related effects on the properties we observe. An intriguing avenue for further exploration is whether there is a method to selectively remove apical oxygen from the perovskite layer in RP. This approach could bring us closer to 2D or quasi-2D system similar to that of superconducting infinite-layer nickelates. Furthermore, investigating alternative synthesis methods for this reduced compound may provide insights into the potential role of hydrogen, if any, induced by the reduction process involving  $\text{CaH}_2$ . This could help us better understand the observed changes in both physical and structural properties.

Throughout our studies of nickelate thin films and the  $\text{CaH}_2$  reduction process, we have encountered a dynamic interplay of behaviors and challenges. After dedicated efforts and meticulous optimization, our research group stabilized the  $\text{Nd}_{0.85}\text{Sr}_{0.15}\text{NiO}_2$  infinite layer phase; we observed a drop in resistivity around 10 K, yet did not reach a zero-resistivity value. This scenario encouraged us to consider the possibility that a non-superconducting part might be contributing to the measurements from the specific region of the film under investigation. This led us to investigate further, revealing distinct resistivity behaviors at different locations within the film. These variations hinted at inhomogeneity stemming from various sources, including aspects related to synthesis, the reduction processes, and strain induced by the substrate. These results and

observations served as a significant motivation for delving further into the study of nickelate thin films as part of my thesis, with a particular focus on the synthesis process, the encountered difficulties, and the challenges related to achieving homogeneity during the reduction process.

Despite our efforts to optimize growth parameters and explore reduction processes, challenges persist. The presence of coexisting phases such as RP along with desired perovskite phase is confirmed from TEM analysis. Inhomogeneous resistivity behaviour is observed to an artefact from the reduction process, as we observed different resistive behaviour across the reduced samples irrespective of its final phase. While progress was made, including insights from structural and transport studies before and after reduction the path to stable stabilise infinite layer phase still remain unclear.

Significantly, our TEM analysis of the LSAT substrate revealed a deviation from the expected perovskite characteristics. The fact that we cannot flag the substrate as pure perovskite, which is crucial for achieving epitaxial stability in the perovskite thin film, raises further concerns. However, the films deposited on LSAT substrates exhibited a higher degree of homogeneity upon reduction compared to reduced films that are deposited on STO. This observation can be attributed to the fact that LSAT provides a better environment for epitaxial stabilisation of perovskite phase during PLD synthesis by applying less strain on the film compared to STO.

Our investigation into the role of STO capping has provided valuable insights into its influence on the phase composition of nickelate films and its consequences for the reduction process. We highlight that optimal thickness STO has to be found, as it should simultaneously stabilize the perovskite phase and not be a barrier for reduction, ultimately leading to the optimization of the infinite layer phase without inducing degradation from reduction.

Moreover, the limited success and control in obtaining samples of infinite layer of  $\text{Pr}_{1-x}\text{Sr}_x\text{NiO}_2$  can potentially be further attributed to the critical nature of both the film quality and the chemical reduction process. To optimize the chemical reduction process, numerous parameters need to be considered. These include phase purity of the film before reduction, the amount of the reduction agent ( $\text{CaH}_2$  powder), the reduction temperature, the chemical reaction time, the volume of Pyrex tubes, pressure inside the tube during reduction, the thin film thickness, and the relative positions of the thin-film samples and the  $\text{CaH}_2$  powder. Due to the challenges in controlling these

multiple factors during sample preparation, the same nominal fabrication process can yield reduced samples with completely undesired transport properties and structural properties.

Addressing these issues primarily requires a focus on stabilizing the perovskite phase using PLD. Quantitative measurements of the film stoichiometry could provide valuable insights into necessary adjustments during deposition. Electron Energy Loss Spectroscopy (EELS) can offer information about the type and quantity of atoms present, as well as the chemical state of these atoms. Additionally, X-ray Photoelectron Spectroscopy (XPS) can help in identifying the elemental composition and oxidation states of the elements. If necessary, it can be advantageous to prepare a target with an excess of specific constituents in the film to ensure a stoichiometric plume, ultimately leading to the formation of a stoichiometric film. With these pieces of information in hand, we can fine-tune PLD parameters to enhance the perovskite nature of the film.

Once we gain control over the synthesis of perovskite with desired properties, we can proceed to the reduction stage. Our next focus will be exploring the alteration of reduction pressure by adjusting the volume of the Pyrex tube used and its impact on reduction. Furthermore, we can explore alternative reduction methods. Recent reports suggest a reduction method involving aluminum deposition atop the nickelate layer. This technique selectively reduces the nickelate layer while forming aluminum oxide on the surface, allowing precise control over the film's oxygen content and facilitating topotactic transformation. These developments open up a multitude of possibilities for our research.



## Appendix

### A1-Pulsed Laser deposition (PLD).

The PLD system I utilized for thin film deposition comprises a laser, a vacuum system integrated with the deposition chamber, and optics guiding laser pulses. The system incorporates the COMPexPro Excimer Laser, utilizing excimer gas laser technology that exploits excited dimer molecules to emit ultraviolet (UV) light of wavelength 248 nm. The laser's short pulse duration, typically in the range of several nanoseconds (ns), aligns perfectly with the requirements of PLD procedures. Our vacuum system could achieve a level of up to  $10^{-8}$  mbar within the PLD deposition chamber and the substrate heater can attain temperatures up to  $900^{\circ}\text{C}$ .

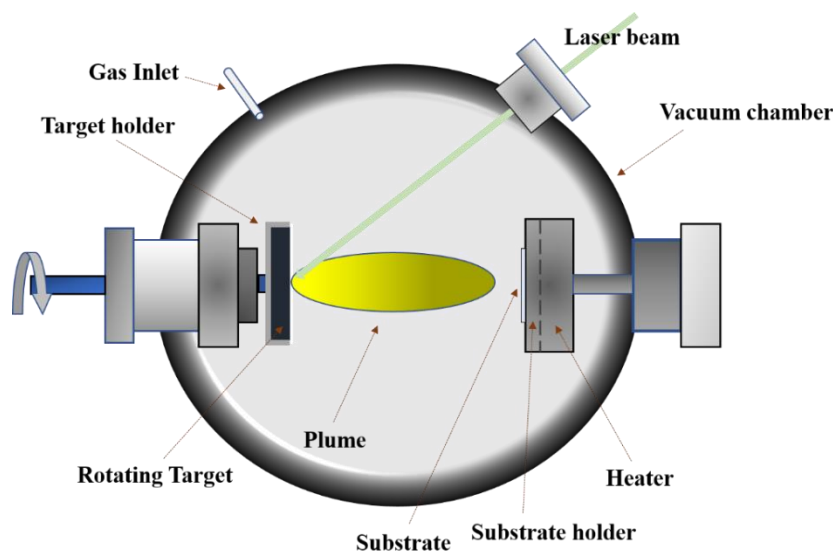


Figure A1:

Schematic of PLD chamber used for the thin film deposition

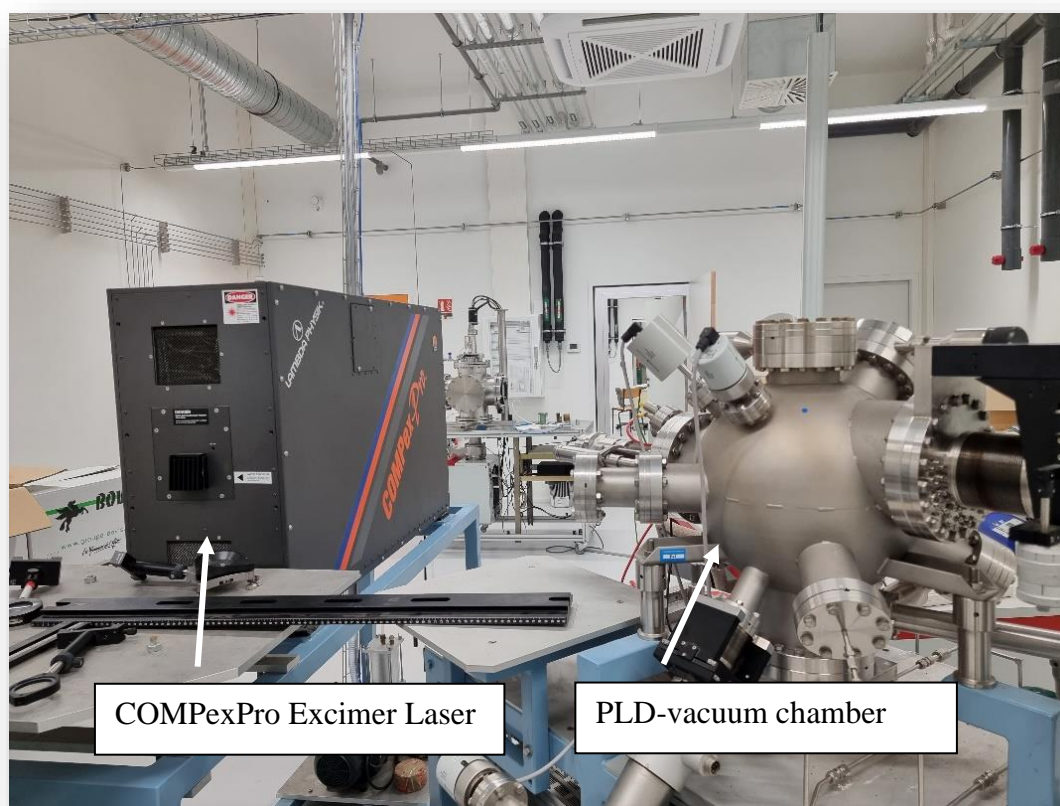


Figure A2:

Excimer laser and PLD chamber used for the thin film deposition. CRISMAT lab

## A2-X-ray diffraction

The thin film synthesized as a part of this thesis was characterized using the Bruker D8 Discover XRD machine with Cu-K $\alpha$  radiation. The diffraction patterns were captured in the  $2\theta$ - $\omega$  geometry, where the X-ray incident angle remains constant while the detector is rotated to scan across various  $2\theta$  angles. Prior to the scan, the XRD device underwent calibration using known substrate parameters. This calibration process involves meticulously adjusting the angular positions ( $\omega$  values) to ensure alignment with the known crystallographic orientation of the substrate. These

deviations in  $\omega$  values are identified and then applied as corrections to subsequent measurements. The calibration process involving z-scan and rocking curve measurements ensures the accuracy of the XRD measurements and the integrity of the obtained results.

Polycrystalline samples are characterized using X'Pert Pro XRD machine by PANalytical. I employed the theta-theta scan, where the X-ray beam is incident on the sample at a fixed angle, referred to as  $\theta$ . The detector is positioned on the opposite side of the sample and also at an angle of  $\theta$ . As the diffracted X-rays emerge from the sample at various angles, they are captured by the



Figure A3:

D8 Discover XRD equipment. CRISMAT lab

detector. For polycrystalline samples, which consist of numerous crystalline grains oriented in different directions, the theta-theta scan is advantageous. It enables the simultaneous observation of multiple diffraction peaks corresponding to the various crystallographic planes within the individual grains.

### A3-Physical Property Measurement System (PPMS)

In this thesis, all electrical transport measurements were conducted using the Physical Property Measurement System (PPMS) provided by Quantum Design. This cryogenic apparatus operates within the temperature range of 400 K down to 2 K and employs both a closed-cycle refrigeration method and a flow cryostat-based system. Magnetic fields are generated using a superconducting coil composed of the NbTi alloy, which is immersed in liquid helium. For the purpose of electrical measurements, a current ranging from 0.1  $\mu\text{A}$  to 5 mA can be applied to the



Figure A4:

PPMS 9T equipment. CRISMAT lab

samples. For more detailed information about the equipment, refer to the Quantum Design PPMS manual.

## A4-Resistivity measurements

Electrical resistivity measurements can conventionally be carried out using two distinct methods, contingent on the nature of conduction. These methods include the two-probe and four-probe techniques. The two-probe method is well-suited for insulating systems where the contact resistance is negligible compared to sample. However, in the case of metals and semiconductors, the four-probe method is more effective in eliminating contact resistance. I employed linear four probe geometry for resistivity measurement for thin film as well as bulk samples. In linear measurement geometry, ensuring a uniform current distribution across the sample necessitates a substantial length-to-width ratio.

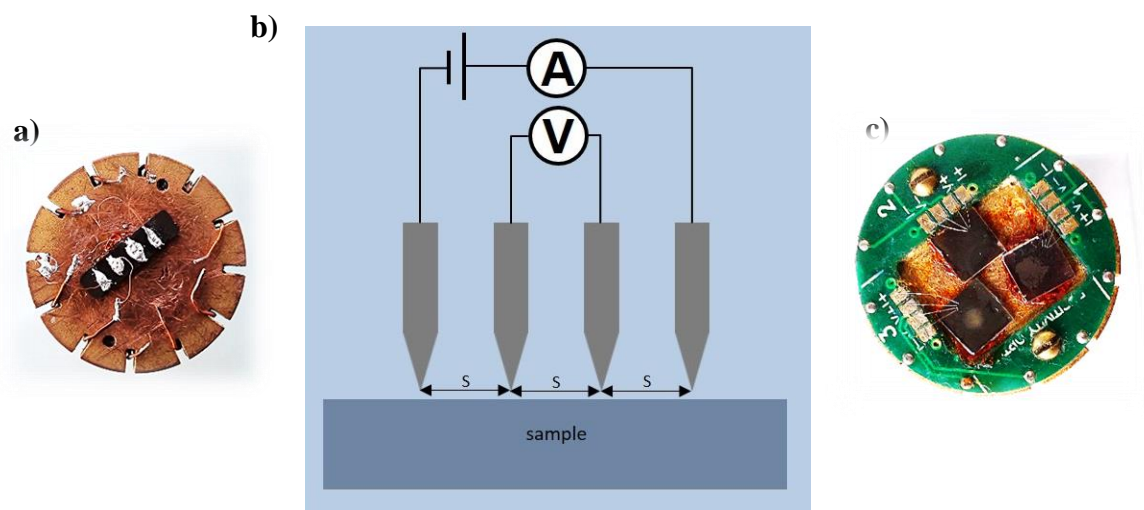


Figure A5:

- a) PPMS puck with polycrystalline sample stick on it. Lead four probe electrical contacts are given with the aid of ultrasonic soldering
- b) Schematic on four probe contacts
- c) PPMS puck with thin film samples stick on it. Four probe contacts are given with wire bonder

Additionally, maintaining equal distances between the measurement pads is crucial to ensure that the voltage pads align with equipotential surface lines. To achieve accurate measurements, the resistivity ( $\rho$ ) can be calculated using the formula:

$$\rho = R * \left[ \frac{(d * w)}{l} \right]$$

In this equation, R represents resistance,  $l$  signifies the distance between the two voltage probes,  $w$  stands for width, and  $d$  represents thickness. The product of  $d$  and  $w$  gives the cross-sectional area (A). Above equation can be used in bulk materials but for thin film samples with dimensions in nano regime, correction factors should be taken into account. For the case of thin films on a non-conducting bottom surface, resistivity can be calculated from resistance measured as [172]

$$\rho = \frac{R * \pi * w}{\ln 2} * F\left(\frac{w}{S}\right)$$

$S$  is the distance between the probes and  $F\left(\frac{w}{S}\right)$  is the correction factor. Considering the thickness of the film and spacing between the probes. Since the thickness of the film is negligible compared to probe spacing,  $F\left(\frac{w}{S}\right)$  can be approximated to unity. For the thin films presented in this thesis, resistivity is calculated from the resistance measured by PPMS using the formula

$$\rho = \frac{R * \pi * w}{\ln 2}$$

In the context of this thesis, for the electrical measurements on thin films, the contact pads were attached using direct ultrasonic wire bonding. A West Bond wire-bonder was utilized for this purpose, employing high-purity aluminum wire. Electrical contacts on bulk materials are either made using silver paste or Ultrasonic vibrator-assisted lead contacts.

## A5-SQUID magnetometer

The Superconducting Quantum Interference Device (SQUID) is a magnetometer designed for precise magnetic measurements. It can detect even the faintest magnetic fields due to its remarkable sensitivity. In applications demanding high sensitivity, the DC-SQUID configuration, which consists of two parallel-connected Josephson junctions within a superconducting loop, is favored. This configuration produces a counteracting screening supercurrent ( $I_s$ ) within the loop when an

external magnetic field perturbs the coil. This supercurrent generates an additional phase known as the Josephson phase, which correlates with the external magnetic flux. For the magnetic measurements we used Quantum Design MPMS 5S SQUID instrument. Operating from 1.8 K to 400 K, it accommodates a superconducting magnet that generates fields from -9 T to +9 T.



Figure A6:

SQUID equipment. CRISMAT lab

## A6-Experimental data analysis and fitting data

I employed Python for both data analysis and curve fitting tasks, specifically the Spyder environment provided by Anaconda. I used libraries such as Matplotlib, Numpy, and Lmfit. Matplotlib facilitated the creation of visual representations, aiding in the interpretation of data patterns, Numpy in handling numerical operations and computations and the Lmfit library helped in optimizing curve fitting procedures, enhancing the accuracy of parameter estimation.

Here is an example of code snippet used for plotting and fitting as part of the thesis

```
1 import numpy as np
2 import matplotlib.pyplot as plt
3 from lmfit import Model
4
5 # Define the susceptibility model
6 def susceptibility_model(T, C, q, A):
7     return (C / (T - q)) + A
8
9 # Define the linear model for the inset plot
10 def linear_model(T, slope, intercept):
11     return slope * T + intercept
12
13 # Read the data and skip the first row
14 data = np.loadtxt("MK3 FC.dat", skiprows=1)
15 T = data[:, 0] # Temperature data
16 chi = data[:, 1] # Susceptibility data
17
18 # Select a temperature range for the plot
19 mask = (T > 130) & (T < 300)
20 T_mask = T[mask]
21 chi_mask = chi[mask]
22
23 # Create the susceptibility model
24 susceptibility_model = Model(susceptibility_model)
25
26 # Set the initial guesses for the susceptibility model parameters
27 params = susceptibility_model.make_params(C=1.66, q=-80, A=.00001)
28
29 # Perform the susceptibility model fit
30 result = susceptibility_model.fit(chi_mask, T=T_mask, params=params)
31
32 # Print the fit parameters and their uncertainties
33 print(result.fit_report())
```

```

35 # Create the plot
36 fig, ax = plt.subplots(figsize=(8,6)) # Set the figure size to match the column width
37 ax.plot(T, chi, marker='o', markerfacecolor='blue', markersize=8, alpha=0.8,
38         linestyle='none', markeredgewidth='black', linewidth=0.5, label='FC Susceptibility')
39 ax.plot(T, chi, '-', color='blue', linewidth=1.5) # Add lines connecting the data points
40
41 ax.plot(T_mask, result.best_fit, 'r-', label='Modified C-W fit') # Plot the fitted model
42 ax.set_xlabel('Temperature (K)', fontsize=14, fontweight='bold') # Set the x-axis label
43 ax.set_ylabel('$\chi$ (emu/mol.Oe)', fontsize=14, fontweight='bold') # Set the y-axis label
44 plt.axvspan(130,300,color='r', alpha=0.1, lw=1)
45 plt.axvspan(3,130,color='y', alpha=0.05, lw=1)
46 ax.legend(fontsize=8) # Add a legend
47 plt.tight_layout() # Adjust the layout to prevent labels from overlapping
48 ax.tick_params(axis='both', which='major', labelsize=12)
49
50 # Create an inset to plot the inverse susceptibility data
51 inset_ax = ax.inset_axes([0.3, 0.3, 0.5, 0.5])
52 inset_ax.scatter(T, 1/chi, s=50, c='green', alpha=0.8, edgecolors='black', linewidths=0.5)
53
54 inset_ax.set_xlabel('Temperature (K)', fontsize=10)
55 inset_ax.set_ylabel('1/$\chi$', fontsize=10)
56 inset_ax.tick_params(axis='both', which='major', labelsize=8)
57 inset_ax.axvspan(130,300,color='r', alpha=0.1, lw=1)
58 inset_ax.axvspan(3,130,color='y', alpha=0.05, lw=1)
59
60 # Define the linear model for the inset plot
61 linear_model = Model(linear_model)
62
63 # Set the initial guesses for the linear model parameters
64 linear_params = linear_model.make_params(slope=0, intercept=0)
65
66 # Select a temperature range for the linear model fit
67 linear_mask = (T > 130) & (T < 300)
68 T_linear = T[linear_mask]
69 chi_linear = 1/chi[linear_mask]
70
71 # Perform the linear model fit
72 linear_result = linear_model.fit(chi_linear, T=T_linear, params=linear_params)
73
74 # Plot the linear fit in the inset plot
75 inset_ax.plot(T_linear, linear_result.best_fit, 'r-', label='Curie-Wiess region')
76
77 # Add a legend to the inset plot
78 inset_ax.legend(fontsize=8)
79 ax.set_title('Temperature vs. Susceptibility', fontsize=16)
80 # Save the figure in a high-quality format
81 plt.savefig('susceptibility_plot.png', dpi=300, bbox_inches='tight')

```

## A7-Fit results eq 2.4

fitting method = leastsq

function evals = 9

data points = 251

variables = 1

Table A1: Fit results eq 2.4

Temperature (K)	S(T) ( $10^{-21}$ )	chi-square	reduced chi-square	Akaike info crit	Bayesian info crit	R-squared
20.0	8.6782	0.04697032	1.87e-04	-2152.506	-2148.981	-0.242686
10.0	5.6219	0.04004487	1.68e-04	-2192.545	-2189.019	0.968092
5.0	2.4539	0.07306122	2.92e-04	-2041.619	-2038.094	0.996306
3.0	4.3546	0.03824763	3.86e-04	-784.8843	-782.2792	0.998509

The chi-square is a measure of how much the fit function deviates from the data points. The lower the chi-square, the better the fit. The reduced chi-square is the chi-square divided by the degrees of freedom, which is the number of data points minus the number of variables. The reduced chi-square can be used to compare different models with the same data set. The Akaike information criterion (AIC) and the Bayesian information criterion (BIC) are also used to compare different models, but they take into account the complexity of the model as well. The lower the AIC and BIC, the better the model. The R-squared is a measure of how much of the variation in the data is explained by the fit function. The higher the R-squared, the better the fit.

The results show that the fit function is not very good for the temperature of 20.0 K, as the chi-square, the reduced chi-square, the AIC, and the BIC are all high, and the R-squared is negative. This means that the fit function does not capture the behavior of the data at this temperature, and there may be other factors influencing the parameter S(T). The fit function is much better for the temperatures of 10.0 K, 5.0 K, and 3.0 K, as the chi-square, the reduced chi-square, the AIC, and the BIC are all low, and the R-squared is close to 1. This means that the fit function fits the data well at these temperatures, and the value of S(T) is estimated with high precision.

## A8-Fit results eq 2.5

fitting method = leastsq

function evals = 213

data points = 240

variables = 2

Table A2: Fit results eq 2.5

Temperature (K)	a ( $10^{-21}$ )	b( $10^{-11}$ )	chi-square	reduced chi-square	Akaike info crit	Bayesian info crit	R-squared
3.0	2.56299	-2.7477	0.26789	0.00112	-1627.468	-1620.507	0.99974
5.0	2.22270	-2.3142	0.10636	1.77e-04	-5188.327	-5179.529	0.99988
10.0	1.76394	1.3871	0.08653	1.44e-04	-5312.31	-5303.516	0.99881
20.0	0.50040	1.7169	0.10724	1.79e-04	-5183.365	-5174.568	0.88002

### A9-Fit results eq 2.9

fitting method = leastsq

function evals = 566

data points = 899

variables = 3

Table A3: Fit results eq 2.9

Temperature (K)	chi-square	reduced chi-square	Akaike info crit	Bayesian info crit	R-squared
20.0	0.140031	1.5646e-04	-7865.921	-7851.520	0.974805
10.0	0.124317	1.3875e-04	-7982.694	-7968.290	0.999662
5.0	0.161335	1.8006e-04	-7748.373	-7733.969	0.999953
3.0	0.254942	7.1412e-04	-2605.016	-2593.357	0.999924



## References

- [1] Z. X. Shen and D. S. Dessau, “Electronic structure and photoemission studies of late transition-metal oxides — Mott insulators and high-temperature superconductors,” *Phys. Rep.*, vol. 253, no. 1–3, pp. 1–162, Mar. 1995, doi: 10.1016/0370-1573(95)80001-A.
- [2] M. Imada, A. Fujimori, and Y. Tokura, “Metal-insulator transitions,” *Rev. Mod. Phys.*, vol. 70, no. 4, p. 1039, Oct. 1998, doi: 10.1103/RevModPhys.70.1039.
- [3] M. Uehara, S. Mori, C. H. Chen, and S. W. Cheong, “Percolative phase separation underlies colossal magnetoresistance in mixed-valent manganites,” *Nat.* 1999 3996736, vol. 399, no. 6736, pp. 560–563, Jun. 1999, doi: 10.1038/21142.
- [4] J. Van den Brink, G. Khaliullin, and D. Khomskii, “Charge and Orbital Order in Half-Doped Manganites,” *Phys. Rev. Lett.*, vol. 83, no. 24, p. 5118, Dec. 1999, doi: 10.1103/PhysRevLett.83.5118.
- [5] P. W. Anderson, “Antiferromagnetism. Theory of Superexchange Interaction,” *Phys. Rev.*, vol. 79, no. 2, p. 350, Jul. 1950, doi: 10.1103/PhysRev.79.350.
- [6] J. B. Goodenough, “Theory of the Role of Covalence in the Perovskite-Type Manganites [La, M(II)]MnO<sub>3</sub> Phys. Rev., vol. 100, no. 2, p. 564, Oct. 1955, doi: 10.1103/PhysRev.100.564.
- [7] C. Zener, “Interaction between the d-Shell in the Transition Metals. II. Ferromagnetic Compounds of Manganese with Perovskite Structure,” *Phys. Rev.*, vol. 82, no. 3, p. 403, May 1951, doi: 10.1103/PhysRev.82.403
- [8] G. Demazeau, A. Marbeuf, M. Pouchard, and P. Hagenmuller, “Sur une série de composés oxygènes du nickel trivalent dérivés de la perovskite,” *J. Solid State Chem.*, vol. 3, no. 4, pp. 582–589, Nov. 1971, doi: 10.1016/0022-4596(71)90105-8.
- [9] P. Lacorre, + J B Torrance, J. Pannetier, S. A. I. Nazzal, " P W Wang, and T. C. Huang, “Synthesis, Crystal Structure, and Properties of Metallic PrNiO<sub>3</sub>: Comparison with Metallic NdNiO<sub>3</sub> and Semiconducting SmNiO<sub>3</sub>,” 1991.
- [10] J. B. Torrance, P. Lacorre, A. I. Nazzal, E. J. Ansaldo, and O. Ch Niedermayer, “Systematic study of insulator-metal transitions in perovskites RNiO<sub>3</sub> (R =Pr, Nd, Sm, Eu) due to closing of charge-transfer gap,” 1992.
- [11] D. Li *et al.*, “Superconductivity in an infinite-layer nickelate,” *Nature*, vol. 572, no. 7771, pp. 624–627, Aug. 2019, doi: 10.1038/s41586-019-1496-5.
- [12] L. D. Landau and V. L. Ginzburg, “On the theory of superconductivity,” *Zh. Eksp. Teor. Fiz.*, vol. 20, p. 1064, 1950, Accessed: Nov. 03, 2022. [Online]. Available: <http://cds.cern.ch/record/486430>.
- [13] J. Bardeen, L. N. Cooper, and J. R. Schrieffer, “Microscopic Theory of Superconductivity,” *Phys. Rev.*, vol. 106, no. 1, p. 162, Apr. 1957, doi: 10.1103/PhysRev.106.162.
- [14] J. G. Bednorz and K. A. Müller, “Possible highT<sub>c</sub> superconductivity in the Ba–La–Cu–O

- system,” *Zeitschrift für Phys. B Condens. Matter* 1986 642, vol. 64, no. 2, pp. 189–193, Jun. 1986, doi: 10.1007/BF01303701.
- [15] M. K. Wu *et al.*, “Superconductivity at 93 K in a new mixed-phase Yb-Ba-Cu-O compound system at ambient pressure,” *Phys. Rev. Lett.*, vol. 58, no. 9, pp. 908–910, 1987, doi: 10.1103/PhysRevLett.58.908.
- [16] Z. A. Ren *et al.*, “Superconductivity and phase diagram in iron-based arsenic-oxides  $\text{ReFeAsO}_{1-\delta}$  (Re = rare-earth metal) without fluorine doping,” *Europhys. Lett.*, vol. 83, no. 1, p. 17002, Jun. 2008, doi: 10.1209/0295-5075/83/17002.
- [17] H. Takahashi, K. Igawa, K. Arii, Y. Kamihara, M. Hirano, and H. Hosono, “Superconductivity at 43 K in an iron-based layered compound  $\text{LaO}_{1-x}\text{F}_x\text{FeAs}$ ,” *Nat.* 2008 4537193, vol. 453, no. 7193, pp. 376–378, Apr. 2008, doi: 10.1038/nature06972.
- [18] F. C. Zhang and T. M. Rice, “Effective Hamiltonian for the superconducting Cu oxides,” *Phys. Rev. B*, vol. 37, no. 7, pp. 3759–3761, 1988, doi: 10.1103/PhysRevB.37.3759.
- [19] V. I. Anisimov, D. Bukhvalov, and T. M. Rice, “Electronic structure of possible nickelate analogs to the cuprates,” *Phys. Rev. B*, vol. 59, no. 12, p. 7901, Mar. 1999, doi: 10.1103/PhysRevB.59.7901.
- [20] K. W. Lee and W. E. Pickett, “Infinite-layer  $\text{LaNiO}_2$ :  $\text{Ni}^{1+}$  is not  $\text{Cu}^{2+}$  [33],” *Phys. Rev. B - Condens. Matter Mater. Phys.*, vol. 70, no. 16, pp. 1–7, Oct. 2004, doi: 10.1103/PhysRevB.70.165109.
- [21] A. S. Botana, V. Pardo, and M. R. Norman, “Electron doped layered nickelates: Spanning the phase diagram of the cuprates,” *Phys. Rev. Mater.*, vol. 1, no. 2, p. 021801, Jul. 2017, doi: 10.1103/PHYSREVMATERIALS.1.021801/FIGURES/5/MEDIUM.
- [22] J. Chaloupka and G. Khaliullin, “Orbital order and possible superconductivity in  $\text{LaNiO}_3/\text{LaMO}_3$  superlattices,” *Phys. Rev. Lett.*, vol. 100, no. 1, p. 016404, Jan. 2008, doi: 10.1103/PHYSREVLETT.100.016404/FIGURES/4/MEDIUM.
- [23] P. Hansmann, X. Yang, A. Toschi, G. Khaliullin, O. K. Andersen, and K. Held, “Turning a Nickelate Fermi Surface into a Cupratelike One through Heterostructuring,” *Phys. Rev. Lett.*, vol. 103, no. 1, p. 016401, Jun. 2009, doi: 10.1103/PHYSREVLETT.103.016401/FIGURES/3/MEDIUM.
- [24] S. Middey, J. Chakhalian, P. Mahadevan, J. W. Freeland, A. J. Millis, and D. D. Sarma, “Physics of Ultrathin Films and Heterostructures of Rare-Earth Nickelates,” <https://doi.org/10.1146/annurev-matsci-070115-032057>, vol. 46, pp. 305–334, Jul. 2016, doi: 10.1146/ANNUREV-MATSCI-070115-032057.
- [25] A. V. Boris *et al.*, “Dimensionality control of electronic phase transitions in nickel-oxide superlattices,” *Science (80-. )*, vol. 332, no. 6032, pp. 937–940, May 2011, doi: 10.1126/SCIENCE.1202647/SUPPL\_FILE/1202647.BORIS.SOM.PDF.
- [26] E. Benckiser *et al.*, “Orbital reflectometry of oxide heterostructures,” *Nat. Mater.* 2011 103, vol. 10, no. 3, pp. 189–193, Feb. 2011, doi: 10.1038/nmat2958.
- [27] A. S. Disa *et al.*, “Orbital engineering in symmetry-breaking polar heterostructures,” *Phys.*

- Rev. Lett.*, vol. 114, no. 2, p. 026801, Jan. 2015, doi: 10.1103/PHYSREVLETT.114.026801/FIGURES/3/MEDIUM.
- [28] J. Zhang *et al.*, “Large orbital polarization in a metallic square-planar nickelate,” *Nat. Phys.* 2017 139, vol. 13, no. 9, pp. 864–869, Jun. 2017, doi: 10.1038/nphys4149.
- [29] Y. Tokura and N. Nagaosa, “Orbital Physics in Transition-Metal Oxides,” *Science (80-. )*, vol. 288, no. 5465, pp. 462–468, Apr. 2000, doi: 10.1126/SCIENCE.288.5465.462.
- [30] P. M. Woodward, “Octahedral Tilting in Perovskites. I. Geometrical Considerations,” *Acta Crystallogr. Sect. B*, vol. 53, no. 1, pp. 32–43, Feb. 1997, doi: 10.1107/S0108768196010713.
- [31] M. Ohring, “Why are thin films different from the bulk?,” <https://doi.org/10.1117/12.180875>, vol. 2114, pp. 624–639, Jul. 1994, doi: 10.1117/12.180875.
- [32] S. Catalano, M. Gibert, J. Fowlie, J. Iñiguez, J. M. Triscone, and J. Kreisel, “Rare-earth nickelates RNiO<sub>3</sub>: thin films and heterostructures,” vol. 81, no. 4, p. 046501, Feb. 2018, doi: 10.1088/1361-6633/AAA37A.
- [33] P. P. Edwards, S. R. Johnson, M. O. Jones, A. Porch, and R. L. Johnston, “The size - Induced metal - Insulator transition in colloidal gold,” *Stud. Surf. Sci. Catal.*, vol. 132, pp. 719–724, 2001, doi: 10.1016/s0167-2991(01)82188-1.
- [34] H. HESS, “THE INSULATOR-METAL TRANSITION IN DENSE PLASMAS,” *Strongly Coupled Plasma Phys.*, pp. 483–494, 1990, doi: 10.1016/B978-0-444-88363-6.50066-2.
- [35] “Metal Insulator Transition - an overview | ScienceDirect Topics.” <https://www.sciencedirect.com/topics/chemistry/metal-insulator-transition> (accessed Mar. 27, 2023).
- [36] V. Bisogni *et al.*, “Ground-state oxygen holes and the metal–insulator transition in the negative charge-transfer rare-earth nickelates,” *Nat. Commun.* 2016 71, vol. 7, no. 1, pp. 1–8, Oct. 2016, doi: 10.1038/ncomms13017.
- [37] A. Mercy, J. Bieder, J. Iñiguez, and P. Ghosez, “Structurally triggered metal-insulator transition in rare-earth nickelates,” *Nat. Commun.* 2017 81, vol. 8, no. 1, pp. 1–6, Nov. 2017, doi: 10.1038/s41467-017-01811-x.
- [38] L. Varbaro *et al.*, “Electronic Coupling of Metal-to-Insulator Transitions in Nickelate-Based Heterostructures,” *Adv. Electron. Mater.*, p. 2201291, Mar. 2023, doi: 10.1002/AELM.202201291.
- [39] F. Bernardini, L. Iglesias, M. Bibes, and A. Cano, “Thin-Film Aspects of Superconducting Nickelates,” *Front. Phys.*, vol. 10, no. February, pp. 1–6, 2022, doi: 10.3389/fphy.2022.828007.
- [40] X. Tang, L. Hu, X. X. Zhu, X. X. Zhu, Y. Wang, and Y. Sun, “Orientations-Dependent Metal-to-Insulator Transition in Solution-Deposited High-Entropy Nickelate Thin Films,” *Cryst. Growth Des.*, vol. 22, no. 12, pp. 7317–7324, Dec. 2022, doi: 10.1021/ACS.CGD.2C00945/ASSET/IMAGES/LARGE/CG2C00945\_0006.JPEG.

- [41] J. H. J. Lee *et al.*, “Non-stoichiometry-induced metal-to-insulator transition in nickelate thin films grown by pulsed laser deposition,” *Curr. Appl. Phys.*, vol. 18, no. 12, pp. 1577–1582, Dec. 2018, doi: 10.1016/J.CAP.2018.10.006.
- [42] Y. Zhang *et al.*, “Flexible Metal-Insulator Transitions Based on van der Waals Oxide Heterostructures,” *ACS Appl. Mater. Interfaces*, vol. 11, no. 8, pp. 8284–8290, Feb. 2019, doi: 10.1021/ACSAMI.8B22664.
- [43] Q. Song *et al.*, “Antiferromagnetic metal phase in an electron-doped rare-earth nickelate,” *Nat. Phys.* 2023, pp. 1–7, Jan. 2023, doi: 10.1038/s41567-022-01907-2.
- [44] M. Crespin, P. Levitz, and L. Gataineau, “Reduced forms of LaNiO<sub>3</sub> perovskite. Part 1.— Evidence for new phases: La<sub>2</sub>Ni<sub>2</sub>O<sub>5</sub> and LaNiO<sub>2</sub>,” *J. Chem. Soc. Faraday Trans. 2 Mol. Chem. Phys.*, vol. 79, no. 8, pp. 1181–1194, Jan. 1983, doi: 10.1039/F29837901181.
- [45] M. A. Hayward and M. J. Rosseinsky, “Synthesis of the infinite layer Ni(I) phase NdNiO<sub>2+x</sub> by low temperature reduction of NdNiO<sub>3</sub> with sodium hydride,” *Solid State Sci.*, vol. 5, no. 6, pp. 839–850, Jun. 2003, doi: 10.1016/S1293-2558(03)00111-0.
- [46] M. Kawai, S. Inoue, M. Mizumaki, N. Kawamura, N. Ichikawa, and Y. Shimakawa, “Reversible changes of epitaxial thin films from perovskite LaNiO<sub>3</sub> to infinite-layer structure LaNiO<sub>2</sub>,” *Appl. Phys. Lett.*, vol. 94, no. 8, p. 82102, Feb. 2009, doi: 10.1063/1.3078276.
- [47] D. Kaneko, K. Yamagishi, A. Tsukada, T. Manabe, and M. Naito, “Synthesis of infinite-layer LaNiO<sub>2</sub> films by metal organic decomposition,” *Phys. C Supercond.*, vol. 469, no. 15–20, pp. 936–939, Oct. 2009, doi: 10.1016/J.PHYSC.2009.05.104.
- [48] A. Ikeda, Y. Krockenberger, H. Irie, M. Naito, and H. Yamamoto, “Direct observation of infinite NiO<sub>2</sub> planes in LaNiO<sub>2</sub> films,” *Appl. Phys. Express*, vol. 9, no. 6, p. 61101, Jun. 2016, doi: 10.7567/APEX.9.061101/XML.
- [49] V. V. Poltavets, K. A. Lokshin, S. Dikmen, M. Croft, T. Egami, and M. Greenblatt, “La<sub>3</sub>Ni<sub>2</sub>O<sub>6</sub>: A new double T'-type nickelate with infinite Ni<sup>1+/2+</sup>O<sub>2</sub> layers,” *J. Am. Chem. Soc.*, vol. 128, no. 28, pp. 9050–9051, 2006, doi: 10.1021/ja063031o.
- [50] T. Onozuka, A. Chikamatsu, T. Katayama, T. Fukumura, and T. Hasegawa, “Formation of defect-fluorite structured NdNiO: XHy epitaxial thin films via a soft chemical route from NdNiO<sub>3</sub> precursors,” *Dalt. Trans.*, vol. 45, no. 30, pp. 12114–12118, 2016, doi: 10.1039/c6dt01737a.
- [51] K. Lee *et al.*, “Aspects of the synthesis of thin film superconducting infinite-layer nickelates,” *APL Mater.*, vol. 8, no. 4, Apr. 2020, doi: 10.1063/5.0005103.
- [52] M. Osada, B. Y. Wang, K. Lee, D. Li, and H. Y. Hwang, “Phase diagram of infinite layer praseodymium nickelate Pr<sub>1-x</sub>Sr<sub>x</sub>NiO<sub>2</sub> thin films,” *Phys. Rev. Mater.*, vol. 4, no. 12, pp. 1–5, 2020, doi: 10.1103/PhysRevMaterials.4.121801.
- [53] D. Li *et al.*, “Superconducting Dome in Nd<sub>1-x</sub>Sr<sub>x</sub>NiO<sub>2</sub> Infinite Layer Films,” pp. 1–2.
- [54] X. Ren *et al.*, “Strain-induced enhancement of  $T_c$  in infinite-layer Pr<sub>0.8</sub>Sr<sub>0.2</sub>NiO<sub>2</sub> films,” pp. 1–14, Sep. 2021, doi:

- 10.48550/arxiv.2109.05761.
- [55] M. Osada *et al.*, “Nickelate Superconductivity without Rare-Earth Magnetism: (La,Sr)NiO<sub>2</sub>,” *Adv. Mater.*, vol. 33, no. 45, pp. 1–23, 2021, doi: 10.1002/adma.202104083.
- [56] M. Osada *et al.*, “A Superconducting Praseodymium Nickelate with Infinite Layer Structure,” *Nano Lett.*, vol. 20, no. 8, pp. 5735–5740, 2020, doi: 10.1021/acs.nanolett.0c01392.
- [57] M. Osada, B. Y. Wang, K. Lee, D. Li, and H. Y. Hwang, “Phase diagram of infinite layer praseodymium nickelate Pr<sub>1-x</sub>Sr<sub>x</sub>NiO<sub>2</sub> thin films,” *Phys. Rev. Mater.*, vol. 4, no. 12, pp. 1–5, 2020, doi: 10.1103/PhysRevMaterials.4.121801.
- [58] Y. Xiang *et al.*, “Physical Properties Revealed by Transport Measurements for Superconducting Nd<sub>0.8</sub>Sr<sub>0.2</sub>NiO<sub>2</sub> Thin Films,” *Chinese Phys. Lett.*, vol. 38, no. 4, p. 47401, May 2021, doi: 10.1088/0256-307X/38/4/047401.
- [59] Y. Li *et al.*, “Impact of Cation Stoichiometry on the Crystalline Structure and Superconductivity in Nickelates,” *Front. Phys.*, vol. 9, p. 443, Sep. 2021, doi: 10.3389/FPHY.2021.719534/BIBTEX.
- [60] Q. Gu *et al.*, “Single particle tunneling spectrum of superconducting Nd<sub>1-x</sub>Sr<sub>x</sub>NiO<sub>2</sub> thin films,” *Nat. Commun.*, vol. 11, no. 1, Dec. 2020, doi: 10.1038/s41467-020-19908-1.
- [61] S. W. Zeng *et al.*, “Observation of perfect diamagnetism and interfacial effect on the electronic structures in infinite layer Nd<sub>0.8</sub>Sr<sub>0.2</sub>NiO<sub>2</sub> superconductors,” *Nat. Commun. 2022 131*, vol. 13, no. 1, pp. 1–6, Feb. 2022, doi: 10.1038/s41467-022-28390-w.
- [62] S. Zeng *et al.*, “Superconductivity in infinite-layer nickelate La<sub>1-x</sub>Ca<sub>x</sub>NiO<sub>2</sub> thin films,” *Sci. Adv.*, vol. 8, no. 7, p. 9927, Feb. 2022, doi: 10.1126/SCIADV.ABL9927/SUPPL\_FILE/SCIADV.ABL9927\_SM.PDF.
- [63] S. Zeng *et al.*, “Phase Diagram and Superconducting Dome of Infinite-Layer Nd<sub>1-x</sub>Sr<sub>x</sub>NiO<sub>2</sub> Thin Films,” *Phys. Rev. Lett.*, vol. 125, no. 14, p. 147003, Oct. 2020, doi: 10.1103/PhysRevLett.125.147003.
- [64] N. N. Wang *et al.*, “Pressure-induced monotonic enhancement of T<sub>c</sub> to over 30 K in superconducting Pr<sub>0.82</sub>Sr<sub>0.18</sub>NiO<sub>2</sub> thin films,” *Nat. Commun. 2022 131*, vol. 13, no. 1, pp. 1–8, Jul. 2022, doi: 10.1038/s41467-022-32065-x.
- [65] Q. Gao, Y. Zhao, X. J. Zhou, and Z. Zhu, “Preparation of Superconducting Thin Films of Infinite-Layer Nickelate Nd<sub>0.8</sub>Sr<sub>0.2</sub>NiO<sub>2</sub>,” *Chinese Phys. Lett.*, vol. 38, no. 7, p. 077401, Jul. 2021, doi: 10.1088/0256-307X/38/7/077401.
- [66] X. Zhou *et al.*, “Antiferromagnetism in Ni-Based Superconductors,” *Adv. Mater.*, vol. 34, no. 4, p. 2106117, Jan. 2022, doi: 10.1002/ADMA.202106117.
- [67] X. R. Zhou *et al.*, “Negligible oxygen vacancies, low critical current density, electric-field modulation, in-plane anisotropic and high-field transport of a superconducting Nd<sub>0.8</sub>Sr<sub>0.2</sub>NiO<sub>2</sub>/SrTiO<sub>3</sub> heterostructure,” *Rare Met.*, vol. 40, no. 10, pp. 2847–2854, Oct. 2021, doi: 10.1007/S12598-021-01768-3/METRICS.

- [68] D. Li *et al.*, “Superconductivity in an infinite-layer nickelate,” *Nature*, vol. 572, no. 7771, pp. 624–627, Aug. 2019, doi: 10.1038/s41586-019-1496-5.
- [69] P. Puphal *et al.*, “Topotactic transformation of single crystals: From perovskite to infinite-layer nickelates,” *Sci. Adv.*, vol. 7, no. 49, Dec. 2021, doi: 10.1126/SCIADV.ABL8091.
- [70] G. Krieger *et al.*, “Synthesis and physical properties of perovskite  $\text{Sm}_{1-x}\text{Sr}_x\text{NiO}_3$  ( $x = 0, 0.2$ ) and infinite-layer  $\text{Sm}_{0.8}\text{Sr}_{0.2}\text{NiO}_2$  nickelates,” *J. Phys. Condens. Matter*, vol. 33, no. 26, p. 265701, May 2021, doi: 10.1088/1361-648X/ABFB90.
- [71] Q. Li, C. He, J. Si, X. Zhu, Y. Zhang, and H.-H. Wen, “Absence of superconductivity in bulk  $\text{Nd}_{1-x}\text{Sr}_x\text{NiO}_2$ ,” *Communications Materials*, vol. 1, no. 1. 2020, doi: 10.1038/s43246-020-0018-1.
- [72] B. X. Wang *et al.*, “Synthesis and characterization of bulk  $\text{Nd}_{1-x}\text{Sr}_x\text{NiO}_2$  and  $\text{Nd}_{1-x}\text{Sr}_x\text{NiO}_3$ ,” *Phys. Rev. Mater.*, vol. 4, no. 8, p. 084409, Aug. 2020, doi: 10.1103/PHYSREVMATERIALS.4.084409/FIGURES/8/MEDIUM.
- [73] A. Fujimori and F. Minami, “Valence-band photoemission and optical absorption in nickel compounds,” *Phys. Rev. B*, vol. 30, no. 2, p. 957, Jul. 1984, doi: 10.1103/PhysRevB.30.957.
- [74] C. Xia, J. Wu, Y. Chen, and H. Chen, “Dynamical structural instability and its implications for the physical properties of infinite-layer nickelates,” *Phys. Rev. B*, vol. 105, no. 11, p. 115134, Mar. 2022, doi: 10.1103/PHYSREVB.105.115134/FIGURES/6/MEDIUM.
- [75] F. Bernardini, A. Bosin, and A. Cano, “Geometric effects in the infinite-layer nickelates,” *Phys. Rev. Mater.*, vol. 6, no. 4, p. 044807, Apr. 2022, doi: 10.1103/PHYSREVMATERIALS.6.044807/FIGURES/4/MEDIUM.
- [76] M. A. Hayward, M. A. Green, M. J. Rosseinsky, and J. Sloan, “Sodium Hydride as a Powerful Reducing Agent for Topotactic Oxide Deintercalation: Synthesis and Characterization of the Nickel(I) Oxide  $\text{LaNiO}_2$ ,” *J. Am. Chem. Soc.*, vol. 121, no. 38, pp. 8843–8854, Sep. 1999, doi: 10.1021/ja991573i.
- [77] S. W. Zeng *et al.*, “Observation of perfect diamagnetism and interfacial effect on the electronic structures in infinite layer  $\text{Nd}_{0.8}\text{Sr}_{0.2}\text{NiO}_2$  superconductors,” *Nat. Commun.* 2022 131, vol. 13, no. 1, pp. 1–6, Feb. 2022, doi: 10.1038/s41467-022-28390-w.
- [78] X. Ren *et al.*, “Strain-induced enhancement of  $T_c$  in infinite-layer  $\text{Pr}_{0.8}\text{Sr}_{0.2}\text{NiO}_2$  films,” Sep. 2021, doi: 10.48550/arxiv.2109.05761.
- [79] K. Lee *et al.*, “Character of the ‘normal state’ of the nickelate superconductors,” Mar. 2022, doi: 10.48550/arxiv.2203.02580.
- [80] K. W. Lee and W. E. Pickett, “Infinite-layer  $\text{LaNiO}_2$ :  $\text{Ni}^{1+}$  is not  $\text{Cu}^{2+}$  [33],” *Phys. Rev. B - Condens. Matter Mater. Phys.*, vol. 70, no. 16, pp. 1–7, Oct. 2004, doi: 10.1103/PhysRevB.70.165109.
- [81] Z. Wang, G. M. Zhang, Y. F. Yang, and F. C. Zhang, “Distinct pairing symmetries of superconductivity in infinite-layer nickelates,” *Phys. Rev. B*, vol. 102, no. 22, p. 220501,

- Dec. 2020, doi: 10.1103/PHYSREVB.102.220501/FIGURES/3/MEDIUM.
- [82] M. Kawai, S. Inoue, M. Mizumaki, N. Kawamura, N. Ichikawa, and Y. Shimakawa, “Reversible changes of epitaxial thin films from perovskite  $\text{LaNiO}_3$  to infinite-layer structure  $\text{LaNiO}_2$ ,” *Appl. Phys. Lett.*, vol. 94, no. 8, p. 082102, Feb. 2009, doi: 10.1063/1.3078276.
- [83] M. Crespin, O. Isnard, F. Dubois, J. Choisnet, and P. Odier, “ $\text{LaNiO}_2$ : Synthesis and structural characterization,” *J. Solid State Chem.*, vol. 178, no. 4, pp. 1326–1334, Apr. 2005, doi: 10.1016/J.JSSC.2005.01.023.
- [84] A. Ikeda, Y. Krockenberger, H. Irie, M. Naito, and H. Yamamoto, “Direct observation of infinite  $\text{NiO}_2$  planes in  $\text{LaNiO}_2$  films,” *Appl. Phys. Express*, vol. 9, no. 6, p. 061101, Jun. 2016, doi: 10.7567/APEX.9.061101/XML.
- [85] M. A. Hayward and M. J. Rosseinsky, “Synthesis of the infinite layer Ni(I) phase  $\text{NdNiO}_{2+x}$  by low temperature reduction of  $\text{NdNiO}_3$  with sodium hydride,” *Solid State Sci.*, vol. 5, no. 6, pp. 839–850, Jun. 2003, doi: 10.1016/S1293-2558(03)00111-0.
- [86] G. M. Zhang, Y. F. Yang, and F. C. Zhang, “Self-doped Mott insulator for parent compounds of nickelate superconductors,” *Phys. Rev. B*, vol. 101, no. 2, pp. 1–5, Jan. 2020, doi: 10.1103/PhysRevB.101.020501.
- [87] T. Tanamoto, H. Kohno, and H. Fukuyama, “Magnetic Properties of Extended t-J Model. I. Static Properties,” <http://dx.doi.org/10.1143/JPSJ.62.717>, vol. 62, no. 2, pp. 717–730, Nov. 2013, doi: 10.1143/JPSJ.62.717.
- [88] A. S. Botana, F. Bernardini, and A. Cano, “Nickelate Superconductors: An Ongoing Dialog between Theory and Experiments,” *J. Exp. Theor. Phys.*, vol. 132, no. 4, pp. 618–627, Apr. 2021, doi: 10.1134/S1063776121040026/METRICS.
- [89] C. ; Lu *et al.*, “Magnetic excitations in infinite-layer nickelates,” *Science (80-. )*, vol. 373, no. 6551, pp. 213–216, 2021, doi: 10.1126/science.abd7726.
- [90] Y. F. Yang and G. M. Zhang, “Self-Doping and the Mott-Kondo Scenario for Infinite-Layer Nickelate Superconductors,” *Front. Phys.*, vol. 9, p. 783, Jan. 2022, doi: 10.3389/FPHY.2021.801236/BIBTEX.
- [91] J. Q. Lin *et al.*, “Strong Superexchange in a  $d^9-\delta$  Nickelate Revealed by Resonant Inelastic X-Ray Scattering,” *Phys. Rev. Lett.*, vol. 126, no. 8, p. 087001, Feb. 2021, doi: 10.1103/PHYSREVLETT.126.087001/FIGURES/4/MEDIUM.
- [92] Y. Gu, S. Zhu, X. Wang, J. Hu, and H. Chen, “A substantial hybridization between correlated Ni-d orbital and itinerant electrons in infinite-layer nickelates,” *Commun. Phys.*, vol. 3, no. 1, pp. 1–9, 2020, doi: 10.1038/s42005-020-0347-x.
- [93] G. Krieger *et al.*, “Theory of unconventional superconductivity in nickelate-based materials\*,” *Chinese Phys. B*, vol. 30, no. 10, p. 108204, Nov. 2021, doi: 10.1088/1674-1056/AC0BB1.
- [94] A. S. Botana and M. R. Norman, “Similarities and Differences between  $\text{LaNiO}_2$  and  $\text{CaCuO}_2$  and Implications for Superconductivity,” *Phys. Rev. X*, vol. 10, no. 1, pp. 1–6,

- Mar. 2020, doi: 10.1103/PhysRevX.10.011024.
- [95] Y. Nomura, M. Hirayama, T. Tadano, Y. Yoshimoto, K. Nakamura, and R. Arita, “Formation of a two-dimensional single-component correlated electron system and band engineering in the nickelate superconductor NdNiO<sub>2</sub>,” *Phys. Rev. B*, vol. 100, no. 20, p. 205138, Nov. 2019, doi: 10.1103/PHYSREVB.100.205138/FIGURES/7/MEDIUM.
- [96] X. Wu *et al.*, “Robust dx<sub>2</sub>-y<sub>2</sub>-wave superconductivity of infinite-layer nickelates,” *Phys. Rev. B*, vol. 101, no. 6, pp. 1–5, Feb. 2020, doi: 10.1103/PhysRevB.101.060504.
- [97] F. Deng, P. Jiang, Y. Lu, and Z. Zhong, “First-principle study of Sr-doping effect in Nd<sub>1-x</sub>Sr<sub>x</sub>NiO<sub>2</sub>,” *Europhys. Lett.*, vol. 135, no. 6, p. 67001, Nov. 2021, doi: 10.1209/0295-5075/AC2073.
- [98] M. C. Jung, H. LaBollita, V. Pardo, and A. S. Botana, “Antiferromagnetic insulating state in layered nickelates at half filling,” *Sci. Reports 2022 121*, vol. 12, no. 1, pp. 1–9, Oct. 2022, doi: 10.1038/s41598-022-22176-2.
- [99] G. A. Pan *et al.*, “Superconductivity in a quintuple-layer square-planar nickelate,” *Nat. Mater.*, vol. 21, no. 2, pp. 160–164, 2022, doi: 10.1038/s41563-021-01142-9.
- [100] M. Jiang, M. Berciu, and G. A. Sawatzky, “Critical Nature of the Ni Spin State in Doped NdNiO<sub>2</sub>,” *Phys. Rev. Lett.*, vol. 124, no. 20, p. 207004, May 2020, doi: 10.1103/PHYSREVLETT.124.207004/FIGURES/4/MEDIUM.
- [101] J. Karp *et al.*, “Comparative many-body study of Pr<sub>4</sub>Ni<sub>3</sub>O<sub>8</sub> and NdNiO<sub>2</sub>,” *Phys. Rev. B*, vol. 102, no. 24, p. 245130, Dec. 2020, doi: 10.1103/PHYSREVB.102.245130/FIGURES/10/MEDIUM.
- [102] M. Hepting *et al.*, “Complex magnetic order in nickelate slabs,” *Nat. Phys. 2018 1411*, vol. 14, no. 11, pp. 1097–1102, Jul. 2018, doi: 10.1038/s41567-018-0218-5.
- [103] B. H. Goodge *et al.*, “Doping evolution of the Mott-Hubbard landscape in infinite-layer nickelates,” *Proc. Natl. Acad. Sci. U. S. A.*, vol. 118, no. 2, p. e2007683118, Jan. 2021.
- [104] Y. Shen *et al.*, “Electronic Character of Charge Order in Square-Planar Low-Valence Nickelates,” 2023, doi: 10.1103/PhysRevX.13.011021.
- [105] Y. Cui *et al.*, “NMR Evidence of Antiferromagnetic Spin Fluctuations in Nd<sub>0.85</sub>Sr<sub>0.15</sub>NiO<sub>2</sub>,” *Chinese Phys. Lett.*, vol. 38, no. 6, p. 067401, Jun. 2021, doi: 10.1088/0256-307X/38/6/067401.
- [106] J. Fowlie *et al.*, “Intrinsic magnetism in superconducting infinite-layer nickelates,” *Nat. Phys. 2022 189*, vol. 18, no. 9, pp. 1043–1047, Aug. 2022, doi: 10.1038/s41567-022-01684-y.
- [107] Á. A. Carrasco Álvarez, S. Petit, L. Iglesias, W. Prellier, M. Bibes, and J. Varignon, “Structural instabilities of infinite-layer nickelates from first-principles simulations,” *Phys. Rev. Res.*, vol. 4, no. 2, p. 023064, Jun. 2022, doi: 10.1103/PHYSREVRESEARCH.4.023064/FIGURES/3/MEDIUM.
- [108] L. Si *et al.*, “Topotactic Hydrogen in Nickelate Superconductors and Akin Infinite-Layer

- Oxides AB O<sub>2</sub>,” *Phys. Rev. Lett.*, vol. 124, no. 16, pp. 1–8, Apr. 2020, doi: 10.1103/PhysRevLett.124.166402.
- [109] T. Onozuka, A. Chikamatsu, T. Katayama, T. Fukumura, and T. Hasegawa, “Dalton Transactions PAPER Formation of defect-fluorite structured NdNiO<sub>x</sub>H<sub>y</sub> epitaxial thin films via a soft chemical route from NdNiO<sub>3</sub> precursors,” *Dalt. Trans.*, vol. 45, 2016, doi: 10.1039/c6dt01737a.
- [110] D. Kutsuzawa *et al.*, “Strain-enhanced topotactic hydrogen substitution for oxygen in SrTiO<sub>3</sub> epitaxial thin film,” *Appl. Phys. Lett.*, vol. 113, no. 25, p. 253104, Dec. 2018, doi: 10.1063/1.5057370.
- [111] X. Ding *et al.*, “Critical role of hydrogen for superconductivity in nickelates,” *Nature*, vol. 615, no. 7950, pp. 50–55, Mar. 2023, doi: 10.1038/S41586-022-05657-2.
- [112] Y. Ji, J. Liu, L. Li, and Z. Liao, “Superconductivity in infinite layer nickelates,” *J. Appl. Phys.*, vol. 130, no. 6, p. 060901, Aug. 2021, doi: 10.1063/5.0056328.
- [113] J. F. Mitchell, “A Nickelate Renaissance,” *Front. Phys.*, vol. 9, p. 753, Dec. 2021, doi: 10.3389/FPHY.2021.813483/BIBTEX.
- [114] F. Bernardini, L. Iglesias, M. Bibes, and A. Cano, “Thin-Film Aspects of Superconducting Nickelates,” *Front. Phys.*, vol. 10, no. February, pp. 1–6, 2022, doi: 10.3389/fphy.2022.828007.
- [115] H. Chen, A. Hampel, J. Karp, F. Lechermann, and A. J. Millis, “Dynamical Mean Field Studies of Infinite Layer Nickelates: Physics Results and Methodological Implications,” *Front. Phys.*, vol. 10, p. 16, Feb. 2022, doi: 10.3389/FPHY.2022.835942.
- [116] B. H. Goodge *et al.*, “Resolving the polar interface of infinite-layer nickelate thin films,” *Nat. Mater.* 2023, pp. 1–8, Mar. 2023, doi: 10.1038/s41563-023-01510-7.
- [117] G. Krieger *et al.*, “Synthesis of infinite-layer nickelates and influence of the capping-layer on magnetotransport,” *J. Phys. D. Appl. Phys.*, vol. 56, no. 2, p. 024003, Dec. 2022, doi: 10.1088/1361-6463/ACA54A.
- [118] Q. Gao, Y. Zhao, X. Zhou, and Z. Zhu, “Preparation of superconducting thin films of infinite-layer nickelate Nd<sub>0.8</sub>Sr<sub>0.2</sub>NiO<sub>2</sub>,” pp. 1–13, Feb. 2021, [Online]. Available: <http://arxiv.org/abs/2102.10292>.
- [119] X. Ding *et al.*, “Stability of superconducting Nd<sub>0.8</sub>Sr<sub>0.2</sub>NiO<sub>2</sub> thin films,” *Sci. China Physics, Mech. Astron.*, vol. 65, no. 6, pp. 1–8, Jun. 2022, doi: 10.1007/S11433-021-1871-X/METRICS.
- [120] A. Sharma, B. Devanarayanan, P. D. Patel, and N. Singh, “Why is Superconductivity absent in bulk Infinite-layer Nickelates?,” Jun. 2022, Accessed: Mar. 30, 2023. [Online]. Available: <https://arxiv.org/abs/2206.07539v1>.
- [121] M. Kitatani, L. Si, O. Janson, R. Arita, Z. Zhong, and K. Held, “Nickelate superconductors—a renaissance of the one-band Hubbard model,” *npj Quantum Mater.*, vol. 5, no. 1, pp. 6–11, Dec. 2020, doi: 10.1038/s41535-020-00260-y.

- [122] S. Upasen, P. Batocchi, F. Mauvy, A. Slodczyk, and P. Colomban, "Protonation and structural/chemical stability of  $\text{Ln}_2\text{NiO}_{4+\delta}$  ceramics vs.  $\text{H}_2\text{O}/\text{CO}_2$ : High temperature/water pressure ageing tests," *J. Alloys Compd.*, vol. 622, pp. 1074–1085, Feb. 2015, doi: 10.1016/J.JALLCOM.2014.11.017.
- [123] A. P. Tarutin, J. G. Lyagaeva, D. A. Medvedev, L. Bi, and A. A. Yaremchenko, "Recent advances in layered  $\text{Ln}_2\text{NiO}_{4+\delta}$  nickelates: fundamentals and prospects of their applications in protonic ceramic fuel and electrolysis cells," *J. Mater. Chem. A*, vol. 9, no. 1, pp. 154–195, Jan. 2021, doi: 10.1039/D0TA08132A.
- [124] A. L. Soldati, L. Baqué, F. Napolitano, and A. Serquis, "Cobalt–iron red–ox behavior in nanostructured  $\text{La}_{0.4}\text{Sr}_{0.6}\text{Co}_{0.8}\text{Fe}_{0.2}\text{O}_{3-\delta}$  cathodes," *J. Solid State Chem.*, vol. 198, pp. 253–261, Feb. 2013, doi: 10.1016/J.JSSC.2012.10.019.
- [125] T. Nakamura, K. Yashiro, K. Sato, and J. Mizusaki, "Thermally-induced and chemically-induced structural changes in layered perovskite-type oxides  $\text{Nd}_{2-x}\text{Sr}_x\text{NiO}_{4+\delta}$  ( $x = 0, 0.2, 0.4$ )," *Solid State Ionics*, vol. 181, no. 8–10, pp. 402–411, Mar. 2010, doi: 10.1016/J.SSI.2010.02.002.
- [126] T. Nakamura, K. Yashiro, K. Sato, and J. Mizusaki, "Oxygen nonstoichiometry and defect equilibrium in  $\text{La}_{2-x}\text{Sr}_x\text{NiO}_{4+\delta}$ ," *Solid State Ionics*, vol. 180, no. 4–5, pp. 368–376, Apr. 2009, doi: 10.1016/J.SSI.2009.01.013.
- [127] E. Boehm, J. M. Bassat, P. Dordor, F. Mauvy, J. C. Grenier, and P. Stevens, "Oxygen diffusion and transport properties in non-stoichiometric  $\text{Ln}_{2-x}\text{NiO}_{4+\delta}$  oxides," *Solid State Ionics*, vol. 176, no. 37–38, pp. 2717–2725, Nov. 2005, doi: 10.1016/J.SSI.2005.06.033.
- [128] M. Zaghrioui, F. Giovannelli, N. P. D. Brouri, and I. Laffez, "Anomalies in magnetic susceptibility of nonstoichiometric  $\text{Nd}_2\text{NiO}_{4+\delta}$  ( $\delta=0.049, 0.065, 0.077, 0.234$ )," *J. Solid State Chem.*, vol. 177, no. 10, pp. 3351–3358, Oct. 2004, doi: 10.1016/J.JSSC.2004.05.065.
- [129] C. Allançon, A. Gonthier-Vassal, J. M. Bascat, J. P. Loup, and P. Odier, "Influence of oxygen on structural transitions in  $\text{Pr}_2\text{NiO}_{4+\delta}$ ," *Solid State Ionics*, vol. 74, no. 3–4, pp. 239–248, Dec. 1994, doi: 10.1016/0167-2738(94)90216-X.
- [130] M. Filippi, B. Kundys, S. Agrestini, W. Prellier, H. Oyanagi, and N. L. Saini, "Charge order, dielectric response, and local structure of  $\text{La}_{5/3}\text{Sr}_{1/3}\text{NiO}_4$  system," *J. Appl. Phys.*, vol. 106, no. 10, 2009, doi: 10.1063/1.3260222.
- [131] E. Kravchenko *et al.*, "High-temperature characterization of oxygen-deficient  $\text{K}_2\text{NiF}_4$ -type  $\text{Nd}_{2-x}\text{Sr}_x\text{NiO}_{4-\delta}$  ( $x = 1.0-1.6$ ) for potential SOFC/SOEC applications," *J. Mater. Chem. A*, vol. 3, no. 47, pp. 23852–23863, 2015, doi: 10.1039/c5ta06779k.
- [132] T. Nakamura, K. Yashiro, K. Sato, and J. Mizusaki, "Oxygen nonstoichiometry and defect equilibrium in  $\text{La}_2 - x\text{Sr}_x\text{NiO}_4 + \delta$ ," *Solid State Ionics*, vol. 180, no. 4–5, pp. 368–376, 2009, doi: 10.1016/j.ssi.2009.01.013.
- [133] A. Grimaud, F. Mauvy, J. Marc Bassat, S. Fourcade, M. Marrony, and J. Claude Grenier, "Hydration and transport properties of the  $\text{Pr}_{2-x}\text{Sr}_x\text{NiO}_{4+\delta}$  compounds as  $\text{H}^+$ -SOFC

- cathodes,” *J. Mater. Chem.*, vol. 22, no. 31, pp. 16017–16025, 2012, doi: 10.1039/c2jm31812a.
- [134] A. Aguadero, M. J. Escudero, M. Pérez, J. A. Alonso, V. Pomjakushin, and L. Daza, “Effect of Sr content on the crystal structure and electrical properties of the system  $\text{La}_{2-x}\text{Sr}_x\text{NiO}_{4+\delta}$  ( $0 \leq x \leq 1$ ),” *Dalt. Trans.*, no. 36, pp. 4377–4383, 2006, doi: 10.1039/b606316k.
- [135] J. Alonso, M. Vallet-Regí, and J. M. González-Calbet, “Phase transitions and oxygen content in the  $\text{Nd}_{2-x}\text{Sr}_x\text{NiO}_{4+\delta}$  system,” *Solid State Ionics*, vol. 66, no. 3–4, pp. 219–223, 1993, doi: 10.1016/0167-2738(93)90410-5.
- [136] M. Jiménez-Ruiz, C. Prieto, J. L. Martínez, and J. M. Alonso, “Nickel Oxidation State and Magnetic Properties of Hole-Doped and Reduced  $\text{Nd}_{2-x}\text{Sr}_x\text{NiO}_y$  Compounds,” *J. Solid State Chem.*, vol. 140, no. 2, pp. 278–284, 1998, doi: 10.1006/jssc.1998.7887.
- [137] S. M. Doyle, M. P. Sridhar Kumar, and D. McK Paul, “Magnetism and resistivity of  $\text{Nd}_{2-x}\text{Sr}_x\text{NiO}_{4+\delta}$  compounds,” *J. Phys. Condens. Matter*, vol. 4, no. 13, pp. 3559–3568, 1992, doi: 10.1088/0953-8984/4/13/018.
- [138] R. D. Shannon and IUCr, “Revised effective ionic radii and systematic studies of interatomic distances in halides and chalcogenides,” *urn:issn:0567-7394*, vol. 32, no. 5, pp. 751–767, Sep. 1976, doi: 10.1107/S0567739476001551.
- [139] C. Brisi and P. Rolando, “No Title,” *Ann. Chim.*, vol. 59, no. 385, 1969.
- [140] Y. Takeda, M. Nishijima, N. Imanishi, R. Kanno, O. Yamamoto, and M. Takano, “Crystal chemistry and transport properties of  $\text{Nd}_{2-x}\text{AxNiO}_4$  (A=Ca, Sr, or Ba,  $0 \leq x \leq 1.4$ ),” *J. Solid State Chem.*, vol. 96, no. 1, pp. 72–83, Jan. 1992, doi: 10.1016/S0022-4596(05)80299-3.
- [141] “Shannon Radii.” <http://abulafia.mt.ic.ac.uk/shannon/ptable.php> (accessed Sep. 14, 2023).
- [142] R. D. Shannon, “Revised effective ionic radii and systematic studies of interatomic distances in halides and chalcogenides,” *Acta Crystallogr. Sect. A*, vol. 32, no. 5, pp. 751–767, Sep. 1976, doi: 10.1107/S0567739476001551/FULL.
- [143] N. Gayathri, A. K. Raychaudhuri, X. Q. Xu, J. L. Peng, and R. L. Greene, “Electronic conduction in : the dependence on the oxygen stoichiometry,” *J. Phys. Condens. Matter*, vol. 10, no. 6, p. 1323, Feb. 1998, doi: 10.1088/0953-8984/10/6/015.
- [144] G. W. Winkler, M. Ganahl, D. Schuricht, al -, J. Blasco, and I. Garcia, “A comparative study of the crystallographic, magnetic and electrical properties of the  $\text{Nd}_{1-x}\text{La}_x\text{NiO}_{3-\delta}$  system,” *J. Phys. Condens. Matter*, vol. 6, no. 49, p. 10759, Dec. 1994, doi: 10.1088/0953-8984/6/49/017.
- [145] X. Q. Xu, J. L. Peng, Z. Y. Li, H. L. Ju, and R. L. Greene, “Resistivity, thermopower, and susceptibility of  $\text{RNiO}_3$  (R=La,Pr)” *Phys. Rev. B*, vol. 48, no. 2, p. 1112, Jul. 1993, doi: 10.1103/PhysRevB.48.1112.
- [146] J. Liu *et al.*, “Heterointerface engineered electronic and magnetic phases of  $\text{NdNiO}_3$  thin films,” *Nat. Commun. 2013 41*, vol. 4, no. 1, pp. 1–11, Nov. 2013, doi: 10.1038/ncomms3714.

- [147] E. Mikheev *et al.*, “Tuning bad metal and non-Fermi liquid behavior in a Mott material: Rare-earth nickelate thin films,” *Sci. Adv.*, vol. 1, no. 10, Nov. 2015, doi: 10.1126/SCIADV.1500797/SUPPL\_FILE/1500797\_SM.PDF.
- [148] V. Hien-Hoang, N. K. Chung, and H. J. Kim, “Electrical transport properties and Kondo effect in  $\text{La}_{1-x}\text{Pr}_x\text{NiO}_{3-\delta}$  thin films,” *Sci. Reports 2021 111*, vol. 11, no. 1, pp. 1–10, Mar. 2021, doi: 10.1038/s41598-021-84736-2.
- [149] J. Kondo, “Resistance Minimum in Dilute Magnetic Alloys,” *Prog. Theor. Phys.*, vol. 32, no. 1, 1964, Accessed: Apr. 20, 2023. [Online]. Available: <https://academic.oup.com/ptp/article/32/1/37/1834632>.
- [150] R. P. Khosla and J. R. Fischer, “Magnetoresistance in Degenerate CdS: Localized Magnetic Moments,” *Phys. Rev. B*, vol. 2, no. 10, p. 4084, Nov. 1970, doi: 10.1103/PhysRevB.2.4084.
- [151] D. R. Hamann, “New Solution for Exchange Scattering in Dilute Alloys,” *Phys. Rev.*, vol. 158, no. 3, p. 570, Jun. 1967, doi: 10.1103/PhysRev.158.570.
- [152] M. Yarmohammadi and H. Cheraghchi, “Effective low-energy RKKY interaction in doped topological crystalline insulators,” *Phys. Rev. B*, vol. 102, no. 7, p. 075411, Aug. 2020, doi: 10.1103/PHYSREVB.102.075411/FIGURES/12/MEDIUM.
- [153] S. Barua, M. C. Hatnean, M. R. Lees, and G. Balakrishnan, “Signatures of the Kondo effect in  $\text{VSe}_2$ ,” *Sci. Reports 2017 71*, vol. 7, no. 1, pp. 1–10, Sep. 2017, doi: 10.1038/s41598-017-11247-4.
- [154] F. J. Ohkawa, “Magnetoresistance of Kondo lattices,” *Phys. Rev. Lett.*, vol. 64, no. 19, p. 2300, May 1990, doi: 10.1103/PhysRevLett.64.2300.
- [155] A. N. Pasupathy *et al.*, “The Kondo Effect in the Presence of Ferromagnetism,” *Science (80-. )*, vol. 306, no. 5693, pp. 86–89, Oct. 2004, doi: 10.1126/SCIENCE.1102068.
- [156] S. Mugiraneza and A. M. Hallas, “Tutorial: a beginner’s guide to interpreting magnetic susceptibility data with the Curie-Weiss law,” *Commun. Phys. 2022 51*, vol. 5, no. 1, pp. 1–12, Apr. 2022, doi: 10.1038/s42005-022-00853-y.
- [157] S. Mugiraneza and A. M. Hallas, “Tutorial: a beginner’s guide to interpreting magnetic susceptibility data with the Curie-Weiss law,” *Commun. Phys. 2022 51*, vol. 5, no. 1, pp. 1–12, Apr. 2022, doi: 10.1038/s42005-022-00853-y.
- [158] K. Lee *et al.*, “Aspects of the synthesis of thin film superconducting infinite-layer nickelates,” *APL Mater.*, vol. 8, no. 4, Apr. 2020, doi: 10.1063/5.0005103.
- [159] D. Li *et al.*, “Superconducting Dome in  $\text{Nd}_{1-x}\text{Sr}_x\text{NiO}_2$  Infinite Layer Films,” *Phys. Rev. Lett.*, vol. 125, no. 2, p. 27001, Jul. 2020, doi: 10.1103/PhysRevLett.125.027001.
- [160] A. Kalabukhov, R. Gunnarsson, J. Börjesson, E. Olsson, T. Claeson, and D. Winkler, “Effect of oxygen vacancies in the  $\text{SrTiO}_3$  substrate on the electrical properties of the  $\text{LaAlO}_3/\text{SrTiO}_3$  interface,” *Phys. Rev. B - Condens. Matter Mater. Phys.*, vol. 75, no. 12, Mar. 2007, doi: 10.1103/PHYSREVB.75.121404.

- [161] J. G. Connell, B. J. Isaac, G. B. Ekanayake, D. R. Strachan, and S. S. A. Seo, "Preparation of atomically flat SrTiO<sub>3</sub> surfaces using a deionized-water leaching and thermal annealing procedure," *Appl. Phys. Lett.*, vol. 101, no. 25, p. 251607, Dec. 2012, doi: 10.1063/1.4773052/26465.
- [162] S. Woo *et al.*, "Surface properties of atomically flat poly-crystalline SrTiO<sub>3</sub>," *Sci. Rep.*, vol. 5, Mar. 2015, doi: 10.1038/SREP08822.
- [163] M. Tripathi *et al.*, "Cleaning graphene: comparing heat treatments in air and in vacuum."
- [164] A. J. Hauser, E. Mikheev, N. E. Moreno, J. Hwang, J. Y. Zhang, and S. Stemmer, "Correlation between stoichiometry, strain, and metal-insulator transitions of NdNiO<sub>3</sub> films," *Appl. Phys. Lett.*, vol. 106, no. 9, p. 92104, Mar. 2015, doi: 10.1063/1.4914002/14467160/092104\_1\_ACCEPTED\_MANUSCRIPT.PDF.
- [165] E. Breckenfeld, Z. Chen, A. R. Damodaran, and L. W. Martin, "Effects of nonequilibrium growth, nonstoichiometry, and film orientation on the metal-to-insulator transition in NdNiO<sub>3</sub> thin films," *ACS Appl. Mater. Interfaces*, vol. 6, no. 24, pp. 22436–22444, Dec. 2014, doi: 10.1021/AM506436S/SUPPL\_FILE/AM506436S\_SI\_001.PDF.
- [166] G. Catalan, R. M. Bowman, and J. M. Gregg, "Transport properties of NdNiO<sub>3</sub> thin films made by pulsed-laser deposition," *J. Appl. Phys.*, vol. 87, no. 1, pp. 606–608, Jan. 2000, doi: 10.1063/1.371912.
- [167] Q. Gao *et al.*, "Superconductivity in infinite-layer Pr<sub>0.8</sub>Sr<sub>0.2</sub>NiO<sub>2</sub> films on different substrates," *APS*, vol. 2022, p. T57.014, 2022, Accessed: Aug. 28, 2023. [Online]. Available: <https://ui.adsabs.harvard.edu/abs/2022APS..MART57014G/abstract>.
- [168] X. Zhou *et al.*, "Experimental progress on the emergent infinite-layer Ni-based superconductors," *Mater. Today*, vol. 55, pp. 170–185, May 2022, doi: 10.1016/J.MATTOD.2022.02.016.
- [169] A. Venimadhav, I. C. Lekshmi, and M. S. Hegde, "Strain-induced metallic behavior in PrNiO<sub>3</sub> epitaxial thin films," *Mater. Res. Bull.*, vol. 37, no. 2, pp. 201–208, 2002.
- [170] K. Lee *et al.*, "Linear-in-temperature resistivity for optimally superconducting (Nd,Sr)NiO<sub>2</sub>," *Nat. 2023 6197969*, vol. 619, no. 7969, pp. 288–292, Jul. 2023, doi: 10.1038/s41586-023-06129-x.
- [171] J. W. Cooley, P. A. W. Lewis, and P. D. Welch, "The Fast Fourier Transform and its Applications," *IEEE Trans. Educ.*, vol. 12, no. 1, pp. 27–34, 1969, doi: 10.1109/TE.1969.4320436.
- [172] F. M. Smits, "Measurement of Sheet Resistivities with the Four-Point Probe," *Bell Syst. Tech. J.*, vol. 37, no. 3, pp. 711–718, 1958, doi: 10.1002/J.1538-7305.1958.TB03883.X.